Thiago Destri Cabral

A FIRST APPROACH TO STRUCTURAL HEALTH MONITORING OF ADHESIVE BONDED JOINTS IN PIPELINES USING INTEGRATED FIBER OPTIC SENSORS

Dissertation submitted to the Mechanical Engineering Graduate Program of the Federal University of Santa Catarina in partial fulfillment of the requirements for the degree of Master of Mechanical Engineering.

Supervisor: Prof. Armando Albertazzi Gonçalves Jr., Dr. Eng.

Co-supervisor: Prof. Daniel Pedro Willemann, Dr. Eng.

Florianópolis
2016

Ficha de identificação da obra elaborada pelo autor,
através do Programa de Geração Automática da Biblioteca Universitária
da UFSC.

Destri Cabral, Thiago
A First Approach to Structural Health Monitoring of Adhesive Bonded Joints in Pipelines Using Integrated Fiber Optic Sensors / Thiago Destri Cabral ; orientador, Armando Albertazzi Gonçalves Jr ; coorientador, Daniel Pedro Willemann. – Florianópolis, SC, 2016.

151 p.

Dissertação (mestrado) – Universidade Federal de Santa Catarina, Centro Tecnológico. Programa de Pós-Graduação em Engenharia Mecânica.

Inclui Referências

1. Engenharia Mecânica. 2. Materiais Compósitos. 3. Uniões Adesivadas. 4. Sensores de Fibra Óptica. 5. Integridade Estrutural. I. Albertazzi Gonçalves Jr, Armando. II. Pedro Willemann, Daniel. III. Universidade Federal de Santa Catarina. Programa de Pós-Graduação em Engenharia Mecânica. IV. Título.

Thiago Destri Cabral

A FIRST APPROACH TO STRUCTURAL HEALTH MONITORING OF ADHESIVE BONDED JOINTS IN PIPELINES USING INTEGRATED FIBER OPTIC SENSORS

This Dissertation was considered adequate to obtain the degree of Master of Mechanical Engineering and was approved on its final version by the Mechanical Engineering Graduate Program.

Florianópolis, 3rd of November of 2016.

_____

Prof. Jonny Carlos da Silva, Dr. Eng.
Program Coordinator

Examining board:

_____

Prof. Armando Albertazzi Gonçalves Jr., Dr. Eng. - Supervisor
Federal University of Santa Catarina

_____

Prof. Marco Antonio Martins Cavaco, Dr. Eng.
Federal University of Santa Catarina

_____

Antonio Carlos Zimmermann, Dr. Eng.
Federal University of Santa Catarina

_____

Sergio Damasceno Soares, Dr. Eng.
Cenpes - Petrobras

This thesis is dedicated to the memory
of my late grandfather, José Destri.

ACKNOWLEDGMENTS

I would like to thank, in no particular order:

- Petrobras, for the interest and financial resources invested into composite pipelines inspection technology, making this project possible;
- Federal University of Santa Catarina, for the amazing mechanical engineering undergrad and postgrad programs;
- The Laboratory of Metrology and Automation (LABMETRO), for providing the necessary infrastructure to conduct this experimental research project;
- The great colleagues Filipe Zanini Broetto, Marcos José Ferreira Carvalho, Mariana Tiemi Tamura, Estiven Sánchez Barrera, with whom I shared not only classrooms and the workplace, but also many amazing moments;
- The best of friends Bruno Travassos, João Paulo 'Tiz', Lucas de Camargo, Miguel Mendes and Victor Ugo Amarante, for all the shared laughs, rages, rants, heavy metal concerts and beers;
- The great friends Alexandre Bittencourt de Sá, Conrado da Veiga Balvedi, Jian Carlos Bonelli and Juan Filipi Garcês for the comradery and all the interesting and productive discussions;
- The interns Eduardo César, Eduardo Fronza, James Nogueira, Jonathan Luiz, and Leandro Neves for all their help with preparing and executing experiments;
- All my other colleagues at LABMETRO, who are too many to list here but made the lab a very warm and welcoming place;
- Prof. Armando Albertazzi, for his impeccable dedication as a professor, researcher and supervisor;
- Prof. Daniel Pedro Willemann, co-supervisor and great friend, for the friendship and brilliant guidance since I joined LABMETRO back in 2009;
- Former professor, friend, beer sommelier and English gentleman at heart Nilton Branco, for the captivating teaching and inspiration;
- My family, for all the support.

“And it came to pass that AC learned how to reverse the direction of entropy. But there was now no man to whom AC might give the answer of the last question. No matter. The answer – by demonstration – would take care of that, too. For another timeless interval, AC thought how best to do this. Carefully, AC organized the program. The consciousness of AC encompassed all of what had once been a Universe and brooded over what was now Chaos. Step by step, it must be done. And AC said, ‘LET THERE BE LIGHT!’ And there was light-”

The Last Question – Isaac Asimov

ABSTRACT

The sea, sea salt aerosol, direct exposure to sunlight and corrosive fluids make oil and gas rigs hostile environments for its own infrastructure. Metallic pipelines and structural items are being progressively replaced by engineering plastics and composite materials with high structural efficiency and corrosion resistance. As these components require regular inspection and maintenance routines, developing non-destructive inspection techniques is required. The high cost associated with conducting maintenance in hazardous and difficult to access areas, along with the prevalence of premature failure of adhesive bonded joints between composite material pipes, creates a demand for passive long-term monitoring techniques able to act as a bridge between scheduled inspections. This work explores the use of fiber optic sensors integrated into the bonded joints as a potential long-term solution. Several optical fiber sensors were studied and one was selected for testing purposes. Sensors were then integrated internally and externally to bonded joints between pipes with similar geometry to those used in oil and gas rigs. A series of non-destructive tests plus a destructive test were realized. Shearography and computed tomography, as supporting techniques, corroborate the capacity of the selected sensors and devised sensing strategy to detect the presence of voids and debondings at various stages of the pipeline's life cycle.

Keywords: Composite materials, adhesive bonded joints, fiber optic sensors, non-destructive testing, structural health monitoring.

RESUMO

O mar, a atmosfera salina, a incidência solar e a presença de fluidos corrosivos fazem de plataformas de prospecção de petróleo e gás ambientes hostis para a infraestrutura nelas instalada. Tubulações e itens estruturais metálicos vêm sendo substituídos por plásticos de engenharia e materiais compostos com alta eficiência estrutural e resistência à corrosão.

Um material compósito é formado pela combinação, em escala macroscópica, de dois ou mais componentes com distintas características físicas e química, que quando combinados produzem um material cujas propriedades diferem das de seus constituintes.

Visto que estes componentes também necessitam de inspeção e manutenção regular, tem-se a necessidade de desenvolvimento de múltiplas técnicas não-destrutivas de avaliação. O que levou à adaptação de técnicas como a termografia, holografia, shearografia, ultrassonografia e tomografia para a inspeção de compósitos.

Ainda, o alto custo associado à realização de ensaios em áreas classificadas e de difícil acesso, conjuntamente com a prevalência de falhas prematuras em uniões adesivadas em tubulações de material composto, criam uma demanda por técnicas passivas de monitoramento a longo prazo capazes de atuar como uma ponte entre as inspeções periódicas.

A união por adesivo é um processo testado, confiável e consolidado para unir substratos metálicos, plásticos, cerâmicos e compósitos. Apresenta como vantagens com relação às uniões parafusadas ou rebitadas massa reduzida, melhor distribuição de esforços mecânicos e melhor resistência à fadiga devido à maior flexibilidade e capacidade de inibição da propagação de trincas dos adesivos. Apesar disso são de difícil modelagem matemática, difícil manutenção e são consideradas como uniões permanentes. Este é o processo mais utilizado para unir tubulações de plástico e de compósito, tanto em aplicações na construção civil como na indústria.

O presente trabalho explora a utilização de sensores de fibra óptica integrados às uniões adesivadas como potencial solução deste problema.

Foram estudados diversos sensores de fibra óptica, como redes de Bragg, interferômetros de Fabry-Pérot e sensores distribuídos com base em deflectometria. Alguns sensores capazes de medir múltiplos parâmetros também são apresentados.

Para a realização de ensaios, sensores de fibra óptica foram integrados interna e externamente a uniões adesivadas de tubulações de características similares às utilizadas em campo. Um total de doze fibras sensoras, contendo 3 redes de Bragg cada foram colocadas internamente à camada de adesivo das uniões para medir o campo de deformação axial no interior da união. Além disso, fibras mais longas contendo 12 redes de Bragg foram projetadas para serem enroladas externamente ao longo da circunferência das uniões.

Uma série de ensaios não-destrutivos foram realizados, começando-se por testes de inserção dos sensores. Três uniões adesivadas foram instrumentadas, incluindo uma com defeitos planejados para fins de comparação.

Por fim um dos corpos de prova foi ensaiado de maneira não-destrutiva para avaliar se a instrumentação integrada possui impacto negativo nas propriedades mecânicas das uniões. O corpo de prova ensaiado falhou em uma região distante da instrumentada, mas mais testes precisam ser realizados para que se estabeleça significância estatística de que a instrumentação não foi deletéria.

Shearografia digital e tomografia computadorizada foram utilizadas como técnicas de apoio e corroboraram a capacidade dos sensores selecionados e da estratégia de medição adotada para a detecção da presença de vazios e falhas de adesão em várias etapas do ciclo de vida das uniões.

Palavras-chave: Materiais compósitos, uniões adesivadas, sensores de fibra óptica, ensaios não-destrutivos, monitoramento de integridade estrutural.

LIST OF FIGURES

LIST OF TABLES

LIST OF ABBREVIATIONS

FRP	Fiber Reinforced Plastics
NDT	Non Destructive Tests
CPVC	Chlorinated Polyvinyl Chloride
CCM	Carbon Ceramic Material
CCB	Carbon Ceramic Brakes
CT	Computed Tomography
SHM	Structural Health Monitoring
SiO_2	Silicon Dioxide
OH^-	Hydroxyl Radical
Fe^{2+}, Fe^{3+}	Iron Ions
Cu^{2+}	Copper Ion
Cr^{2+}	Chromium Ion
V^{4+}	Vanadium Ion
FBG	Fiber Bragg Grating
EDFA	Erbium-Doped Fiber Amplifier
FFPI	Fiber Fabry-Pérot Interferometer
OTDR	Optical Time Domain Reflectometry
OFDR	Optical Frequency Domain Reflectometry

LIST OF SYMBOLS

Symbol	Unit	Description
a	μm	Radius of optical fiber core
n	-	Index of refraction
ϕ	rad	Incidence angle
θ_0	rad	Optical fiber acceptance angle
$\theta_{0,max}$	rad	Maximum acceptance angle
Δ	-	Core-cladding index difference
NA	-	Numerical aperture
M	-	Modal volume
V	-	Normalized frequency
λ	nm	Wavelength
α_{scatt}	$Np \cdot km^{-1}$	Rayleigh scattering loss
p	-	Photoelastic coefficient
k_b	$J \cdot K^{-1}$	Boltzmann's constant
T_f	K	Fictive Temperature
β_T	$m^2 \cdot N^{-1}$	Isothermal compressibility
x	mm	Distance
Δt	s	Maximum pulse broadening
t_{max}	s	Fastest mode travel time
t_{min}	s	Slowest mode travel time
L	mm	Length
λ_B	nm	Bragg wavelength
Δn	-	Index of refraction variation
n_{ef}	-	Effective index of refraction
Λ	nm	Bragg grating period
$\delta a/\delta b$	-	Partial derivative of *a* in relation to *b*
T	$K, -$	Temperature, t-test statistic
ΔT	K	Temperature variation
ΔL	mm	Length variation
$\Delta\lambda_B$	nm	Bragg wavelength variation
p_e	-	Strain-optic tensor
ε	$\mu m \cdot m^{-1}$	Strain
α_f	K^{-1}	Optical fiber's coefficient of thermal expansion
ξ_f	K^{-1}	Optical fiber's thermo-optical coefficient
q_i	-	Axis *i*
K_{ij}	-	Linear system transfer matrix coefficients

l	mm	Cavity length
k	-	Positive non-zero integer
v	$m \cdot s^{-1}$	Speed of an electromagnetic wave
f	s^{-1}	Frequency
Δf	s^{-1}	Free spectral range
F	-	Finesse
R	-	Reflectance
l_0	mm	Nominal cavity length
Δl	mm	Cavity length variation
μ_ε	$\mu m \cdot m^{-1}$	Mean strain
H_0	-	Null hypothesis
H_1	-	Alternative hypothesis
S	-	Standard deviation
α	-	Significance level

TABLE OF CONTENTS

1 INTRODUCTION

1.1 Motivation

In applications where crucial system components are frequently or constantly in contact with corrosive fluids or atmosphere, such as in the oil and gas industry, usage of composite materials in the form of full composite-made components and composite fabric reinforcements has grown exponentially, due to low weight-to-strength ratio and high corrosion resistance inherent to these materials.

Metallic produced water pipelines on offshore oil platform are being systematically replaced by adhesive bonded fiber reinforced plastic (FRP) pipelines for their lower weight and high corrosion resistance, generating a demand for FRP inspection techniques.

This lead to heavy investment in adapting and developing inspection techniques to ensure the quality and structural integrity of composite components. Several NDT techniques have been adapted or developed on the last decades to meet this demand, including thermography, ultrasonography, radiography, holography and shearography.

Experience acquired over the years at the Metrology and Automation Laboratory (LABMETRO) in the Federal University of Santa Catarina shows that today, in the oil and gas industry, inspection of composite materials is not optimally conducted.

Access to the inspection site and to the component to be inspect is often difficult, as is the case of pipelines that are buried or installed in confined spaces on oil platforms. Available technology requires experienced personal to interpret measurement results, leading to higher inspection costs. Logistical and financial constraints result in inspection schedules that are seldom enough to guarantee premature failure will not occur.

A promising new approach is to embed several fiber optic sensors into the adhesive layer of the FRP pipes bonded joints for long-term strain monitoring. In order to expand the coverage of NDT techniques on composite pipelines, this study proposes to evaluate the feasibility of this new health monitoring approach.

In addition to adhesive bonded joints between FRP pipes, it is expected that this method can also be used for health monitoring of anti-corrosion FRP reinforcements and FRP repairs applied to metallic pipelines.

1.2 Objectives

1.2.1 General Objective

The main objective of this work is to study, propose and evaluate a health monitoring solution for adhesive bonded joints between pipes utilizing embedded fiber optic sensors.

1.2.2 Specific Objectives

Specific objectives can be seen as the stepping-stones, or a set of requirements, that paves the road towards the fulfillment of the general objective. They can be listed as follows:

- Select a set of fiber optic sensors to be embedded or otherwise integrated to the adhesive bonded joint;
- Determine sensor placement aiming for a balance between intrusiveness and coverage;
- Evaluate the capacity of the devised approach to detect and monitor commonly occurring defects;
- Define procedures and elaborate recommendations to conduct tests on adhesive bonded joints between pipes with integrated fiber optic sensors.

To properly address all listed objectives a series of adhesive bonded joints with integrated instrumentation is to be designed and constructed. Tomography and shearography will be used as support techniques to better understand collected fiber optics sensors data.

1.3 Chapter Summary

This work is structured in six chapters. Chapter two contains a brief review on composite materials. The definition of a composite material is presented, along with several application examples in the oil and gas industry. Some aspects of fiber reinforced plastic (FRP) pipes such as fabrication, adhesive bonded joints between pipe sections and commonly occurring defects are detailed.

Chapter three consists of a review on optical fibers and optical fiber sensors. The reader will come across fiber optics fundamentals and a selection of both single-point and distributed optical fiber sensors

capable of single or multi-parameter measurements. Emphasis is given to Fiber Bragg Gratings, as they are the sensor of choice in this work.

Chapter four discusses the methodology behind the experiments conducted during this work. Experimental procedures, test sample design, instrumentation design and placement plans are detailed.

Chapter five presents discussions based on the data obtained during the execution of the experiments detailed in the previous chapter. Sensor embedding procedure is the first discussion point, followed by detection of defects in the adhesive layer and the effects of the embedded instrumentation on the bonded joint's strength.

Chapter six contains the conclusions to this work. First the objectives presented on chapter one are compared to the results from chapter five to check their completion, then a series of recommendations for the continuation and expansion of this work is presented. The capabilities and limitations of the proposed health monitoring method are discussed as well

1.4 Test Specimen Material

This work originally intended to use fiberglass-epoxy composite pipes as test specimens. Due to time and money constraints, industrial grade CPVC pipes were used instead. The review on composite materials and piping systems has been kept as a reference for future works. Since this study uses relative strain measurements, it is not expected that the change in materials will influence the evaluation of the proposed method.

2 COMPOSITE MATERIALS

Composite is a generic denomination used to describe a composition material whose resulting properties differ significantly from those of its individual components. It is obtained by combining two or more constituent materials with distinct physical or chemical properties. [1][2]

Differently from an alloy, in which the mixing of constituents occurs at atomic scale, mixing occur at macroscopic level in composites and so materials remain separated in the final product. [1]

The use of composites is increasing in various engineering applications due to their inherent characteristics. High strength to weight ratio, high resistance to corrosion, oxidation and to harsh chemicals such as solvents, grease and oil are all examples of desirable properties. [3]

2.1 Basic Concepts

In general, one of the constituent materials in a composite form a continuous phase called matrix and the other constituents are reinforcements, in the form of fibers or particulates, added in to improve the matrix properties. Sandwich panels and laminates do not follow this structure but are still composites by definition. [4][5]

Fibers can be made of light elements like carbon or boron, silica compounds such as silicon oxide, silicon carbide and silicon nitride. Organic materials (C-H-N chains) such as aramid (Kevlar) are also commonly used. [4][5]

Fiber reinforcement represents the major contribution to the composite final toughness, strength and stiffness in fiber directions. Fibers can be weaved into several different fabric styles, from plain weave to satin weave, according to the desired directional properties and lay-up conformability. [4][5]

Particle reinforcement is cheaper and allow for more flexibility in the production and forming of the composite. Gains in stiffness, strength and toughness are lower comparatively to fibers, but increase in hardness and abrasion resistance is unmatched. [6]

Matrixes may be composed of polymer, metal or ceramic materials. It forms the shape of the component, transfers load in and out of the reinforcements, protect fibers from environmental harm and from damage from nearby fiber failure. [4]

Temperature and environmental resistance, longitudinal compression strength, transverse tensile strength and shear strength are properties of the composite that are matrix-dominated. [4]

2.2 Miscellaneous Applications

The following short list of applications clearly illustrates the versatility of composite materials.

2.2.1 Composite Brakes

Carbon-composite (CCM) and carbon-ceramic (CCB) discs have been used since 1980 in motorsports braking systems. CCM discs are made of high performance ceramic matrix composites reinforced with carbon fibers. CCB discs (Figure 2-1) follow the same basic structure but with an added ceramic friction layer on both braking surfaces. [7]

Figure 2-1 - Automotive CCB disc. [8]

2.2.2 Cemented Carbides

Cemented carbides are metal matrix composites reinforced with carbide particles. Usually tungsten carbide (WC), titanium carbide (TiC) and tantalum carbide (TaC). [9][10]

Originally developed for use in tungsten filament drawing for incandescent lamps, cemented carbides were quickly adopted in a number of applications for its unique combination of hardness, wear resistance and high temperature strength. It is often used on metalworking rollers cutting tools and inserts for metal cutting (Figure 2-2). [9][11][12]

Figure 2-2 - Cemented carbide cutting inserts. [13]

2.2.3 Sandwich Panels

Although they do not follow the classic monolithic structure, sandwich panels are also composites by definition. A sandwich panel is composed of a core inserted between two flat plates or laminates. The core increases the moment of inertia of the panel with little impact on its mass, leading to structures that are highly efficient under axial compression and bending. [14][15]

Sandwich panels are used in applications that require very high strength-to-weight ratios, such as aircrafts (Figure 2-3), racing cars, marine vehicles, prefabricated houses and optical breadboards. [15][16]

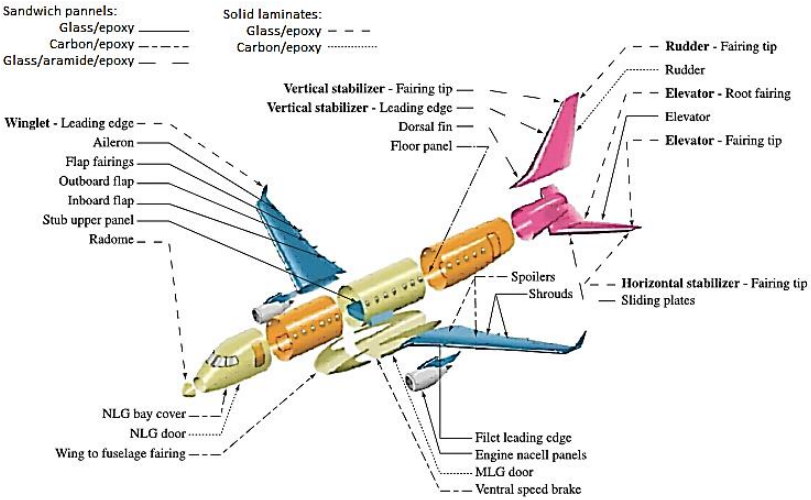

Figure 2-3 - Exploded view of an EMB-170 aircraft fuselage listing various parts made out of composite materials. Adapted from [16].

2.3 Composite Materials in the Oil and Gas Industry

In the oil and gas industry, FRPs are more commonly used in the form of composite pipelines (Figure 2-4), localized patch repairs and anticorrosive patches applied to metallic pipelines, storage tanks (Figure 2-5) and tanker ships. [17][18][19]

Figure 2-4 – Fiberglass-epoxy pipes for marine and offshore applications. [20]

Oil platform and tankers benefit greatly on FRP's light weight, while their inherent corrosion resistance leads to longer lifespan for components in contact with oil, gas, maritime atmosphere and produced water.

Figure 2-5 – Fiberglass-epoxy anticorrosive patch applied to the bottom of an oil storage tank. [17]

Other applications include structural items, composite risers, and various sorts of pressure vessels. [21][22][23][24]

Fiberglass-epoxy pipes are the most commonly used FRP pipes in oil platforms, especially in produced water lines.

2.4 Fabrication of FRP Pipes and Fittings

2.4.1 Glass Fibers Production Process

Figure 2-6 shows a schematic representation of glass fibers manufacturing process. Sand, aluminum and borax (sodium borate) are mixed together and continuously fed to a furnace that heats the mixture to 1250 ºC. Molten glass flows through a perforated platinum plate and is then drawn to the right diameter. The fibers are cooled with water sprays and directed to a treadmill or cylinder to be coated with a protective layer that allows posterior handling. Finally, individual filaments are united into strands, typically in groups of 204 filaments, which are wound and stored.

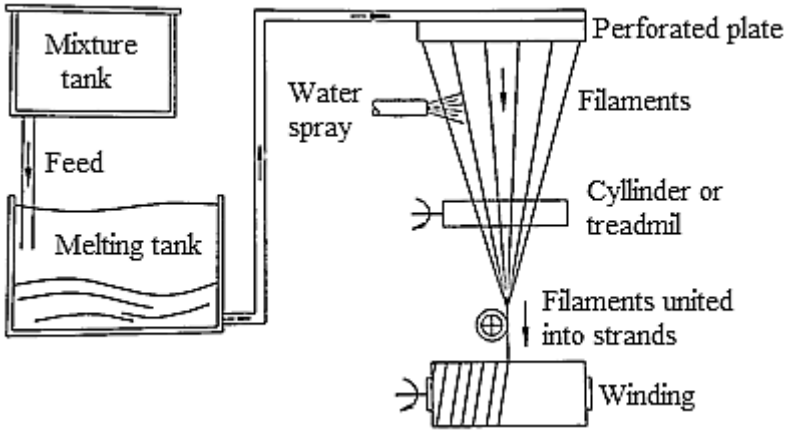

Figure 2-6 – Schematic representation of a glass fiber production line. Adapted from [1].

2.4.2 Filament Winding

Filament winding is a composite materials production process that is greatly suited for axisymmetric components such as pipes and most fittings. Multi-axis machines are also available for components that are more complex. [4][24][25]

Continuous strands or filaments of fibers are bathed in resin before being led to a rotating mandrel, where they are laid down at high speed, as illustrated in Figure 2-7.

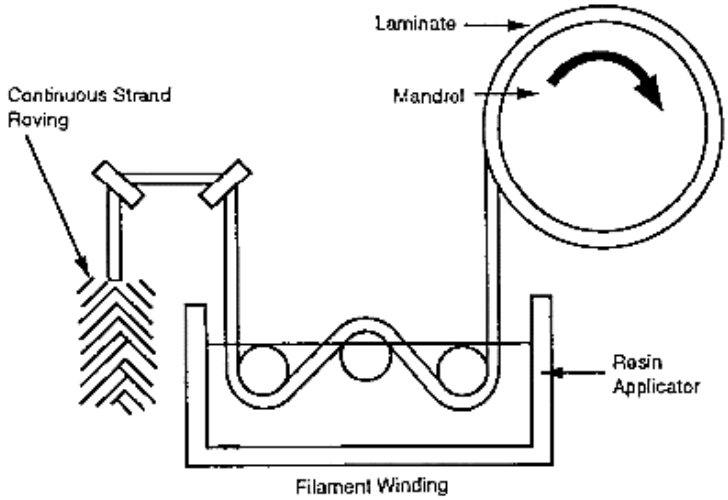

Figure 2-7 - Schematic diagram of filament winding. [25]

Fibers can be laid down with high precision in predefined paths by adjusting the angular velocity of the mandrel and the movement pattern of a moving platform, as shown in Figure 2-8. [4][24][25]

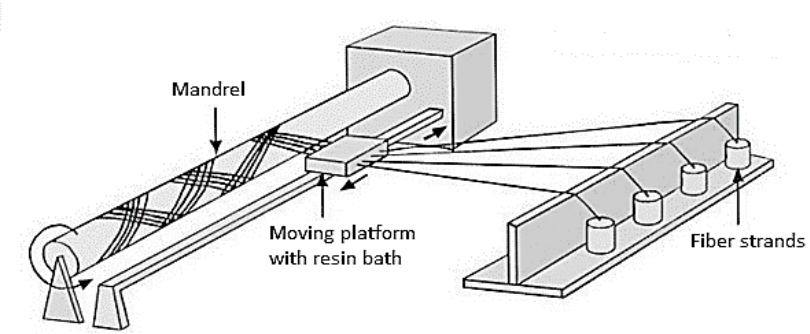

Figure 2-8 - Winding pattern control scheme. [26]

Common patterns are polar, hoop or helical (Figure 2-9). Winding angle, fiber tension and the amount of resin in each layer are

the main control parameters to ensure the desired stiffness and strength are obtained. [4][24][25]

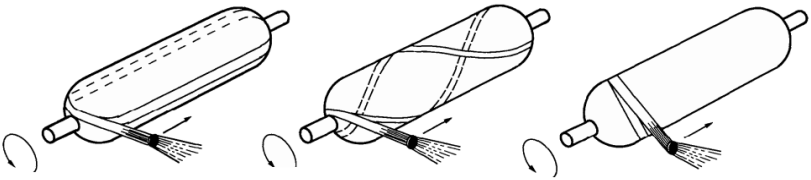

Figure 2-9 - From right to left: Polar, helical and hoop winding. Adapted from [25].

After winding, the composite coated mandrel is removed and transported to an oven, if heat curing is needed, or a clean room for room temperature curing. The mandrel can be removed and reused or remain as part of the composite after the curing process ends. [4][24][25]

2.5 Adhesive Bonded Joints

Adhesive bonding is a method for joining metals, plastics, ceramics and composites in which an adhesive, placed between the surfaces to be joined, solidifies to consolidate the union. [27]

In comparison to classical mechanical joining methods, such as screwed or riveted joints, it presents a series of advantages. Bonded joints are lighter, cheaper and are more resistant to damage. Fewer parts are required to complete the joining process, there is no need to drill the adherends and loads are distributed over larger areas. They are more flexible and inhibit crack propagation on the adhesive layer, leading to a longer fatigue life. [27][28][29]

Nonetheless, they are difficult to inspect with non-destructive methods and all surfaces in contact with the adhesive must be carefully cleaned and prepared beforehand. Mechanical properties may change due to moisture absorption and service temperature is limited by both the adhesive and curing cycle parameters. Since it is difficult to disassemble adhesive bonded joints without incurring in irreparable damage this is often considered a permanent joining method. [29]

Specialized literature contains plenty of examples of adhesive joints suitable for all kinds of mechanical loads. Some of these configurations are shown in Figure 2-10.

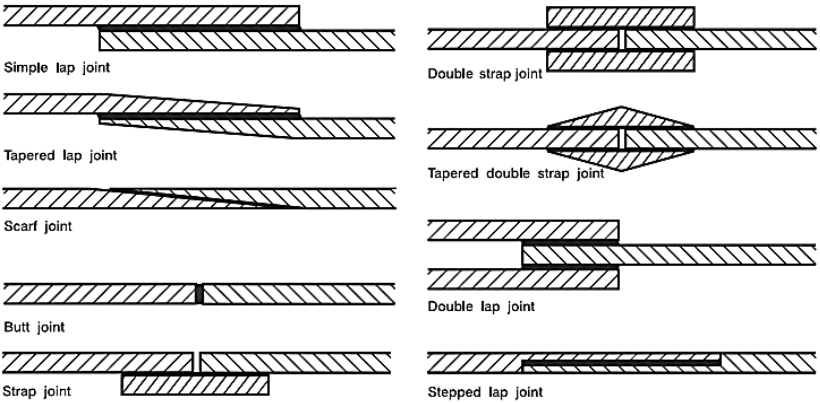

Figure 2-10 - Several types of adhesive bonded joints. Adapted from [28].

2.5.1 The Bell-and-Spigot Joint

The bell-and-spigot joint is an asymmetric junction where a smooth walled bell is sized to accept either a smooth or gasketed pipe spigot. Examples of this type of joint are depicted in Figure 2-11. It is widely used to join cast iron and ferroalloy pipes, vitrified clay pipes and plain, reinforced or asbestos cement pipes. It is also the most used method for joining plastic pipes. [30][31]

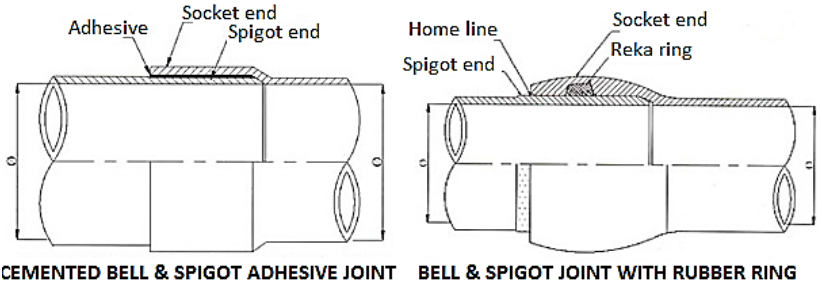

Figure 2-11 - Bonded and gasketed bell-and-spigot joint. Adapted from [32].

Sealing method varies according to the pipe material and the operating pressure in the line. Rubber O-rings, gaskets and mortar with sealing rings are adequate for liquid lines pressurized up to 1.5 MPa (15 bar) and 0.1 MPa (1 bar) for gases. For higher operating pressures, welded cast iron pipes or adhesive bonded composite pipes must be used. [30][31]

In adhesive bonded joints, the bell's inner surface and the spigot's outer surface can be cylindrical or conical (tapered).

2.5.2 Tubular Single Lap Joint

From Figure 2-11 it is evident that when both surfaces are not tapered, the bell-and-spigot joint is very similar to a tubular single lap joint (Figure 2-12), which is simpler and has been a subject of study to researchers in recent years.

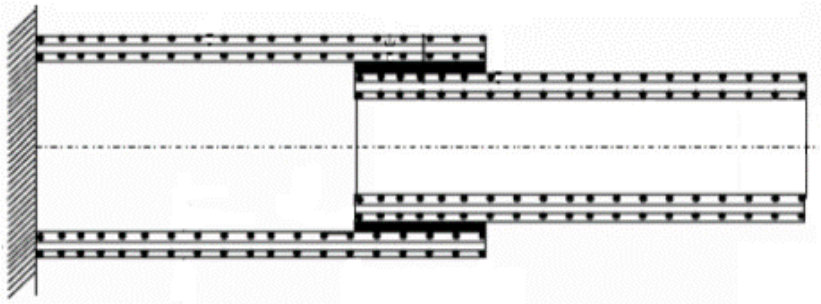

Figure 2-12 - Tubular single lap bonded joint. Adapted from [33]

The behavior of tubular single lap bonded joints in FRP pipes to axial, pressure and torsional loads have been studied analytically, by finite elements method, and experimentally. [33][34][35][36][37]

Das and Pradhan [33] show that the state of stress in the bonded joint is fully tridimensional, due to the free edges, differential elasticity and coupling between rotation, stretching and bending.

Although studies performed by Das [33] and Oh [36][37] proposed consistent failure conditions for interfacial failure and adhesive failure, the mathematical equations often require the input of all three principal strains or up to six stress components.

2.6 Quality Control and Non-Destructive Inspection

When compared to metals, composites are more susceptible to damage and introduction of defects upon manufacturing and handling. In FRPs, defects are usually introduced during manufacturing, mainly due to wrong number of composite plies, wrong curing temperature, poor resin choice, foreign-body inclusions or poorly sealed vacuum bags. [16][38]

When inspecting adhesive bonded joints between FRPs, the most common defects are delamination and debonding. These defects have various causes, such as trapped air, catalyst mixed in excess to the resin, propagation of cracks through the FRP's matrix and lack of adhesive.

Commonly occurring defects, their description and most likely causes are summarized in [16][17][18].

Table 2-1 - Commonly occurring defects and their likely cause. [17][18]

Defect	Description	Likely Cause
Delamination	Separation between layers of a laminate.	Poor compatibility between constituent materials, excess use of catalyzer.
Debonding	Separation between components/interfaces that should be bonded.	Poor compatibility between constituent materials, poor control over manufacturing.
Inclusions	Presence of foreign objects inside the material.	Improper cleaning of the glued surfaces, contaminated resin or plies.
Porosity	Presence of numerous visible pores.	Air trapped in resin, inclusion of volatile substances.
Chipping	Small broken pieces of the components in the vicinity.	Bad handling, impact.
Fiber breakage	Presence of ruptured fibers.	Overload, impact.
Swelling	Dimensional changes.	Moisture absorption.
Elongation	Axial dimensional change	Overload.
Fracture	Component rupture.	Overload.

NDT techniques are preventive tools for diagnosing component malfunction, deterioration and failure. Data acquisition for assessing structural integrity is conducted in a non-invasive way. [39]

Despite the existence of a relatively large number of techniques, only a few are suitable for inspecting composites due to their characteristic anisotropy. In addition to visual inspection, the most used NDT techniques for composite are holography [39], radiography [40] ultrasonography [41], thermography [42], shearography [43] and computed tomography [44].

Shearography and computed tomography are complimentary analysis techniques used in this work.

2.6.1 Computed Tomography

Computed tomography (CT) is an extension of computed radiography. Both techniques make use of differential absorption of X-rays by local variations in a material's density, thickness and/or composition. Both use electronic X-ray detectors, outputting digital images by default. [44][45][46]

The difference between the two is that CT latter allows a full three-dimensional reconstruction of an object and its internal structure by combining multiple radiographic images taken from different angles. This can be achieved in two ways: by rotating the object (Figure 2-13) or by rotating the X-ray source and detector around the object. [44][45][46]

In FRPs, tomography allows the detection of impact damage, crushed core (Figure 2-14) and other internal defects such as delamination, porosity and cracks. [44][45][46]

In this work, CT is used to check the position of embedded sensors and artificially inserted defects in bonded joints of test specimens.

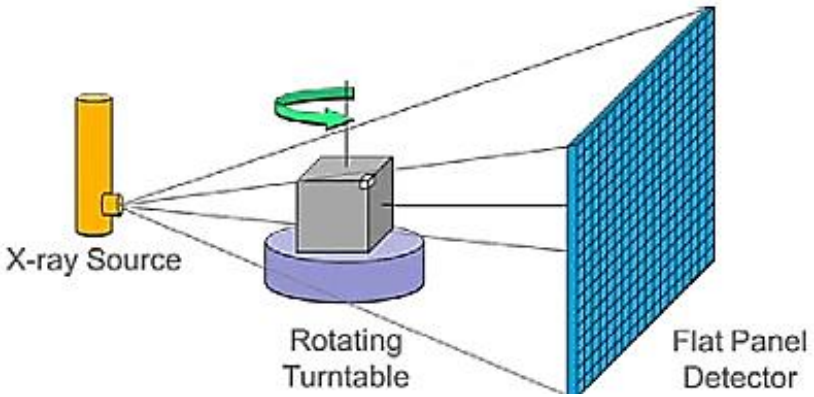

Figure 2-13 – CT scan with rotating turntable. [46]

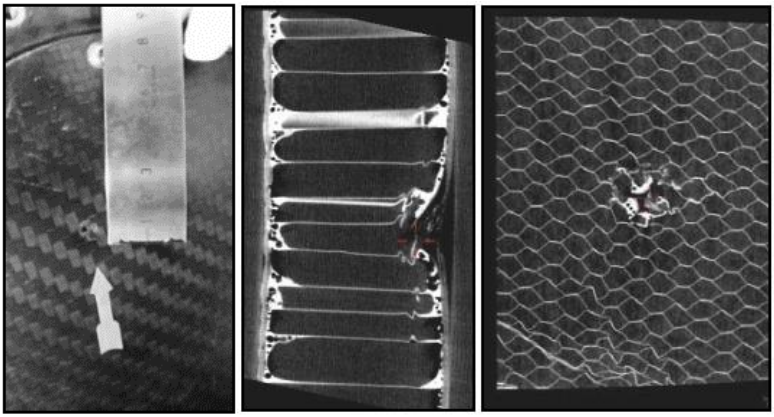

Figure 2-14 - CT measurement (center and right) of an impacted sandwich panel (left) exhibiting localized crushing of the honeycomb core. [46]

2.6.2 Digital Shearography

Shearography is a quasi-common-path laser interferometry technique capable of contactless measurement of strain fields. Being a quasi-common-path interferometry technique allows the use of short coherence length illumination and leads to reduced sensibility to environmental disturbances. This makes shearography a robust technique for use in the industry and in the field. [47][48]

The name of this technique comes from its use of speckle pattern shearing interferometry. Laser speckle phenomenon (Figure 2-15) manifests from the interferometric superposition of coherent light scattered by a diffusely reflecting surface. [47]

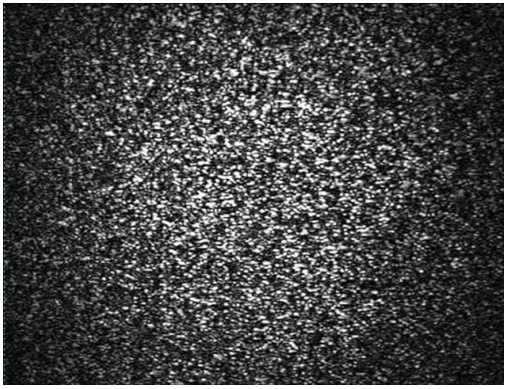

Figure 2-15 - Laser speckle pattern. [49]

Shearography measurement requires the superposition of two images from the illuminated surface with a slight shear between them. Shearing interferometers are used to simultaneously split and shear the reflect wavefront. Lateral shearing interferometers (Figure 2-16) are the most common, but is also possible to use radial, rotational and reverse shear interferometers. [43][47]

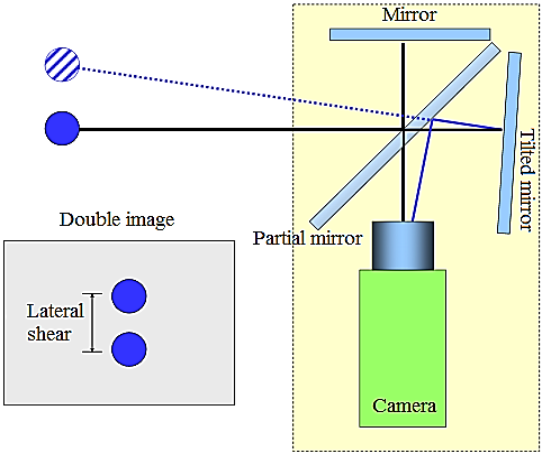

Figure 2-16 - Modified Michelson interferometer for lateral shearing interferometry. Adapted from [43].

The superposition of the slightly sheared images creates a speckle interferogram, which has an intensity distribution directly related to the surface's geometry. When the studied object (Figure 2-17) is subjected to a loading, its surface geometry changes and so does the intensity distribution (Figure 2-18) of the speckle interferogram. [43][47]

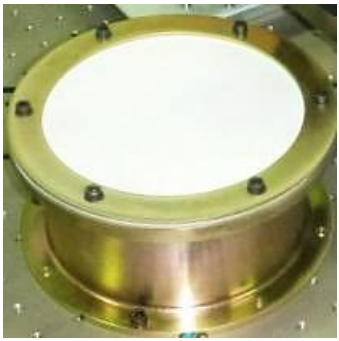

Figure 2-17 – Cylindrical pressure vessel with a flat plate cover. [50]

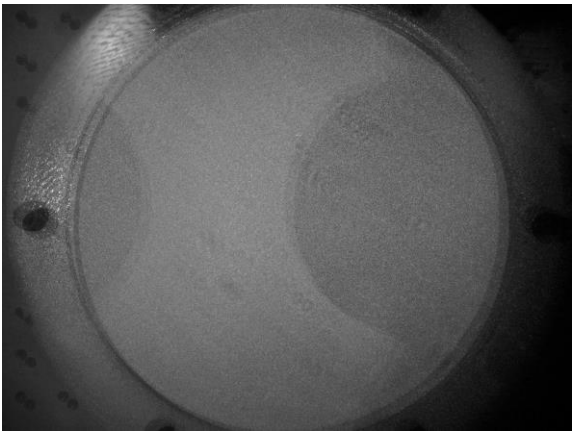

Figure 2-18 - Intensity map of a speckle shearogram of a flat circular plate cover of the pressure vessel shown on Figure 2-17. [50]

By capturing a series of speckle interferograms, it is possible to extract phase information from the intensity maps (Figure 2-19). [43][47]

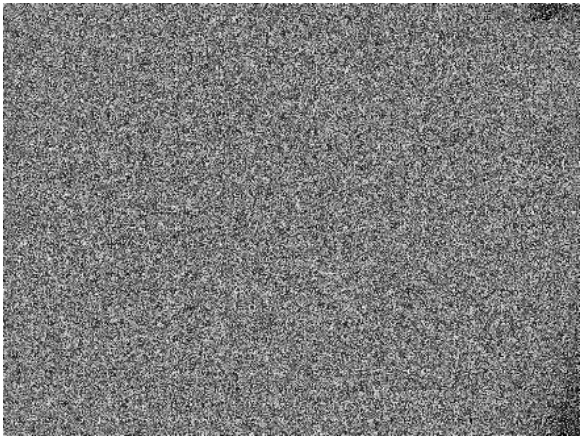

Figure 2-19 - Phase map extracted from a series of intensity maps. [50]

Subtracting a phase map obtained before applying a load from a phase map obtained after a load is applied results in a fringe map (Figure 2-20). The fringe map is related to the change in the surface's strain field in response to the applied load. [43][47]

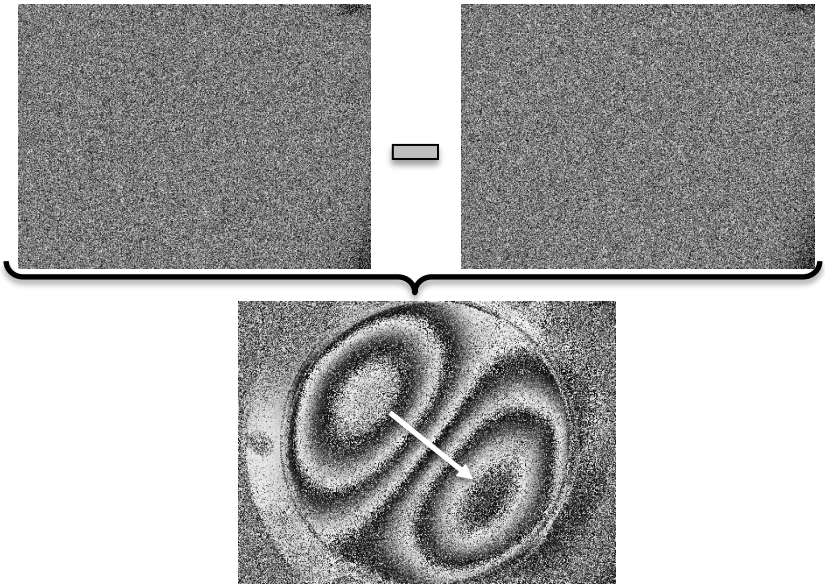

Figure 2-20 - Fringe map obtained from subtracting phase maps. Applied load: 4 kPa (30 mmHg) internal pressure variation. Shear amount: 3 mm. Shear direction: as pointed by the arrow. Adapted from [50]

Internal defects in composite materials are revealed by their effect in the surface strain field, as shown in Figure 2-21. [43][48][51]

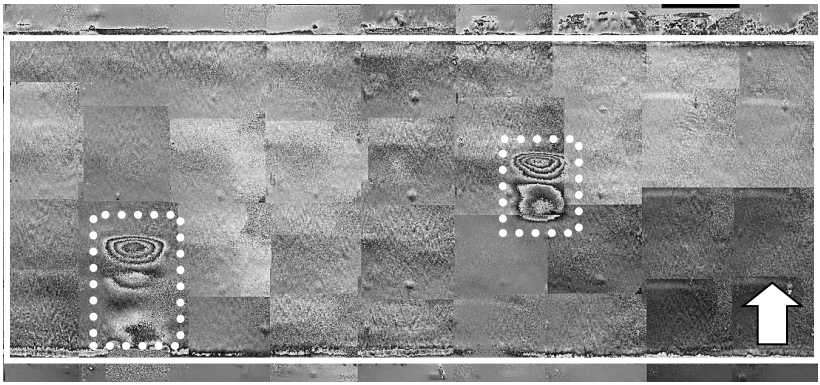

Figure 2-21 - Composition of fringe maps from a glass/epoxy anti-corrosive sleeve applied to a steel pipe. Areas delimited by dots exhibit anomalies caused by sub-surface defects. [51]

In this work, shearography is used to study the effects of the embedded sensors and artificial defects in the strain fields on the surface of the adhesive bonded joints of the test specimens.

2.7 Structural Health Monitoring

SHM in composite can be performed in many ways, including conventional sensors such as electric strain gages [52], or modern methods [53] using different types of sensors and transducers embedded in the composite.

Influence of embedded sensors on the mechanical properties of composite components is a controversial topic. Some studies observe up to 70% reductions in yield strength, 20% reduction in the modulus of elasticity and up to 10% reduction of the performance under tensile load, depending on the orientation of the sensors in relation to the fibers in composite laminates [54]. Other studies show mixed results on the influence depending on size and type of sensor and the constructive aspects of the tested composite [54][55][56][57]. There has also been reports of minimal or no negative effects [58].

Despite the mechanical degradation discussion, this approach has shown very promising results in several applications, such as detection and monitoring of debonding in adhesive bonded joints [59], monitoring of strain gradient in adhesive composite joints [60] and life cycle monitoring of curved composite parts. [61]

3 FIBER OPTIC SENSORS

Fiber optic sensors were chosen for this study for having some important advantages [62] over electronic sensors, considering the context of composite pipelines in off-shore oil and gas rigs:

i. They are small: the typical fiber sensor has an uncoated diameter of 125 μm and around double this value for coated fibers. Their small frame allows the embedding of sensors into delicate composite structures with minimal impact on mechanical properties.

ii. With proper choice of coating and connectors fiber sensors can be made environmentally rugged, being able to withstand the bonded joints fabrication and off-shore environments.

iii. They are passive sensors: not needing electrical power makes them safe to use in classified environments.

iv. High multiplexing capabilities means simpler and less bulky setups. Off-shore oil and gas rigs usually have a great number of pipelines grouped in tight spaces.

3.1 Optical Fibers

Telecommunications have been revolutionized by fiber optic technology as mass production techniques and technical improvements led to superior performance and reduced costs. Now a sensing revolution is on the making, as engineers combine product outgrowths of fiber optic telecom with optoelectronic devices. [63]

Novel fiber sensors, with the potential of replacing many of the existing environmental sensors and fulfilling roles where current sensor technology falters, are quickly being researched and developed. [63]

An optical fiber is a dielectric waveguide capable of transmitting optical signals over great distances with attenuation as low as 0.2 dB/km [64]. The typical structure of an optical fiber is shown in Figure 3-1.

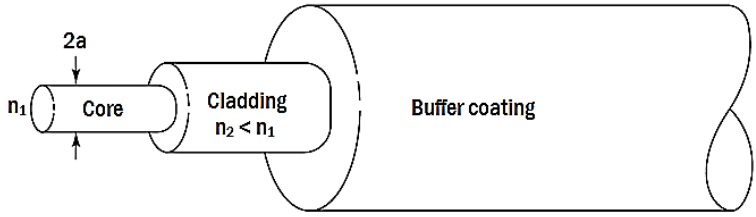

Figure 3-1 - Typical structure of a silica optical fiber. Adapted from [65].

The core is the waveguide itself, a solid glass rod that traps and conducts light by total internal reflection. It is usually made of high purity silicon dioxide (SiO_2). Plastic fibers are also widely used. [65]

A cladding is not strictly required for transmitting light, but it reduces dispersion loss due to discontinuities on the core's surface, provides mechanical protection and prevents contaminants absorption into the core. Notice that the index of refraction n_2 of the cladding is greater than the index of refraction n_1 of the core. [65]

Most fibers are coated with a plastic, ceramic or metallic buffer. Buffer coatings provide extra mechanical protection by isolating the fiber from small irregularities on adjacent surfaces, which would otherwise induce microbending loss. It also protects the fiber from scratches and abrasion. [65]

Any light wave coupled into the fiber is heavily attenuated if it refracts into the cladding instead of bouncing back by total internal reflection. Light rays entering the core of a fiber with uniform index of refraction n_1, from a medium with index of refraction $n < n_1$, are transmitted forward as long as they belong to the acceptance cone depicted in Figure 3-2. [65]

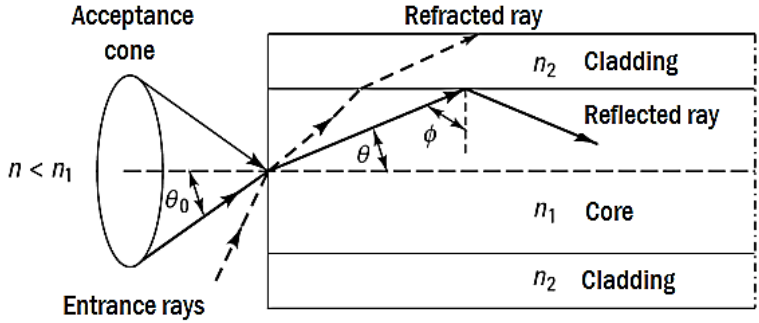

Figure 3-2 - Acceptance cone in an optical fiber with uniform core index of refraction. Adapted from [65].

From Snell's law, total internal reflection will occur for an incidence angle ϕ that satisfies the condition presented in Equation 3.1. [65]

$$sin(\phi) \geq {}^{n_2}/_{n_1} \tag{3.1}$$

Working backwards from this it is easy to show that the maximum value for θ_0 can be determined by applying Equation 3.2. [65]

$$n\,sin(\theta_{0,max}) = \sqrt{n_1^2 - n_2^2} \approx n_1\sqrt{2\Delta} \tag{3.2}$$

Equation 3.2 also defines the numerical aperture NA for an optical fiber with a uniform index of refraction at its core. The parameter Δ is the core-cladding index difference, as defined by Equation 3.3. [65]

$$\Delta = 1 - \left({}^{n_2}/_{n_1}\right) \tag{3.3}$$

The approximation on the right side of Equation 3.2 is valid when $\Delta \ll 1$. Typically, for a given value of n_1, n_2 is chosen such that Δ is equal to 0.01. [65]

3.1.2 Fiber Types

Looking at Figure 3-2 from a ray optics perspective, it is evident that light entering the fiber with many different angles $\theta_0 < \theta_{0,max}$ can be guided. However, the number of guided modes is finite. Solving Maxwell's equation for a circular dielectric waveguide shows that only certain modes entering the fiber with $\theta_0 < \theta_{0,max}$ are guided. [63]

Fibers can be classified according to the number of allowed modes and the index of refraction profile in the core region. Figure 3-3 presents a comparison between conventional optical fiber types.

As the name suggests, multimode fibers allow a large number of guided modes simultaneously. A multimode step-index fiber usually allows around 10^4 individual propagation modes. The number of guided modes, or modal volume, M can be approximated by Equation 3.4 for large V values. [63][65]

$$M = {}^{V^2}/_{2} \tag{3.4}$$

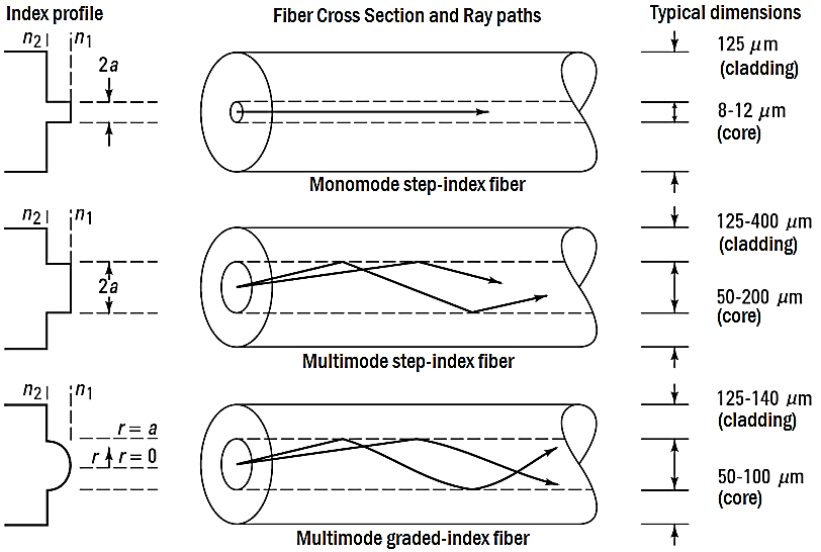

Figure 3-3 – Fiber types by number of guided modes and index of refraction profile. Adapted from [65].

Where V is the normalized frequency, as defined by Equation (3.5), for a light wave of wavelength λ traveling in a fiber of core radius a. [65]

$$V = \left(\frac{2\pi a}{\lambda}\right)\sqrt{n_1^2 - n_2^2} = \left(\frac{2\pi a}{\lambda}\right)NA \qquad (3.5)$$

Guided modes follow slightly different paths and experience slightly different refractive indexes in the core, causing modal dispersion. This phenomenon limits the fiber bandwidth, reducing the amount of data transmitted per unit of time. [63]

Multimode graded-index fibers mitigate this problem by changing the core index of refraction profile to make the core act as a series of lenses that periodically focus the light beam as it propagates down the fiber. This technique reduces the amount of individual propagation modes down to about 300 for a typical graded-index fiber. [63]

The ultimate solution to manage modal noise and maximize bandwidth came in the form of monomode fibers. By greatly reducing the core diameter until it approaches the wavelength of the guided light,

diffraction effects dominate and light becomes constrained to propagate only along the waveguide axis. When $V \leq 2.405$ only one mode is allowed to propagate, this is referred to as the cutoff condition. [63]

The monomode fiber described above is not truly monomode in a sense that two modes with degenerate polarization states are allowed to propagate. There are various solutions to remove this degeneracy and let a single linear polarization state propagate. Figure 3-4 shows the most common polarization maintaining fibers. [63]

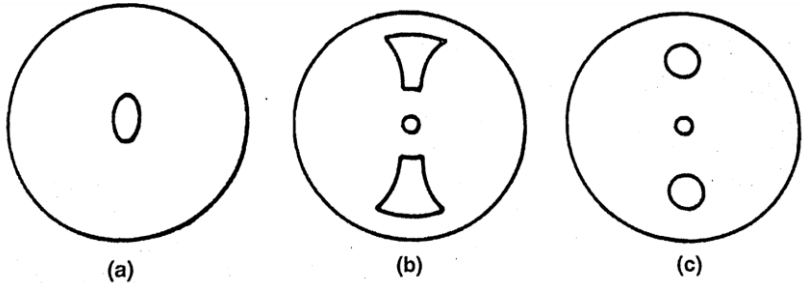

Figure 3-4 – Types of polarization maintaining fibers: (a) elliptical core fiber; (b) bow-tie stress-induced birefringent fiber; (c) stress-induced birefringent fiber using bars. [63]

Elliptical core fibers are the simplest solution for maintaining polarization. If the core-cladding index difference is sufficiently high, light with linear polarization aligned along the major axis will retain its polarization state. [63]

Fabricating a fiber with built-in stress causes stress birefringence, i.e., the stress induces an index of refraction difference between a major and a minor axis. Light propagating along the major axis preserves its polarization state. [63]

There is also a type of fiber called polarizing fiber that is designed to induce high transmission loss for undesired polarization states, allowing only a single state to propagate. This kind of fiber is very useful in optical sensing applications that rely on the control of the polarization state. [63]

3.1.3 Signal Attenuation

There are three main attenuation mechanisms for light signals traveling through an optical fiber. Absorption, which is related to the fiber material; scattering, which is dependent on both fiber material and

waveguide imperfections; and radiative losses, originated from perturbations of the fiber geometry. [63][65]

Total absorption is the combination of effects from three distinct absorption mechanisms: absorption by atomic defects in the glass composition, extrinsic absorption by impurity atoms and intrinsic absorption by basic fiber constituent atoms. [65]

Atomic defects in the glass structure are missing molecules, high-density atom clusters and oxygen defects. Absorption loss from atomic defects is negligible in comparison with the other absorption mechanisms under normal circumstances, but can become significant (Figure 3-5) if the fiber is subjected to ionizing radiation. [63][65]

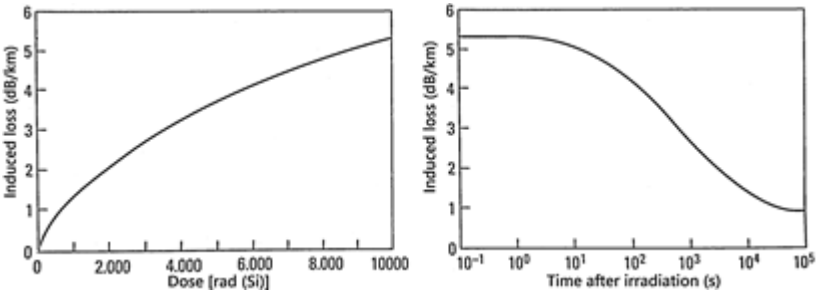

Figure 3-5 – Left: Induced absorption loss due to steady exposure to ionizing radiation (1 rad(Si) = 100 erg/g = 0.01 J/kg). Right: Recovery as a function of time after radiation exposure has ceased. Adapted from [65].

The presence of OH^- (water) and transition metal ions impurities in the fiber is the dominant absorption mechanism. Even 1 ppm concentration of these impurities can lead to absorption losses up to 4 dB/km. Improvements to the fiber fabrication process, to significantly reduce the presence of contaminants, were paramount in achieving the low-loss fibers (0.2 dB/km) in use today. Table 3-1 contains absorption loss information for commonly occurring impurities. [63][65]

Intrinsic loss occurs due to absorption of photons by electronic and vibrational transitions in the fiber. Electronic transitions occur mainly in the ultraviolet for Si based fibers and its effects decrease exponentially as wavelength increases. Vibrational transition losses are stronger in the 8 to 12 μm region of the spectrum. [63][65]

Table 3-1 – Absorption loss in SiO_2 glass due to 1 ppm of water-ions and some transition metal impurities. [65]

Impurity	Loss due to 1 ppm of impurity (dB/km)	Absorption Peak (nm)
Iron: Fe^{2+}	0.68	1100
Iron: Fe^{3+}	0.15	400
Copper: Cu^{2+}	1.1	850
Chromium: Cr^{2+}	1.6	625
Vanadium: V^{4+}	2.7	725
Water: OH^-	1.0	950
Water: OH^-	2.0	1240
Water: OH^-	4.0	1380

Scattering loss arises from fluctuations of the index of refraction due to compositional fluctuations, microscopic density variations, structural inhomogeneities and/or defects introduced in the fiber manufacturing process. The index of refraction fluctuation is small compared with the wavelength, causing Rayleigh scattering of the transmitted light [63][65]. For single component glass, the scattering loss at a given wavelength λ can be approximated by Equation 3.6 [65].

$$\alpha_{scatt} = \frac{8\pi^3}{3\lambda^4} n^8 p^2 k_b T_f \beta_T \tag{3.6}$$

Where p is the photoelastic coefficient, k_b is the Boltzmann's constant, β_T is the isothermal compressibility of the material, and the fictive temperature T_f is the temperature at which the density fluctuations are frozen into the glass as it solidifies after the fiber drawing process.

Note that α_{scatt} in Equation 3.6 is given in *nepers* (base *e* units); one can convert it to dB for optical power attenuation calculations by multiplying α_{scatt} by $10 \log e = 4.343$. [65]

Finally, radiative losses occur due to macroscopic and microscopic bending. Microbending locally disrupts total internal reflection at the core-cladding boundary, leading to light leakage as shown in Figure 3-6. [63][65]

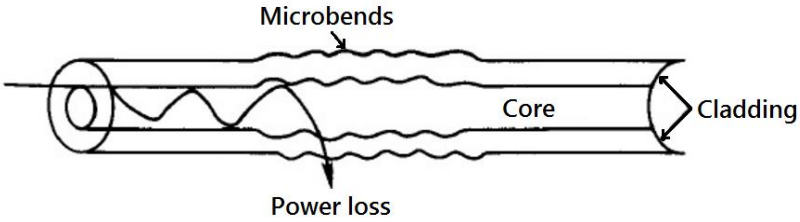

Figure 3-6 - Microbending loss mechanism. Adapted from [65].

Macroscopic bending leads to power loss by two distinct mechanisms. The first loss mechanism is similar to microbending loss, where the local curvature of the fiber can lead to partial reflection at the core-cladding interface, as illustrated in Figure 3-7. [63]

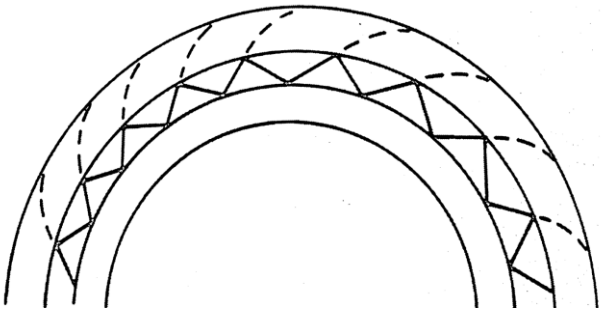

Figure 3-7 – Bending induced loss by partial internal reflection. [63]

The second loss mechanism can be explained by modal analysis of the propagating light wave. Light ray representation is just an approximation of the behavior of light in a waveguide, in reality a propagating mode is not fully restrained to the core of the fiber. Any bound core mode has an evanescent field tail in the cladding that moves with the field in the core and decays exponentially with the distance from the core. A guided mode field in a curved optical waveguide is represented in Figure 3-8. [65]

From Figure 3-8 it is evident that the field tail further away from the center of curvature has to travel at a higher speed to keep up with the field in the core. At a distance x_c from the center of the core, the field tail has to move at the speed of light to follow the core field. Since the field would need to move faster than the speed of light for $x > x_c$, which is not possible, the optical energy in this region radiates away. [65]

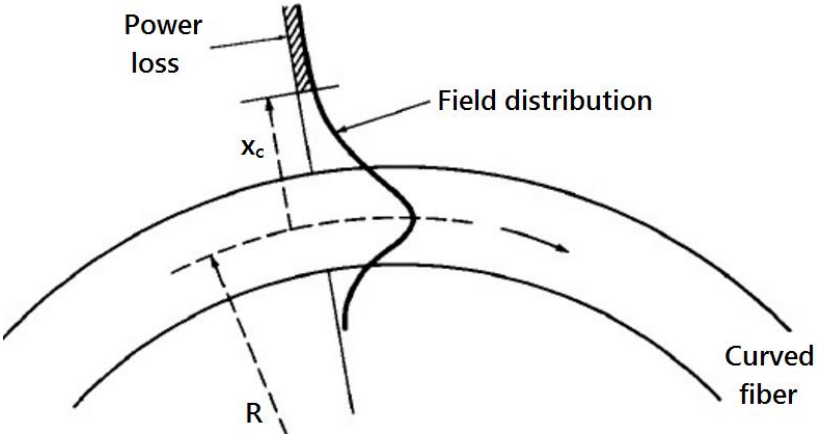

Figure 3-8 - Bending induced loss in evanescent field tail. Adapted from [65].

3.1.4 Pulse Dispersion

As it propagates through a waveguide, a light signal not only experiences attenuation but it also becomes increasingly distorted. Light pulses get progressively wider and can superpose with adjacent pulses. This pulse widening is referred as pulse dispersion or pulse spreading, and it can be explained by examining how the waveguide affects the group velocity of guided modes. [65]

Dispersion effects can be divided in three categories; intermodal dispersion, intramodal dispersion and polarization mode dispersion.

Intermodal dispersion is a distortion mechanism exclusive to multimode fibers. Figure 3-3 illustrates that each mode propagates in a slightly different path inside the fiber. Some modes follow a longer path to get from one point along the fiber axis to another point, and thus have lower axial group velocity. Slower modes lag behind faster modes and the multimode pulse broadens. The maximum pulse broadening Δt, which corresponds to the difference between the time the fastest mode and the slowest mode take to travel down a fiber of length L, can be determined by Equation 3.7. [65]

$$\Delta t = t_{max} - t_{min} = \frac{Ln_1^2}{cn_2}\Delta \tag{3.7}$$

Where L is the fiber length and Δ is the core-cladding index difference as defined in Equation 3.3.

Intramodal dispersion occurs within a single mode, it is mainly caused by material dispersion and waveguide dispersion. Material dispersion is derived from the fact that the index of refraction of the fiber core is a function of wavelength, and that every light source has non-zero spectral width. Each wavelength propagates with a slightly different speed, broadening the pulse. [65]

Waveguide dispersion occurs because part of the optical power propagates in the cladding, as shown in Figure 3-8. Since the core and the cladding have different refractive indexes, light moves at different speeds in these regions, broadening the pulse. This effect is more pronounced in monomode fibers, in which the reduced core diameter means more light propagates in the cladding. [65]

Polarization mode dispersion is a direct result of birefringence along the fiber. Birefringence can be caused by intrinsic factors, such as built-in stress or circularity error in the core; and extrinsic factors, like lateral compression, torsion or flexure. Under these conditions orthogonal polarization modes will undergo dispersion as they experience distinct refractive indexes, as represented in Figure 3-9. [65]

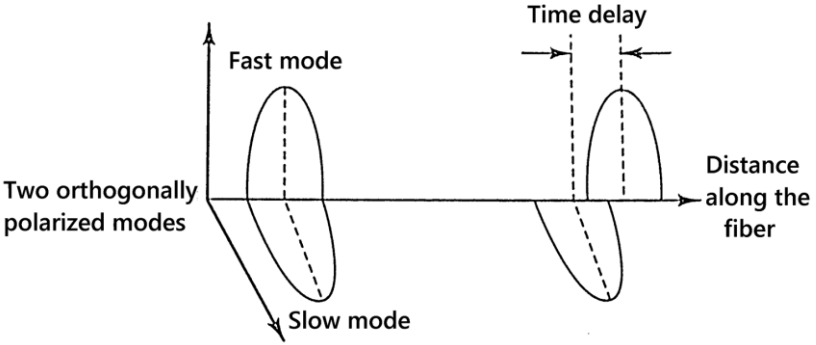

Figure 3-9 - Polarization mode dispersion along birefringent fiber. Adapted from [65].

3.2 Fiber Bragg Gratings (FBG)

The phenomenon of photosensitivity in optical fibers, in which fiber gratings are based on, was first observed in 1978 during experiments with germanium doped silica fibers. Germanium is the most used dopant in low loss fused silica optical fibers to raise the core's index of refraction. As it replaces silicon atoms in the glass structure, germanium creates structural defects. Ultraviolet radiation can

modify the nature of the defects, leading to changes in the local refractive index. [64]

Since then fiber gratings applications on telecommunications and sensors has been widespread. Applications of this technology include stabilization of laser diodes to pump fiber light sources, repeater links in telecommunication lines, wavelength division multiplexing, dispersion compensation on long distance fiber links and a multitude of grating-based fiber sensors. [63][64]

3.2.1 Fundamentals

In their 1978 study, Hill *et al.* [66] describe how standing wave patterns, from a visible argon-ion laser launched into an optical fiber and back-reflected from the fiber end, created a periodic modulation of the core refractive index that acts as a reflection filter. This laid the foundation for fiber reflection gratings research.

While research on photosensitivity and reflection grating writing with transmitted light continued, Meltz *et al.* [67] demonstrated a reflection grating for visible light written with interfering UV beams external to the optical fibers, making modern compact high-reflectivity fiber Bragg gratings possible.

Figure 3-10 illustrates what happens when a broadband signal traveling down an optical fiber passes through a FBG. The FBG acts as a passive narrowband reflection filter. The resulting signal can be analyzed from both ends of the fiber, as the main parameter of interest is the peak reflected wavelength or the corresponding transmission local minimum wavelength, usually referred as the Bragg wavelength λ_B.

The value of λ_B is directly related to intrinsic FBG parameters: the grating period and refractive index change; and extrinsic factors such as strain and temperature. By tracking how λ_B varies to changes in strain and temperature it is possible to use the FBG as a sensor and measure these changes.

3.2.2 Fabrication

The grating writing method used by Meltz *et al.* [67] is referred as holographic method. An amplitude division interferometer is used to divide and recombine an UV beam, the resulting interference pattern creates a periodic modulation of the refractive index in the fiber core, as shown in Figure 3-11.

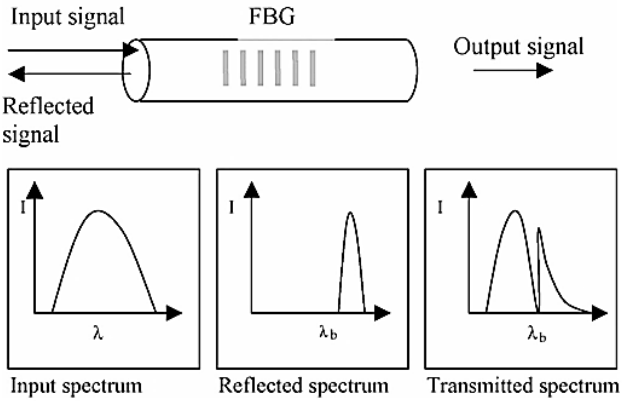

Figure 3-10 - Reflected and Transmitted Spectrum of a fiber Bragg grating. [53]

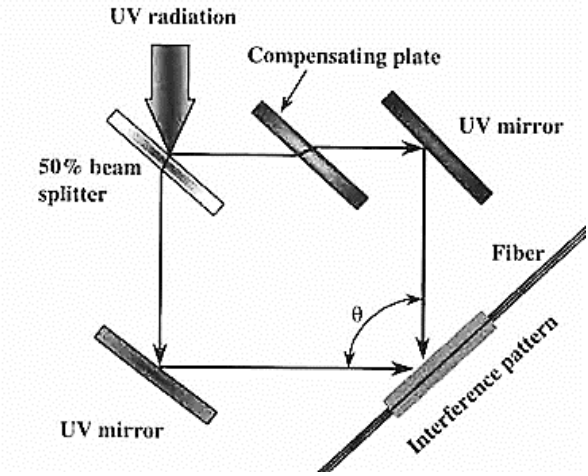

Figure 3-11 – Typical setup for holographic writing of Bragg gratings. [64]

Substitution of the classic holographic setup for a phase mask and a set of mirrors (Figure 3-12) resulted in a much more flexible writing method. By rotating and moving the mirrors, it is easy to adjust the grating length and period. [64]

Grating inscription automation is available in the form of draw towers (Figure 3-13), a process in which fiber drawing and grating inscription processes are synchronized. [68]

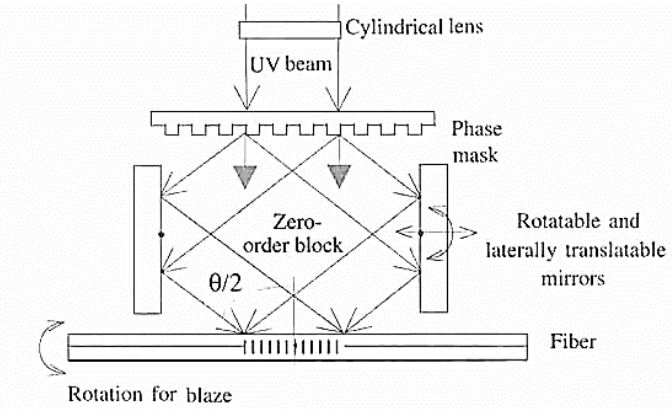

Figure 3-12 - Bragg grating writing with a phase mask interferometer. [64]

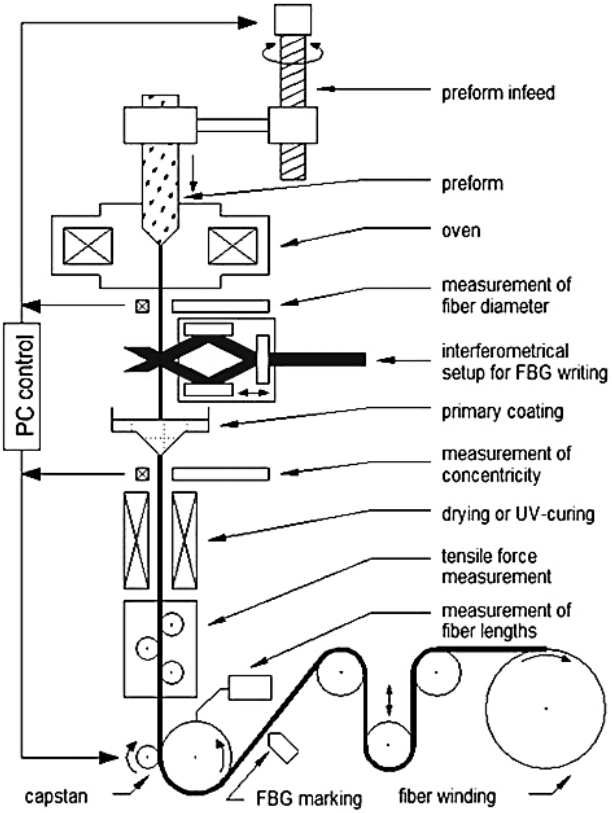

Figure 3-13 - Draw tower grating inscription setup. [68]Figure 3-13

3.2.3 Strain and Temperature Measurement

As discussed in the previous sections, FBGs are narrowband reflection filters with a well-defined peak reflected wavelength λ_B that shifts when strain or temperature varies.

By modelling the periodic index of refraction modulation as multiple layers (Figure 3-14) with slight different refractive indexes, it is possible to derive how λ_B responds to strain and temperature variations without resorting to complicated waveguide modal analysis. [69]

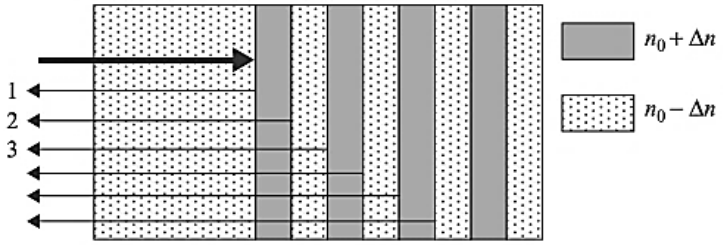

Figure 3-14 - Multiple reflections in a multilayer structure. [69]

As light traverses the layered structure of mean index of refraction n_0, it experiences partial reflection in each interface between the regions of higher and lower refractive index. These multiple reflections can interfere with each other and the wavelength of maximum reflectivity λ_B will be the one with strongest constructive interference. It can be shown that for this model λ_B is given by Equation 3.8, where Λ is the period of the refractive index modulation. [69]

$$\lambda_B = 2n_0\Lambda \tag{3.8}$$

For an optical fiber, the only difference is that instead of n_0 each guided mode experiences a slightly different effective index of refraction n_{ef}, so Equation 3.8 can be rewritten as Equation 3.9. [69]

$$\lambda_B = 2n_{ef}\Lambda \tag{3.9}$$

After partial differentiation of Equation 3.9, the change in λ_B as a function of changes in temperature ΔT and grating section length ΔL is given by Equation 3.10. [70]

$$\frac{\Delta\lambda_B}{2} = \left[\left(\Lambda\frac{\delta n_{ef}}{\delta L} + n_{ef}\frac{\delta\Lambda}{\delta L}\right)\Delta L + \left(\Lambda\frac{\delta n_{ef}}{\delta T} + n_{ef}\frac{\delta\Lambda}{\delta T}\right)\Delta T\right] \quad (3.10)$$

Equation 3.10 is then usually reduced and linearized for λ_B, transforming into Equation 3.11, where ε is the strain component parallel to the axis of the FBG, p_e is the strain-optic tensor, α_f is the coefficient of thermal expansion and ξ_f the thermo-optic coefficient for the optical fiber. [70][71]

$$\frac{\Delta\lambda_B}{\lambda_B} = (1 - p_e)\Delta\varepsilon + (\alpha_f + \xi_f)\Delta T \quad (3.11)$$

The coefficients in Equation 3.11 can be determined experimentally or derived from the properties of the fiber material. Typical values for $(\alpha_f + \xi_f)$ and $(1 - p_e)$ are, respectively, 7.64 x 10^{-6} K^{-1} and 0.769. [71]

3.2.4 Multi-Parameter FBGs

Equation 3.11 shows that a single FBG sensor does not discriminate between temperature and strain variations. Both parameters influence $\Delta\lambda_B$ directly in a non-dissociable way.

Like regular strain gages, there are many situations where compensating for temperature is important. Continuous research on fiber grating technology and optical fiber sensors led to many solutions to this problem, both in the form of temperature independent and multi-parameter sensors.

Frazão *et al.* [72] and Kinet *et al.* [73] compiled a comprehensive list of multi-parameter optical fiber sensors based on grating technology. Many more sensor configurations can be found in specialized literature, but not all can be readily used in this work. Three promising (in the context of this work) multi-parameter configurations are discussed in the following paragraphs.

Mawatari & Nelson [74] further explore a multi-parameter configuration (Figure 3-15) that uses two superposed Bragg gratings written in a birefringent polarization maintaining fiber. Their linear system model has good longitudinal strain prediction capability (error < 10%) but poor transverse strain prediction capability (error of 10-100%). The paper also details a generalized non-linear model with greatly improved results (measurement error < 3%).

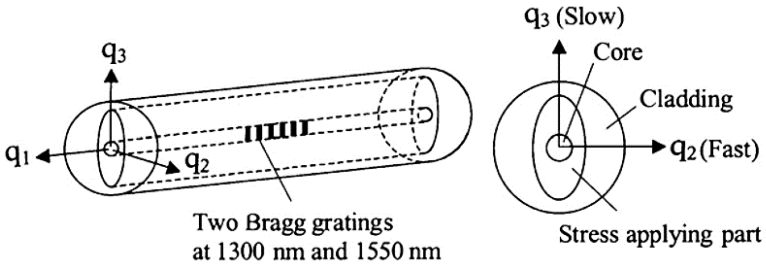

Figure 3-15 - Multi-parameter sensor configuration with dual Bragg gratings in polarization maintaining fiber. [74]

With two gratings and the birefringence, this sensor has four independent reflection peaks, as illustrated in Figure 3-16. Subscripts '2' and '3' are in relation to the axis defined in Figure 3-15, while 'a' and 'b' refers to the 1300 nm grating and 1550 nm grating respectively.

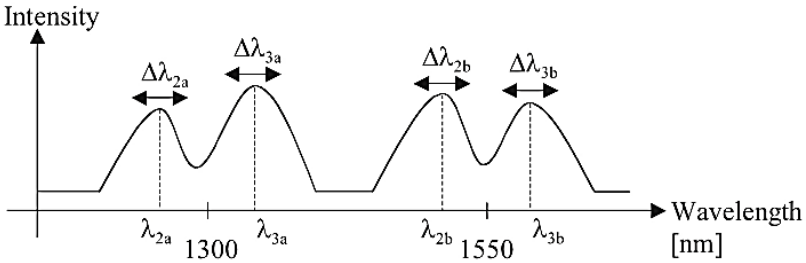

Figure 3-16 - Quadruple reflection peaks from the dual grating birefringent fiber sensor. [74]

The spectral shift of each peak can then be used in a linear system to determine temperature and strain normal to the axis q_1, q_2 and q_3, in the form of Equation 3.12, where the coefficients K_{ij} must be determined experimentally. [74]

$$\begin{bmatrix} \Delta\lambda_{2a} \\ \Delta\lambda_{3a} \\ \Delta\lambda_{2b} \\ \Delta\lambda_{3b} \end{bmatrix} = \begin{bmatrix} K_{11} & K_{12} & K_{13} & K_{14} \\ K_{21} & K_{22} & K_{23} & K_{24} \\ K_{31} & K_{32} & K_{33} & K_{34} \\ K_{41} & K_{42} & K_{43} & K_{44} \end{bmatrix} \begin{bmatrix} \varepsilon_1 \\ \varepsilon_2 \\ \varepsilon_3 \\ \Delta T \end{bmatrix} \tag{3.12}$$

Valdivielso *et al.* [75] demonstrated a strain and temperature sensor using a FBG in a fiber coated with thermochromic material in one end (Figure 3-17).

The semi-transparent thermochromic material at the fiber's tip acts as a partial mirror. Reflectivity of the interface with the fiber is a function of the thermochromic material's refractive index, which in turn is temperature dependent. By measuring the optical power shift of the back reflection at the fiber tip (Figure 3-18), it is possible to determine the temperature, with an accuracy of 0.153 ºC in the range from 20 ºC to 80 °C, and correct $\Delta\lambda_B$ for a pure strain measurement.

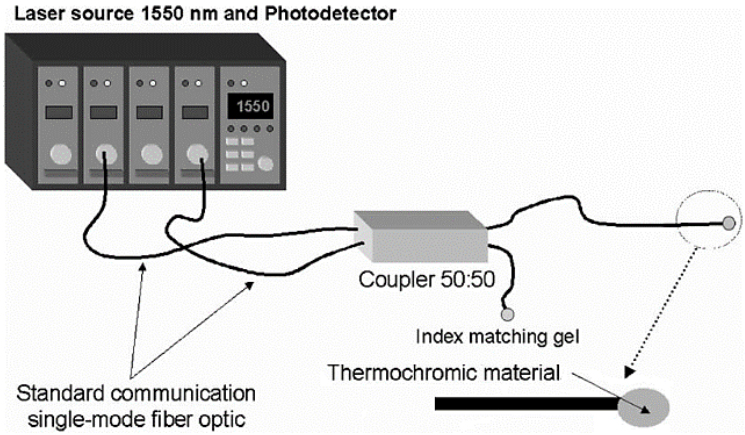

Figure 3-17 - Basic configuration for temperature and strain measurement with FBG and thermochromic material. Adapted from [75].

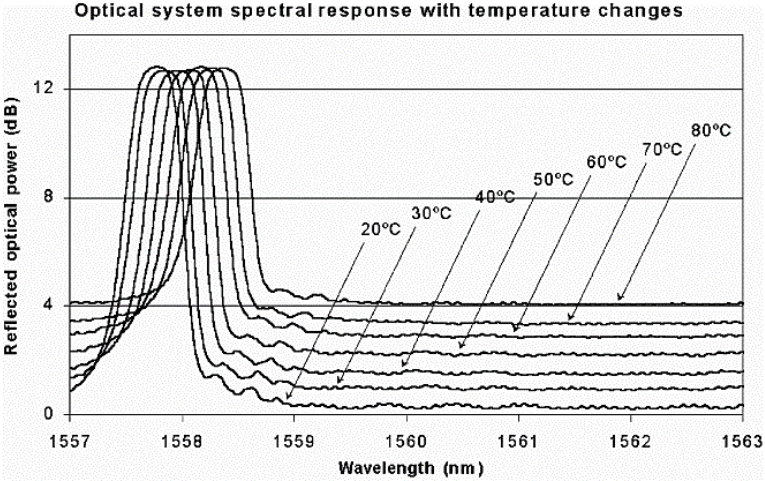

Figure 3-18 - Back reflection power and λ_B shift in response to applied temperature on the FBG-thermochromic material system. [75]

Jung *et al.* [76] used a FBG in series with an erbium-doped fiber amplifier (EDFA), as shown in Figure 3-19, to discriminate between temperature and strain. The deviations of strain and temperature were 18.2 $\mu\varepsilon$ and 0.7 °C over ranges of 0-1200 $\mu\varepsilon$ and 45-150 °C.

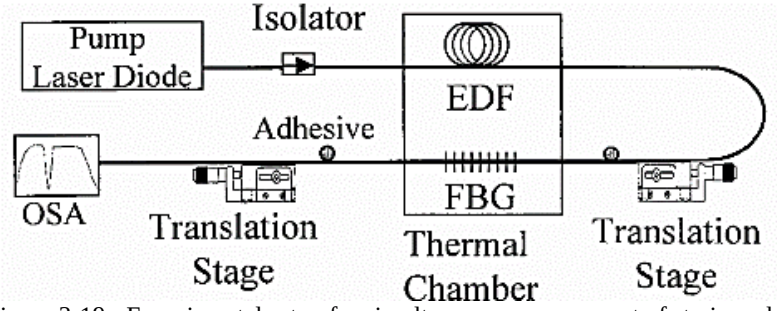

Figure 3-19 - Experimental setup for simultaneous measurement of strain and temperature with a FBG and EDFA. [76]

EDFA spontaneous emission power varies almost linearly with temperature, providing a solid base for measuring temperature to correct $\Delta\lambda_B$ [76]. This is evident when analyzing the transmitted power of the EDFA/FBG system shown in Figure 3-20. Although this is a bulky setup, the authors later reported [77] a compact setup, achieved by writing the FBG in an erbium-ytterbium-doped fiber instead of using a separated EDFA. This setup had deviations of strain and temperature of 55.8 $\mu\varepsilon$ and 3 °C over ranges of 0-1100 $\mu\varepsilon$ and 50-180 °C.

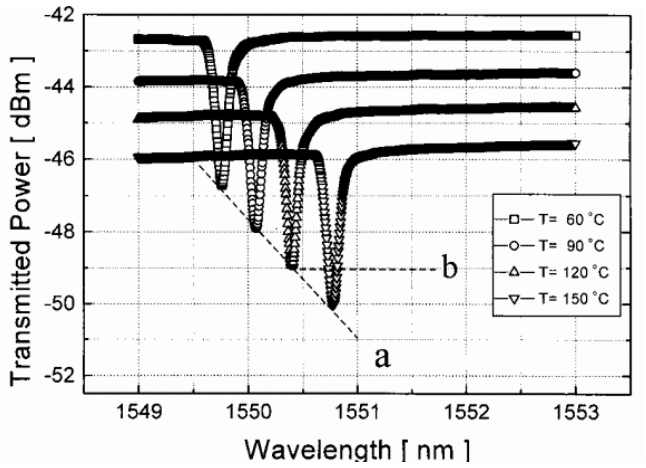

Figure 3-20 – Temperature dependence of the EDFA/FBG sensor. [76]

3.3 Fiber Fabry-Pérot Interferometer (FFPI)

3.3.1 Fundamentals

A Fabry-Pérot interferometer consist of an optical cavity delimited by a pair of partial reflecting surfaces [78], as depicted in Figure 3-21.

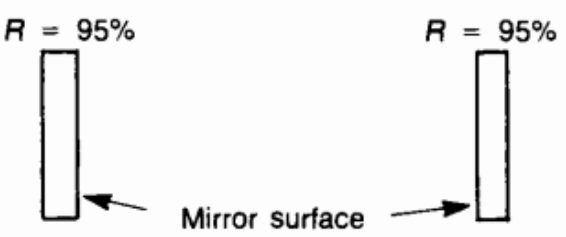

Figure 3-21 - Fabry-Perót Interferometer. [78]

What happens to light propagating across the Fabry-Perót cavity depends on the proportion between its wavelength and the cavity length. If the cavity length is an integral number of half-wavelengths (Figure 3-22) the cavity is said to be resonant and light is strongly transmitted through. Otherwise, it is non-resonant and transmission is attenuated. [78]

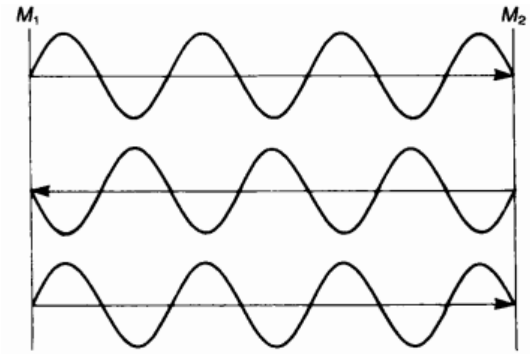

Figure 3-22 - Resonant Fabry-Pérot interferometer. [78]

The cavity length l can then uniquely define resonant wavelengths, as shows Equation 3.13, where k is a positive non-zero integer. [78]

$$\lambda = \frac{2l}{k} \tag{3.13}$$

By substituting $\lambda = v/f$ in Equation 3.13, where v is the speed of light inside the cavity, the frequency f_k of the k-th resonating wavelength is given by Equation 3.14.

$$f_k = k\frac{v}{2l} \tag{3.14}$$

And Equation 3.15 gives the value of f_k for the (k+1)th mode.

$$f_{k+1} = (k+1)\frac{v}{2l} \tag{3.15}$$

Therefore the free spectral range Δf, that is, the frequency difference between consecutive e resonating modes (i.e. transmission peaks) is also defined by l in Equation 3.16. [78]

$$\Delta f = \frac{v}{2l} \tag{3.16}$$

In the same way the cavity length defines the resonating wavelengths, the reflectance R of the partial reflecting surfaces determine how broad and well-defined transmission peaks are. A useful parameter to quantify this is the finesse F, as defined by equation 3.17. [63]

$$F = \frac{4R}{(1-R)^2} \tag{3.17}$$

Figure 3-23 shows the impact of F in the transmission spectrum of a Fabry-Pérot interferometer.

In optical fibers, FPIs can be easily made both intrinsically to the fiber with reflective splices, or extrinsically by inserting two separated pieces of fiber into an external spacer. [63]

3.3.2 Strain and Temperature Measurement

The most intuitive way of measuring with FFPIs is to exploit the relationship between transmission (or reflection) peaks and cavity length. [79]

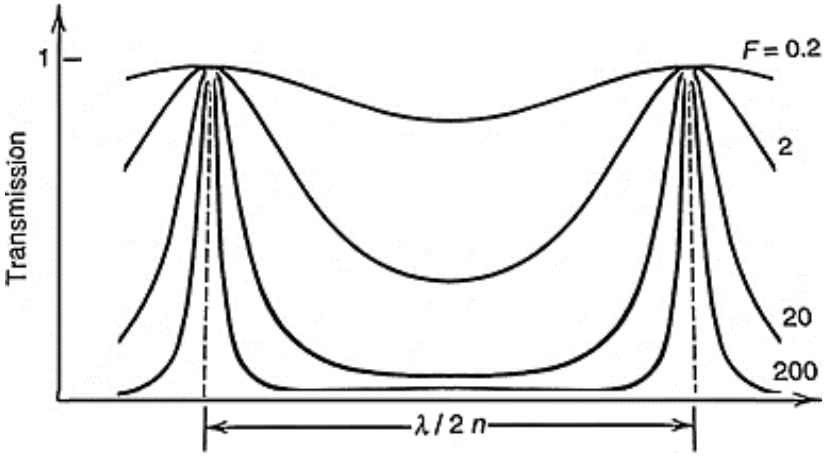

Figure 3-23 - Fabry-Pérot transmission curve for various values of finesse. [63]

Expanding the left side of Equation 3.16 yields:

$$f_1 - f_2 = \frac{v}{2l} \tag{3.18}$$

Then, using $\lambda = v/f$:

$$\frac{v}{\lambda_1} - \frac{v}{\lambda_2} = \frac{v}{2l} \tag{3.19}$$

Finally, it is easy to get to Equation 3.20 from Equation 3.19. Note that it is being assumed that the refractive index difference for the two wavelengths is negligible and thus v is the same for both.

$$l = \frac{\lambda_1 \lambda_2}{2(\lambda_2 - \lambda_1)} \tag{3.20}$$

By measuring Δl in relation to the nominal cavity length l_0, strain acting on the Fabry-Pérot cavity can be calculated with Equation 3.21.

$$\frac{\Delta l}{l_0} = \varepsilon_{tot} = \varepsilon + \alpha \Delta T \tag{3.21}$$

Where ε_{tot} is the total strain, given by the sum of the mechanical strain ε and thermal expansion $\alpha \Delta T$.

3.3.3 Hybrid FFPI-FBG

Equation 3.21 is very similar to Equation 3.11 and reveals the same strain/temperature discrimination problem.

Kang *et al.* [71] demonstrated a solution to this problem by proposing a hybrid FFPI-FBG sensor. As shown in Figure 3-24, the FFPI comes in an extrinsic configuration.

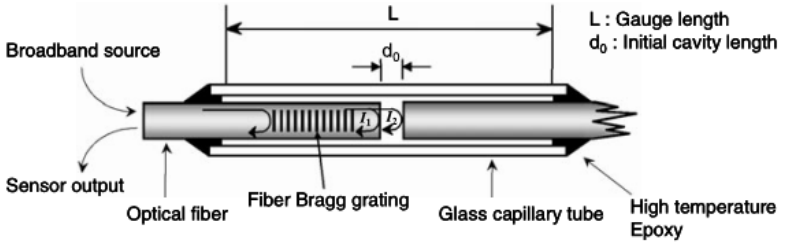

Figure 3-24 - Hybrid FFPI/FBG temperature and strain sensor. [71]

The FBG in this hybrid sensor is insensitive to mechanical strain. Temperature can be measured directly with the FBG and used to extract mechanical strain from the FFPI's response.

3.4 Reflectometry Based Distributed Sensors

3.4.1 Fundamentals

Reflectometry based sensing extracts strain and temperature information along an optical fiber by analyzing backscattered light.

Optical Time Domain Reflectometry (OTDR) techniques are based on time of flight of short light pulses to determine what position along the fiber length is being interrogated. Although capable of distributed sensing, resolution is often limited to a few meters for OTDR, making it impractical for what this work proposes. [63]

Alternatively, Optical Frequency Domain Reflectometry (OFDR) can provide distributed sensing with spatial resolution in the order of tens of micrometers. [80][81]

3.4.2 Strain and Temperature Measurement

The typical OFDR setup uses a tunable laser source and a Mach-Zehnder or similar interferometer (Figure 3-25) to measure the Rayleigh backscattering profile along the optical fiber. [80][81]

Varying the frequency of the laser source results in a periodic signal in the detector. The frequency of the generated signal is directly related to the distance to the source of the backscatter. The further down the fiber, the higher is the signal frequency. [80][81]

The detector receives backscatter information from the entire fiber at once, so the frequency components of the signal must be separated using a Fourier Transform to calculate Rayleigh backscatter as a function of position along the fiber. Extracted frequency data is then divided in small parts, usually equivalent to a few millimeters or less of fiber length, to be analyzed. [80][81]

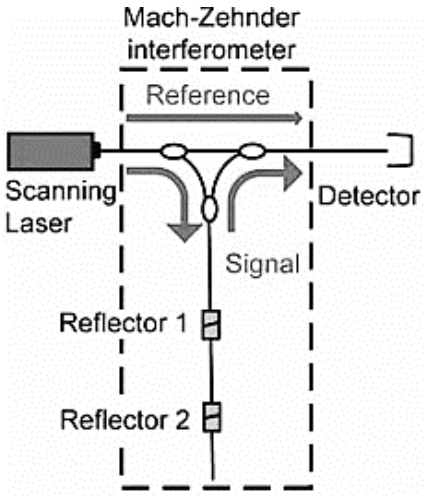

Figure 3-25 - OFDR setup with tunable laser and a Mach-Zehnder interferometer. [80]

As discussed earlier in this chapter, Rayleigh scattering is caused by small fluctuations in the refractive index of the fiber's core due to imperfections or inclusions in the glass.

When strained or subjected to a change in temperature, these fluctuations change slightly, causing a shift in the frequency spectrum, as illustrated in Figure 3-26. [80][81]

It is evident that the behavior of the backscatter profile is very similar to a FBG, showing well-defined spectral shifts. In a way this technique uses the entire fiber as a collection of small FBGs adjacent to each other. [80][81]

An application for distributed temperature measurement with OFDR [80] is shown in Figure 3-27, while Figure 3-28 shows the results of a strain measurement along the top of a beam subjected to a four point bending test [81].

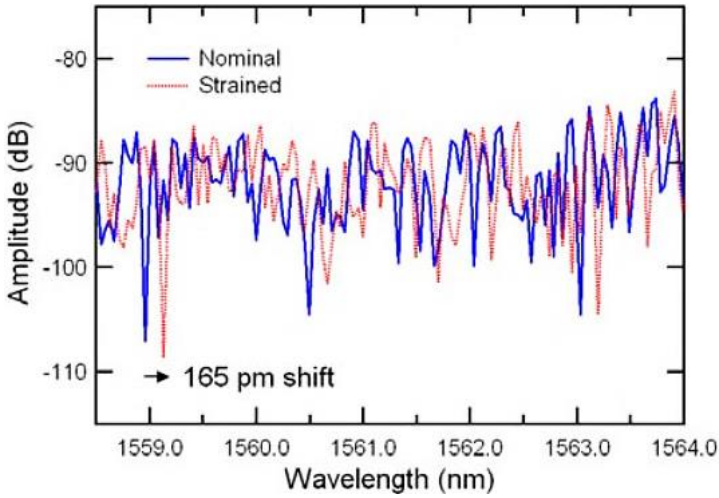

Figure 3-26 - Nominal and strained Rayleigh backscatter profile along a 5 mm fiber segment. [81]

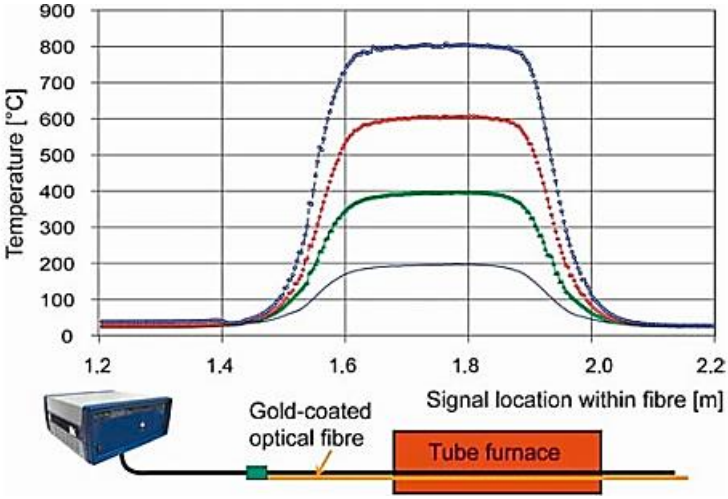

Figure 3-27 - Measure of the temperature distribution within an oven using OFDR. [80]

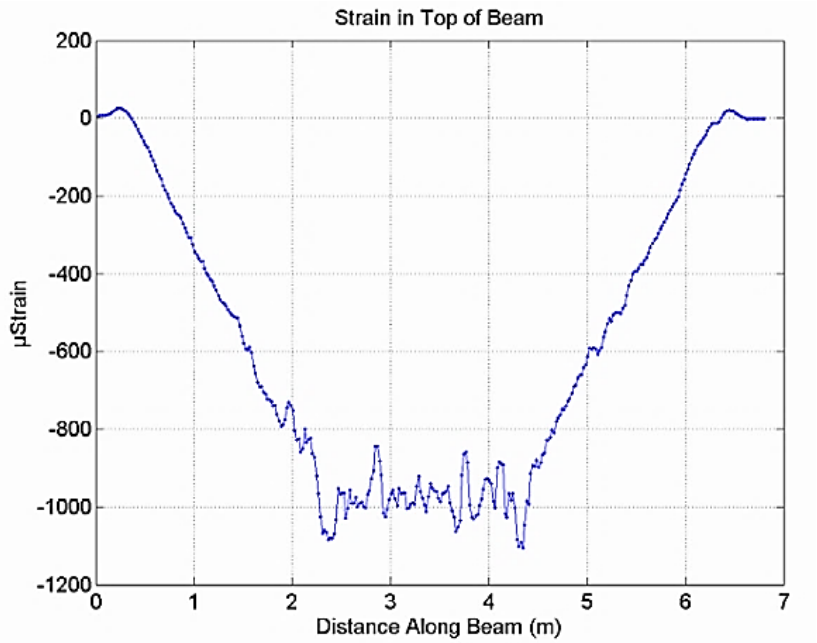

Figure 3-28 - OFDR measurement of strain along a beam subjected to a four-point bending test. [81]

4 METHODOLOGY

In section 1.4 it is disclosed that fiberglass epoxy pipes were to be used as test specimens for the experiments. The experiments and the instrumentation were designed to match them, however pipe material and geometry had to be changed.

This chapter details the original specimens design, based on the product manuals of the fiberglass-epoxy components supplier, followed by the experiments required to validate the CPVC substitute and adaptations to best utilize the fiber sensors that were acquired.

4.1 Experiments Design

To properly design meaningful experiments, from which useful data can be extracted, it is first needed to determine what stages of the pipeline lifecycle, on the perspective of the end user, are worth monitoring.

4.1.1 Pipeline Lifecycle Analysis

Some suppliers provide installation services, but all clients want assurance that the installation, either self-made or by a third-party, is flawless. This stage can be divided into two sub-stages: assembling bonded joints and assembling pipeline sections. The bonding process can introduce defects such as voids, lack of adhesive and debonding. Assembling the pipeline may introduce unwanted stress in the pipes due to poorly designed fixtures or excessive use of force to correct misalignments. Both situations can severely compromise the integrity of the pipeline and must be observed.

Overloads, water hammer, material fatigue and other mishaps during operation can result in catastrophic failure or aggravation of pre-existing defects. Premature failure can incur in high financial and environmental costs, while preventive and corrective maintenance also have associated costs. Long term monitoring during this stage can have significant impact in lowering costs and risks of running an oil and gas rig.

Quality control of pipes and fittings fabrication is of interest of the supplier, and so will not be an object of study in this work.

After determining that the stages of interest are joint fabrication, piping systems installation and operation, it is interesting to look how current quality control standards deal with this problem.

4.1.2 Preexisting Standards

Norsok M-622, ISO 14692-4 and NBR 15921-4 standards for glass reinforced plastic piping systems already specify hydrostatic testing procedure for piping spools, prefabricated adhesive bonded joints and field made adhesive bonded joints. They also detail procedures and acceptance criteria for ultrasonic and radiographic testing of bonded joints.

To keep the monitoring strategy proposed in this work as unobtrusive as possible, it has been decided to use the pre-existing hydrostatic tests as the mean to evaluate the adhesive bonding process with the integrated sensors. This also benefits the long-term sensing strategy, as loading during operation will be heavily influenced by operating pressure. Pipe systems assembly is therefore excluded from this analysis and left for a future work.

Having decided on hydrostatic pressure tests, the number of tests and a few other details must be discussed.

4.1.3 Proposed Tests

There is a better chance of successfully detecting defects internal to the adhesive bonded joint if the sensors are embedded into it. Since this is an unconventional procedure, a few sensor embedding tests must be made for validation purposes. It is expected that computed tomography of adhesive bonded joints with embedded sensors can provide enough information to validate this procedure. Instrumentation must be allocated for at least two insertion tests.

It is important to compare the data provided by the sensors embedded in a pristine joint and one with purposefully inserted defects, to verify how they respond to the presence of defects. This can be thought as defect detectability test. There is an ongoing research at Labmetro for the development of a digital shearography system to inspect composites and the latest shearography system will also be used during this test to compare defect detectability.

Section 2.7 presents a discussion on how the presence of embedded sensors can affect mechanical properties of composites and adhesive bonded joints. By gradually increasing internal pressure until failure occurs and comparing maximum achievable pressure of joints, with and without embedded sensors, the impact of the fibers in the pressure rating can be evaluated. At least three tests for each condition are required for statistical significance.

4.1.4 Summarizing Design Decisions

For a clearer understanding of what has been discussed in this section, all experiments design decisions are summarized below:

- Monitoring pipeline assembly process has been left out in favor of joint fabrication and long-term operation monitoring.

- Defect detectability tests and impact on pressure rating tests will be executed with hydrostatic loading to better harmonize with pre-existing quality control standards;

- Two sensor embedment tests are to be performed to validate insertion strategy. CT scans will provide the needed data;

- Detectability tests will consist of comparing strain information from a pristine joint to another with planned defects. Digital shearography will be used for comparison purposes and CT will provide additional information;

- Six adhesive bonded joints, half with embedded sensors and the other half without sensors, will be pressurized until failure to determine the impact, if any, of the embedded sensors in the joint's pressure rating;

4.2 Test Specimen Design

Fiberglass-epoxy pipes with 150 mm (6") nominal diameter and adhesive bonded bell and spigot joints, such as the one in Figure 4-1, have been well studied before in Labmetro for the digital shearography research programs.

In this configuration the spigot's extremity is shaved to create a 1.5 to 2.0 mm radial clearance in relation to the bell, which leaves plenty of space for the optical fiber sensors to be inserted into the adhesive layer.

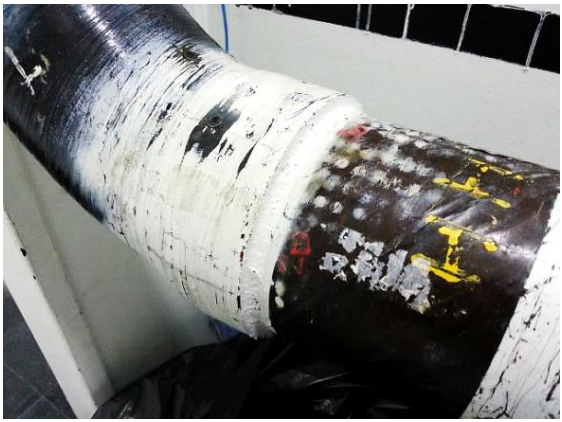

Figure 4-1 - Fiberglass-epoxy pipe with adhesive bonded bell and spigot joint.

This particular pipe and fittings product line is bonded using a bi-component epoxy-based adhesive.

Steel blind flanges, with a central threaded hole for hydraulic connections (Figure 4-2), are available from previous projects to be used with new test specimens for hydrostatic testing.

Figure 4-2 - Steel blind flange fixed to the flanged end of a fiberglass-epoxy pipe.

The simplest specimen design is a straight pipe section, with a single bell and spigot joint in the center, flanged ends and with total length that can fit into the available industrial CT machine. This design is illustrated in Figure 4-3.

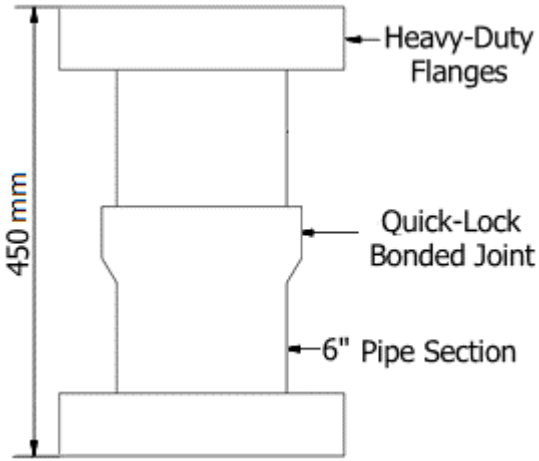

Figure 4-3 - Straight 150 mm (6") pipe with a single bell and spigot joint.

Considering two test specimens for sensor embedding tests, two for the comparison between pristine and defective joints, and two sets of three specimens for destructive testing, the total amount of test specimens is ten.

After designing the specimen and determining how many are needed, the company that provided some specimens for previous projects, including the one depicted in Figure 4-2, was contacted and agreed to provide the specimens for academic research purposes in exchange for full test result disclosure.

4.3 Instrumentation Design

This study is starting a new line of research in the Federal University of Santa Catarina where the main objective is to evaluate the feasibility of using embedded optical fiber sensors for SHM of adhesive bonded joints in pipelines. A good approach is to start with a simple single parameter FBG, evaluate its strong points and shortcomings, and propose a better sensing element for future works.

The reasoning behind the embedded instrumentation is that the presence of defects disrupts the strain distribution in the bonded joint. By measuring strain in various locations, compounding them into an approximation of the strain field and looking for spots with abnormal strain changes, it is possible to detect the presence of defects such as debonding or lack of adhesive

From this perspective, instrumentation was designed accordingly to the geometrical characteristics of the test specimens to provide good strain measuring coverage without employing an excessive number of optical fibers that could compromise the joint's mechanical properties

Relevant geometrical characteristics are insertion depth, which is the length of the spigot that is inserted into the bell, and spigot diameter, which defines its circumference. Geometry discontinuities in both extremities of the inserted section leads to regions with stress concentration. Figure 4-4 contains a cross-section representation of the spigot with those characteristics pointed out.

Insertion length can be used to determine the length of a sensing fiber with FBGs embedded axially into the adhesive layer of the joint, while the circumference provides the circumferential separation between fibers for different number of fibers per joint. Accordingly to the supplier's product manual, for a pipe with 6" nominal diameter, insertion depth is 57 mm and mean spigot diameter 166.4 mm. A mean diameter of 166.4 mm is equivalent to a mean circumference of 522.76 mm.

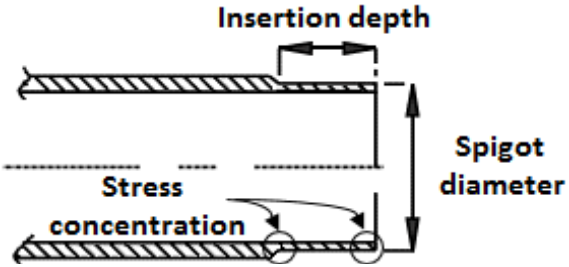

Figure 4-4 - Spigot cross-section indicating insertion depth, spigot diameter and stress concentration areas.

The circumferential separation between two consecutive fibers is the length of the arc between them, as shown in Figure 4-5. Table 4-1

Table 4-1 contains the circumferential separations values and number of fibers in a full circle for some separation angles. There is a compromise between circumferential separation and number of fibers per bonded joint. Smaller separation between fibers results in better strain sensing coverage, but more fibers raises costs and can have deleterious effects on joint pressure rating. Taking these factors into account the value of twelve fibers per joint is a good middle ground.

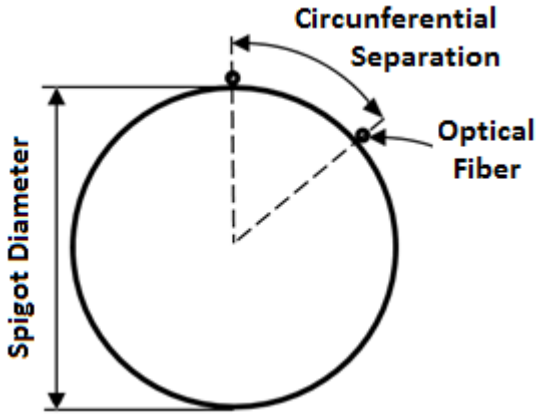

Figure 4-5 - Schematic representation of circumferential separation between optical fibers.

Table 4-1 – Circumferential separation and number of fibers in a bonded joint based on fiber separation angle.

Separation Angle (degrees)	Circumferential Separation (mm)	Number of Fibers
45	65.35	8
30	43.56	12
18	26.14	20
15	21.78	24

Higher stress in the stress concentration regions makes monitoring them especially important. One FBG must be placed near these points, but not too close to the borders or it can be damaged during the assembly process.

Utilizing only one FBG at each stress concentration points would leave a relatively big sensing void in the middle of the inserted section, considering the typical grating length of about 5 mm. Taking into account the number of fibers per bonded joint and the total of seven instrumented joints, the total number of sensors increases very fast for each FBG included between the other two. So, considering that the available financial resources must cover all sensors, a single FBG was added between the others.

The resulting three FBG array (Figure 4-6) is also provided with a 0.9 mm loose tube and a FC/APC connector. This tube is intended to protect the unembedded section and prevent the fiber from breaking at the point it leaves the adhesive.

The chosen buffer coating material is polyimide, as it is easily available on the market, can withstand the adhesive cure temperature of about 100 ºC and is chemically compatible with epoxy adhesives. [82]

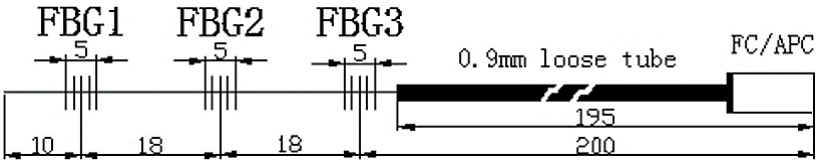

Figure 4-6 - Three FBG array with loose tube and FC/APC connector.

In order to avoid confusion when embedding and interrogating a set of twelve fibers, each fiber in a set has three FBGs with unique nominal Bragg wavelength combinations. These combinations are made from six possible values, which is the smallest pool size that allows for at least twelve unique combinations: 1530 nm, 1535 nm, 1540 nm, 1545 nm, 1550 nm and 1555 nm. The twelve combinations in each set are listed in Table 4-2.

Table 4-2 - Nominal Bragg wavelength combinations per set of twelve fibers.

Combination	λ_B **FBG 1 (nm)**	λ_B **FBG 2 (nm)**	λ_B **FBG 3 (nm)**
1	1530	1535	1540
2	1535	1540	1545
3	1540	1545	1550
4	1545	1550	1555
5	1530	1540	1550
6	1535	1545	1555
7	1530	1540	1545
8	1535	1545	1550
9	1540	1550	1555
10	1530	1535	1545
11	1535	1540	1550
12	1540	1545	1555

It is also interesting to investigate if FBGs integrated to the outer side of the bell and spigot joint can also detect the presence of defects.

A sub-surface defect can produce detectable disturbances in the strain field at the outer surface; this effect is exploited with optical interferometric techniques such as holography and shearography, as shown in Chapter 2.

For this purpose, a longer chain of FBGs has been designed to be wrapped around the circumference of the bell's outer surface. The bell's external circumference was measured from Figure 4-1 pipe using a measuring tape to be approximately 600 mm. To match the number and position of the axial fibers, this longer fiber was given twelve FBGs equally spaced by 50 mm.

The longer fiber is also polyimide coated and has a FC/APC connector. Its nominal Bragg wavelengths are distributed between 1530 nm and 1557.5 nm, with uniform 2.5 nm difference between adjacent sensors.

4.4 CPVC Test Specimen

Unfortunately, just after the designed instrumentation was bought and delivered, the company that originally agreed to supply the test specimens contacted Labmetro dismissing the deal. As resources for acquiring new test specimens were scarce, the first alternative was to look for readily available low cost PVC or other similar material pipes that usually have bonded joints.

The main concern was finding products with similar dimensions to the fiberglass-epoxy pipes, so that the sensors could still be used without complicated adaptations.

A promising industrial CPVC piping systems line of products was then prospected. Insertion depth was 57.5 mm for 4" nominal diameter pipes and fittings, practically the same depth the embedded instrumentation was designed for. All available 6" CPVC piping implements had insertion depths far longer than 57 mm.

The use of a smaller diameter is an interesting change, since smaller diameters lead to smaller circumferential separation between fibers, making for a better sensing coverage. However, the longer FBG chains, designed to be wrapped around the 6" joint, no longer has sensors matching the position of embedded fibers.

The last problem that needed to be addressed was the particularities of the adhesive bonding process between PVC and CPVC pipes.

PVC and CPVC adhesives are solvents, the mating surfaces must be dissolved into a semi-fluid and inserted with interference while they are still wet. This results in a joint whose surfaces are partially bonded and partially fused together [83], as shown in Figure 4-7.

This bonding process does not provide enough space for embedding sensors and does not produce joints that behave similarly as the ones in the fiberglass-epoxy systems.

A workaround is to machine the spigot's outer surface to create a 1 to 2 mm radial clearance and use a compatible bi-component plastic adhesive to bond the spigot to the bell, simulating the adhesive bonded joints described in section 0.

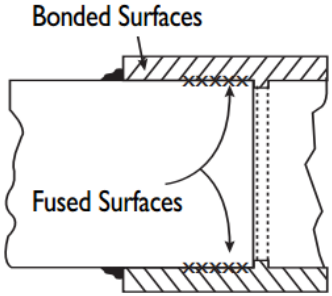

Figure 4-7 - Solvent bonded PVC pipe and fitting with bonded and fused surfaces. [83]

A suitable, heavy-duty industrial methyl methacrylate based bi-component adhesive, capable of bonding PVC substrates with up to 4 mm gap filling was found. Chemical compatibility and bonding efficiency with the fibers polyimide coating was unknown and needed to be properly tested. As the chemical composition of CPVC is different from regular PVC, testing if the adhesive can provide a strong adhesive bond in CPVC is also required.

4.4.1 Preliminary Tests

A simple test was devised in order to test the compatibility between the adhesive, the CPVC pipes and the polyimide coating. For the experiment, a straight piece of 22 mm nominal diameter CPVC pipe, typically used for residential hot water installations, was acquired. Additionally, a matching cap, a threaded adaptor, a sleeve and a bottle of solvent adhesive were also acquired.

The 22 mm CPVC pipe was cut in half. The solvent adhesive was used to bond the threaded adaptor and the sleeve to one of the halves (Figure 4-8). The other half had a sealing cap bonded into one end, while the other end was machined to create a 1 mm radial gap when inserted into the sleeve.

A sample of the methyl methacrylate adhesive, kindly provided by its manufacturer, was then used to bond the machined piece to the vacant side of the sleeve. The sample was also used to glue a single three FBG chain to the surface of the pipe, as shown in Figure 4-9.

Figure 4-8 - Hot water installation CPVC pipe with one machined end (indicated by the yellow arrow) and solvent bonded fittings.

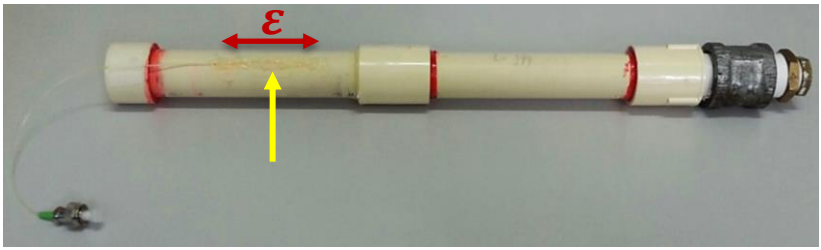

Figure 4-9 - Left side of the sleeve and a single three FBG fiber (indicated by the yellow arrow) bonded to the pipe using the methyl methacrylate adhesive. The direction of strain sensitivity of the FBG indicated by the red arrow.

The FBG chain was aligned along the fiber axis in order to measure the axial strain in response to pressure loadings, as originally intended for the embedded fibers. This particular fiber was selected for being the only one containing one poorly written FBG (Figure 4-10).

A testing bench was assembled using spare aluminum profiles, steel plates, a vacuum chamber window and transparent acrylic sheets (Figure 4-11). The CPVC test specimen was fitted with a manometer and connected to a manual hydraulic pump, while the FBG chain was connected to a FBG interrogator using a 5 meters reinforced patch cord.

Three hydrostatic pressure tests were executed. The first one up to 10 kgf/cm² (0.98 MPa) of internal manometric pressure to see if the methyl methacrylate bond would hold. The results of this first test are summarized in Figure 4-12.

The second test (Figure 4-13) had the test specimen pressurized up to 20 kgf/cm² (1.96 MPa), close to its pressure rating of 2.20 MPa at room temperature. At this point the bonded joint did not exhibit any signs of imminent failure and the FBG signal had not started to degrade.

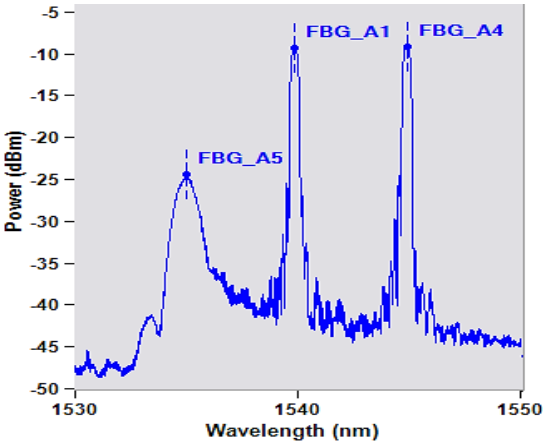

Figure 4-10 - Reflection spectrum of the FBG chain chosen for the adhesive test. A poorly written FBG produces the weaker reflection peak to the left.

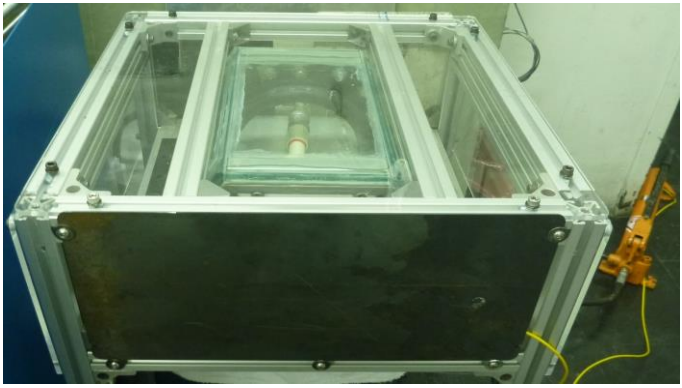

Figure 4-11 - Assembled test bench. The test specimen can be seen resting inside and the manual hydraulic pump in the right side of the picture.

To fully test the capabilities of the adhesive a third test (Figure 4-14) was started, with the intent of keep rising internal pressure until the test specimen fails. The test was interrupted when internal pressure reached 80 kgf/cm² (7.85 MPa), still before failure occur, due to safety concerns. No FBG signal degradation was observed.

Bragg wavelength shift was very linear in every test, with no observable hysteresis. The bonded joint's performance was far superior from the expected. CPVC pipes and the methyl methacrylate adhesive were then considerate adequate substitutes to the fiberglass-epoxy pipes.

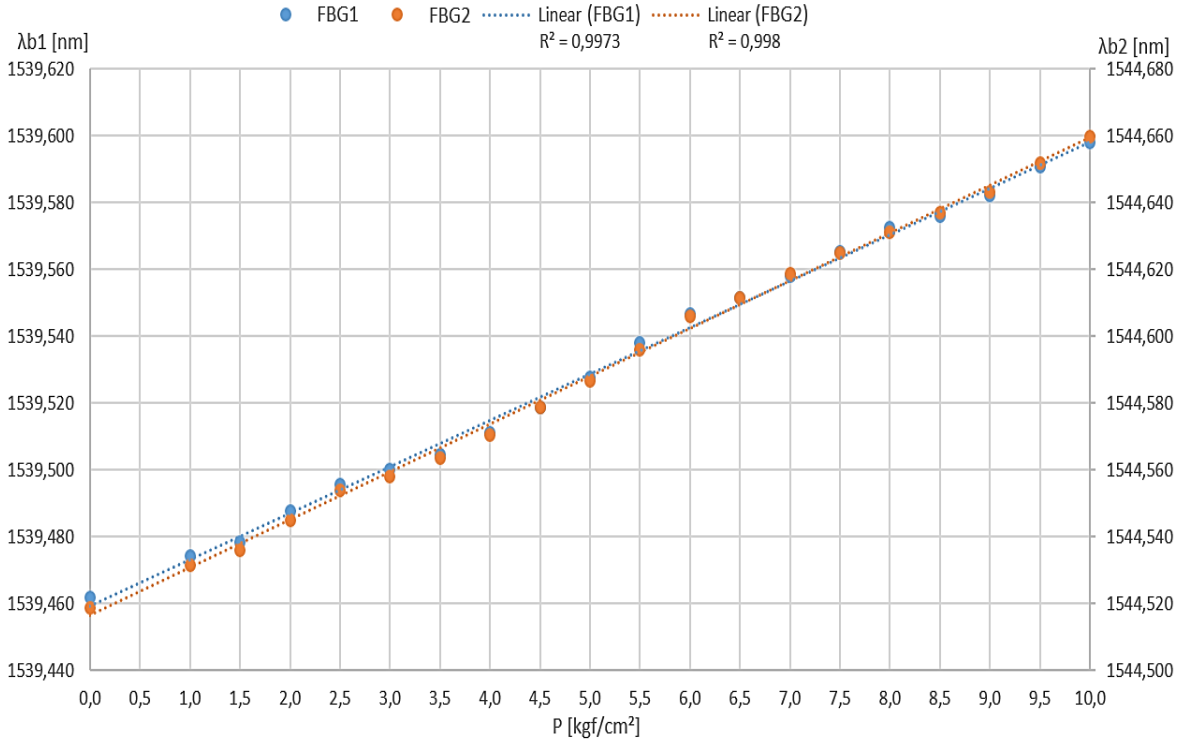

Figure 4-12 – Response of the FBGs up to 10 kgf/cm² internal pressure load. Big dots represent collect data and dotted lines are best fitted to them.

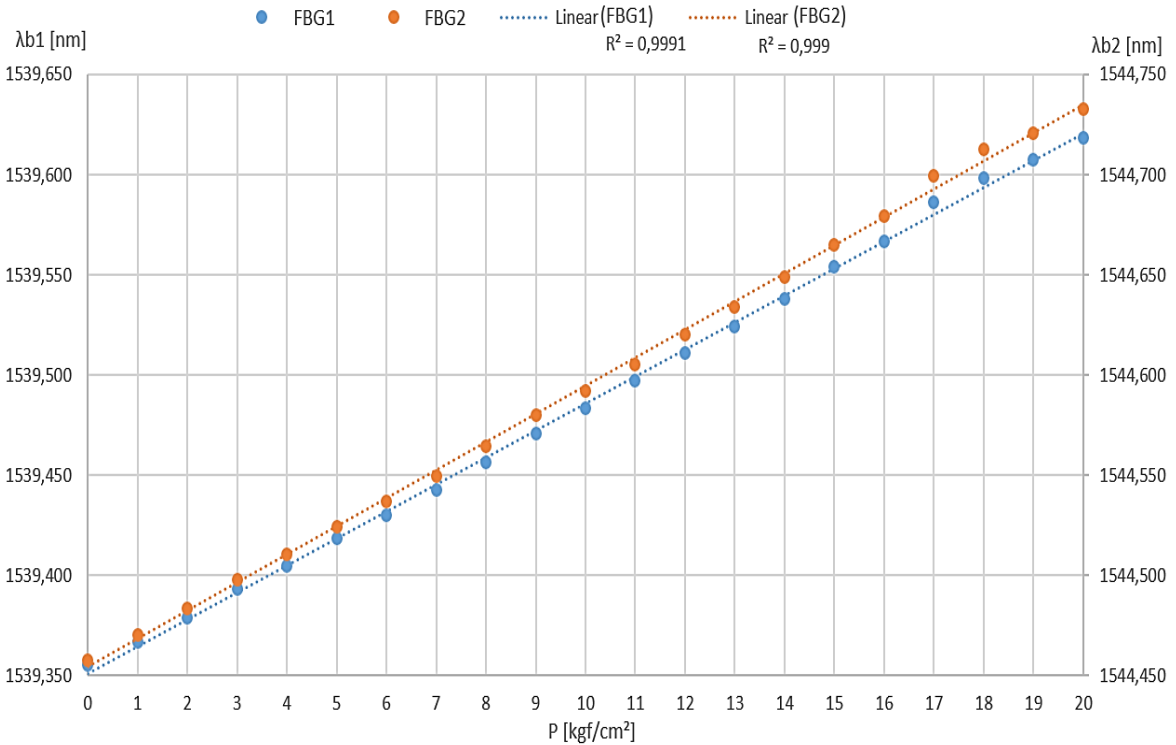

Figure 4-13 – Response of the FBGs up to 20 kgf/cm² internal pressure load. Big dots represent collect data and dotted lines are best fitted to them.

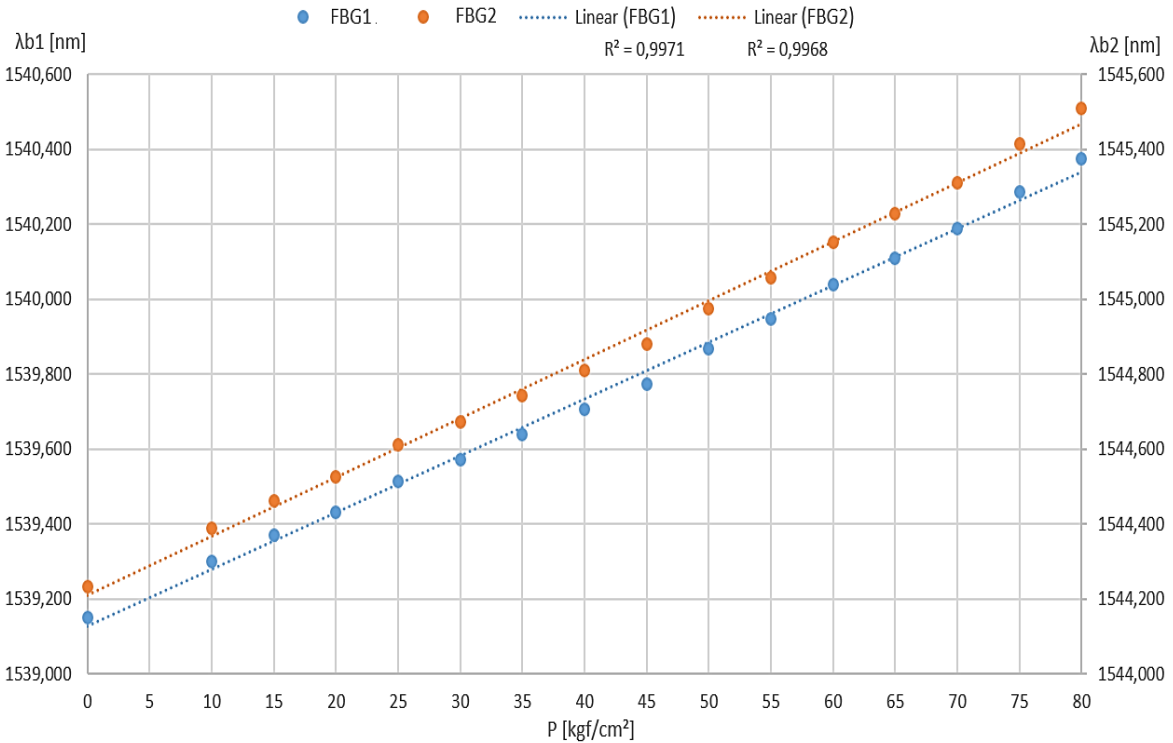

Figure 4-14 - Response of the FBGs up to 80 kgf/cm² internal pressure load. Big dots represent collect data and dotted lines are best fitted to them.

4.4.2 Test Specimen Design and Adaptations to Planned Tests

The industrial 4” CPVC test specimen (Figure 4-15) is basically a bigger version of the one shown in Figure 4-8, with the exception of substituting the threaded end for a flange.

Figure 4-15 - 3D model of the proposed CPVC test specimen.

Sensors were embedded in the side of the sleeve facing the cap. All straight pipe pieces inserted into this side of the sleeve must be machined. Radial gap has been defined as 1.5 mm for all methyl methacrylate bonded joints.

The indicated 450 mm total length from the bottom of the cap to the leftmost face of the sleeve is a design reference to ensure this section of the test specimen fits into the CT machine. To this end, the length of the pipe piece to be solvent bonded to the cap and adhesive bonded to the sleeve was set to 280 mm.

There is no length restriction for the pipe segment solvent bonded to the flange, since this part would not be tested with CT. Considering the insertion depth of 57.5 mm into the sleeve, the length of this segment was set to 200 mm, keeping the specimen compact with a total length just short of 600 mm.

The number of test specimens can be reduced to seven, down from ten at Section 4.2, by cleverly using both sides of the sleeve in the destructive tests. Instead of doing six separate destructive tests, three

with embedded sensors and three without, it is possible to have three test specimens where both sides of the sleeve are adhesive bonded.

If sensors are embedded in just one side of the sleeve, and if a tendency for failure to occur in this side is observed, it will be considered a strong indication that the presence of the fibers is deleterious to the bonded joint.

The number of embedded fibers remains the same. The reduced diameter translates into a circumferential separation reduction from 43.56 mm to approximately 30 mm.

5 RESULTS AND DISCUSSION

Before performing tests with bonded joints all acquired sensors and patch cords (Figure 5-1) were tested to make sure no faulty sensor would be used in the experiments. Only a single 3 FBG array had a faulty sensor. It was separated from the others and then used for the preliminary CPVC pipe test described in the previous chapter.

Figure 5-1 - 3 FBG arrays, 12 FBG arrays and patch cords.

The setup used to interrogate and test the sensors was basically the same for all the experiments detailed in this chapter. The fibers were connected to a 1x12 bi-directional MEMS switch (Figure 5-2), which was then connected to a 4-channel FBG interrogator (Figure 5-3) using a patch cord.

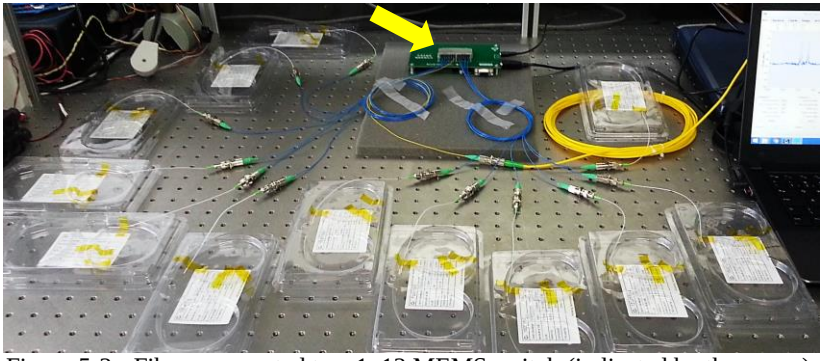

Figure 5-2 - Fibers connected to a 1x12 MEMS switch (indicated by the arrow).

Figure 5-3 - Optical sensing interrogator.

The switch is controlled by a laptop computer through a USB port, while the interrogator communicates to the computer using an Ethernet port.

Total fiber length is less than 8 meters, with the 5 meters patch cords, 1 meter in/out switch ports plus sensing fiber length. The optical signal travels approximately double this value since the FBGs reflection spectrum is the one being analyzed. This is relatively very short and signal attenuation is not a concern considering attenuation values presented in Section 3.1.3.

The specimens were prepared by first cutting the straight pipe pieces to the specified length. They were also machined to ensure a square cut and to provide the radial clearance when necessary (Figure 5-4).

Figure 5-4 - Cut and machined pipe pieces.

Next the caps and flanges were solvent bonded to the pipe pieces. The caps to the longer pieces and the flanges to the shorter ones (Figure 5-5).

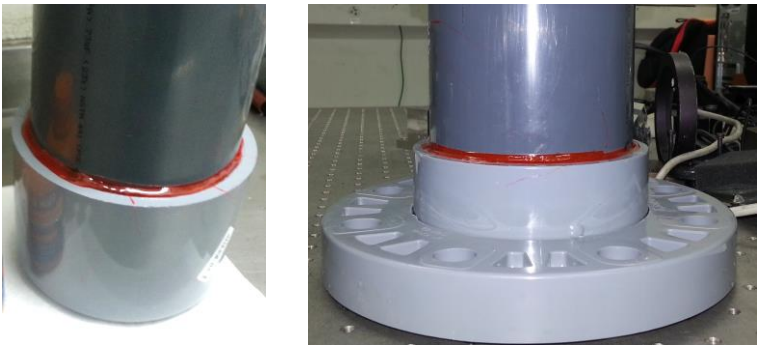

Figure 5-5 - Solvent bonded cap (left) and flange (right).

The assembly process was finished by bonding these two parts to a single sleeve. This is accomplished by first adhesive bonding the capped piece, along with the embedded sensors, to a sleeve and then either adhesive or solvent bonding the flanged piece to the opposite side of the sleeve.

A total of three test specimens were fully assembled. Further details on three, instead of seven as originally planned, will be provided in the following sections when appropriate.

5.1 Optical Fibers Embedding Analysis

Analysis for the three test specimens, dubbed Specimen A, Specimen B and Specimen C, are presented in order.

For Specimen A, the embedding procedure is extensively detailed. Adjustments made to the original procedure are discussed in the section corresponding to the test specimen they were implemented.

After detailing and discussing the embedding process, results from the CT scans and embedded sensors are presented, compared and discussed.

5.1.1 Specimen A

Firstly, the 3 FBG arrays were pre-positioned around the pipe using adhesive tape, as shown in Figure 5-6. The loose tube enters slightly the area to be bonded, preventing the fiber from breaking in the point it exits the cured adhesive.

Figure 5-6 - FBG arrays pre-positioned on the pipe.

Note that since this is the first attempt at embedding the sensors, this test specimen is using the remainder 11 fibers from the set that has one fiber with a defective FBG. The other two specimens have a full set of 12 fibers embedded into them.

Next the tip of the fibers was glued to the pipe with a cyanoacrylate instant adhesive (Figure 5-7). This prevents the fiber from bending when the pipe is inserted into the sleeve, which could misalign or break the fibers.

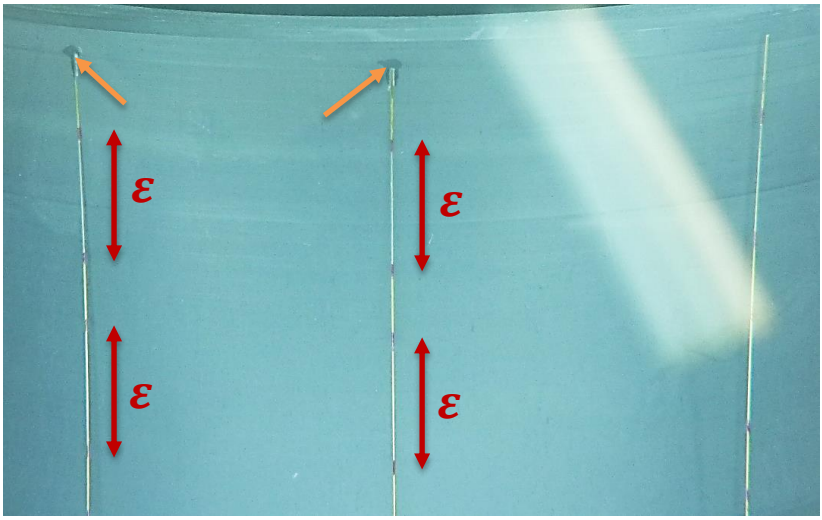

Figure 5-7 - Tip of the fibers glued to the pipe (orange arrows) and the direction of strain sensitivity of the FBGs (red arrows).

The methyl methacrylate adhesive is first applied along the length of the fiber (Figure 5-8). It is made in order to further fix them in place and to avoid moving them during the procedure to spread the adhesive around the tube.

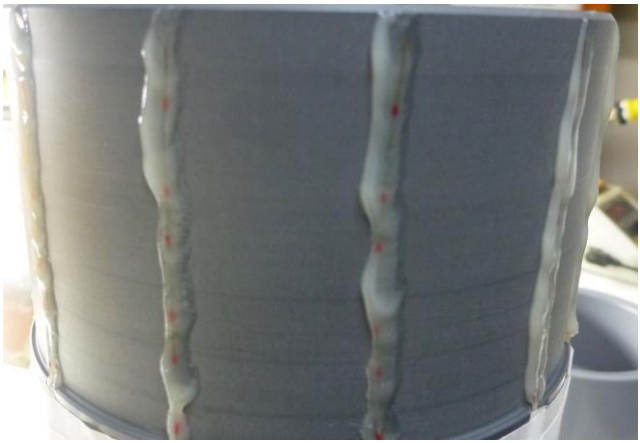

Figure 5-8 - Adhesive applied directly along the fibers.

Adhesive is then applied and spread along the rest of the spigot until a thick layer of adhesive covers the whole section that will be inserted in the sleeve, as shown in Figure 5-9.

Figure 5-9 - Thick layer of methyl methacrylate adhesive covering the spigot.

The sleeve is also coated with a layer of methyl methacrylate adhesive.

Figure 5-10 - Methyl methacrylate adhesive layer in the sleeve.

The adhesive, in the form of bi-component cartridges, was applied with the help of a manual adhesive gun and a plastic mixer nozzle (Figure 5-12).

Figure 5-11- Adhesive gun with a loaded cartridge. Mixer nozzle detached from the cartridge, to the right.

Finally, the spigot and the sleeve are carefully mated and the adhesive is allowed to cure for 24 hours. This partial assembly (Figure 5-12) is then evaluated by means of the FBG sensors and CT scanned before bonding the remaining part.

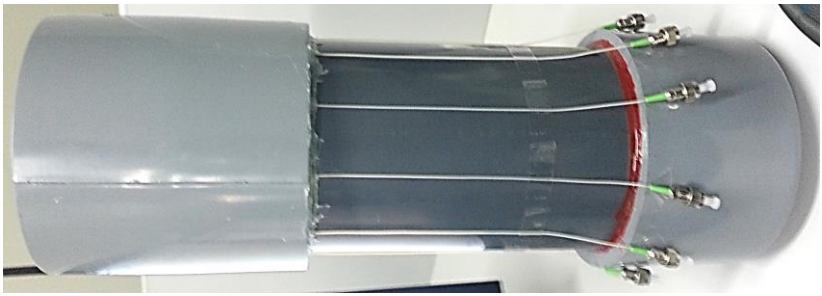

Figure 5-12- Partial test specimen assembly with embedded sensors.

The quality of the bonded joint can then be accessed for the first time by measuring the shift of λ_B for all FBGs and using Equation 3.11. λ_B was measured for all sensors after pre-positioning them and then measured again after the 24 hours curing period.

Room temperature was the same for both tests, so Equation 3.11 can be simplified as follows.

$$\frac{\Delta\lambda_B}{\lambda_B} = (1 - p_e)\Delta\varepsilon \tag{5.1}$$

Isolating ε and using $(1 - p_e) = 0.769$ (refer to Section 3.2.3):

$$\Delta\varepsilon = \frac{10^6}{0.769}\frac{\Delta\lambda_B}{\lambda_B} \quad [\mu m/m] \tag{5.2}$$

The strain is expected to be compressive (negative), due to adhesive shrinkage during the curing process. [84]

Figure 5-13 is a 3D plot of the cure strain distribution inside the adhesive layer, as measured by the FBGs. The Z axis is strain in $\mu m/m$. X axis (0 through 11) are the fibers. Fibers 0 and 11 were purposely plotted with the same data to visualize the strain for the full circumference. The Y axis represent the three FBGs, being 0 the innermost FBG and 2 the FBG nearest to the outer edge of the sleeve. Interpolation between strain values is bilinear.

Figure 5-14 is a 2D color plot of the same strain distribution. The color bar indicates the strain, in $\mu m/m$, and the X and Y axis are the same as in the 3D plot. Every plot from now on will use the same units, axis convention and interpolation as these two.

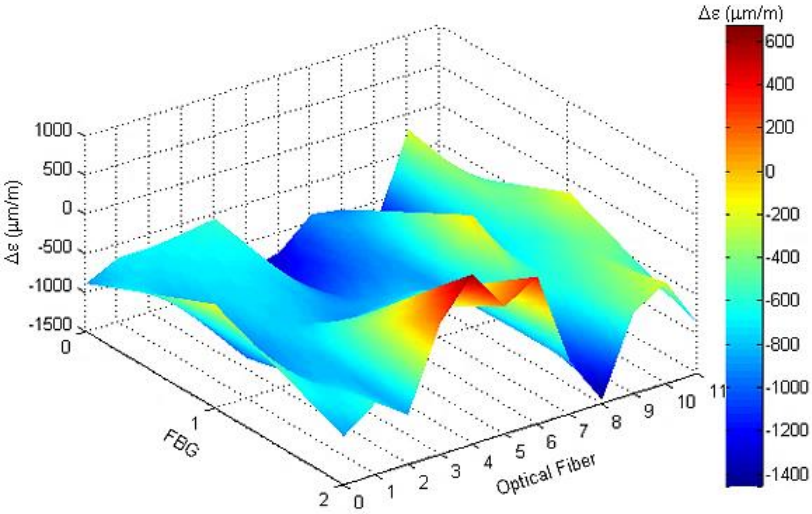

Figure 5-13 - 3D plot with color bar of the cure strain distribution in the adhesive layer. Test specimen A.

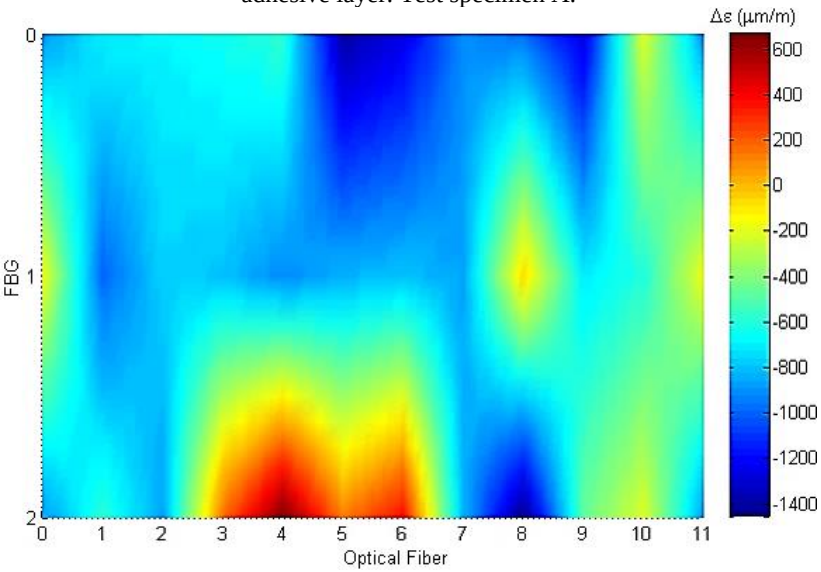

Figure 5-14- Color plot of the cure strain distribution in the adhesive layer. Test specimen A.

Strain distribution is evidently very disarranged. For the same value of Y, strain distribution along X was expected to be approximately uniform due to rotational symmetry but this is not observed.

There is also a pack of FBGs in fibers 2 to 7 with tractive loading, contradicting the predicted compressive strain due to adhesive shrinkage during the cure.

This is an indication that either the sensors are poorly bonded to the adhesive, which is unlikely considering this was not observed in the smaller CPVC pipe, or that many defects were unwillingly introduced into the bonded joint.

The results from the CT scan corroborate the last hypothesis. Figure 5-15 is a 3D rendition of the scans from the bonded joint. Transparency was turned on in the renderer to visualize the internal structure of the bonded joint. Darker areas are voids in the adhesive layer, meaning that a large percentage of this bonded joint is lacking adhesive.

Figure 5-15 - 3D rendering of the CT images. Transparency is used to observe the internal structure of the joint. Darker areas are voids in the adhesive layer.

Cross-sectional cuts of the bonded region also clearly show the lack of adhesive. In Figure 5-16 the voids are contoured in white.

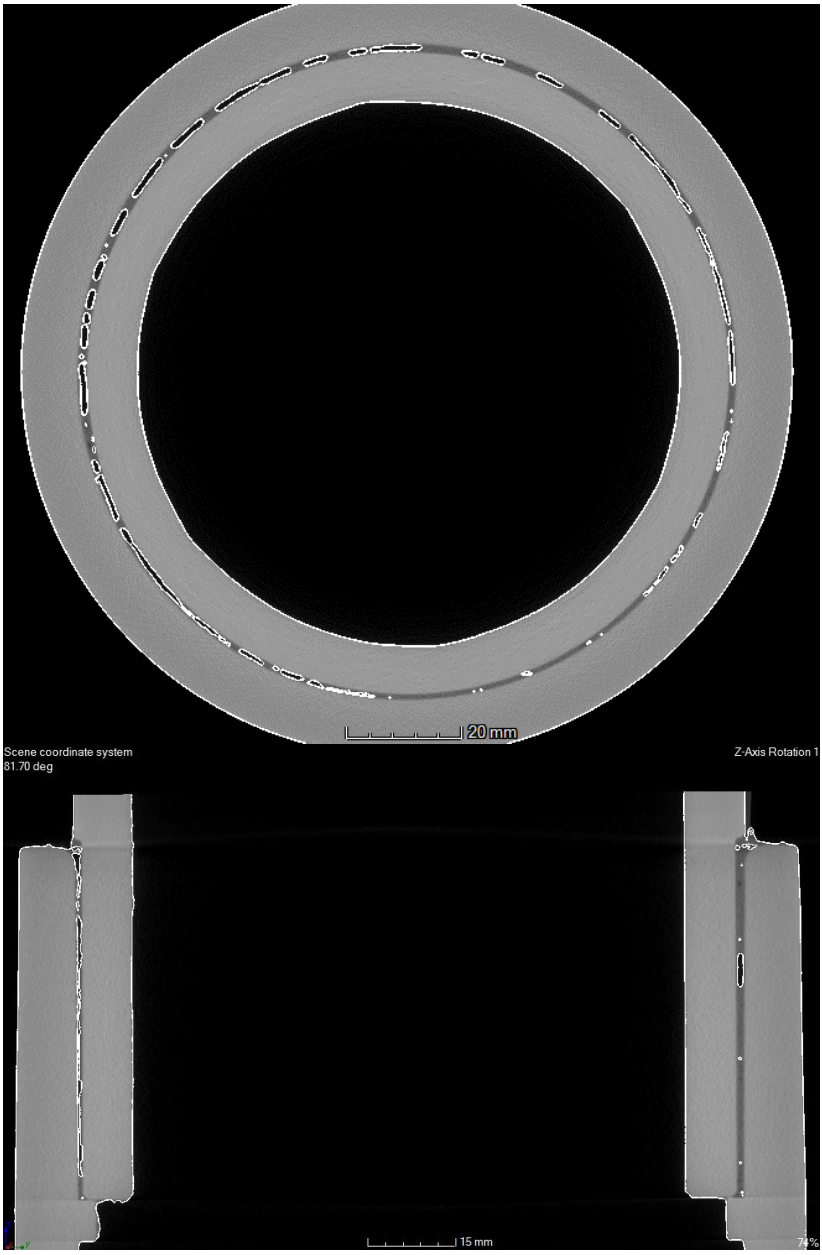

Figure 5-16 - Cross-sectional cuts of the adhesive bonded joint. Voids are contoured in white.

Unfortunately, no optical fiber is seen in any of the last images. A zoomed in view of the cross-section (Figure 5-17) reveals that the fibers are too small to produce a discernible CT signal once inside the bonded region.

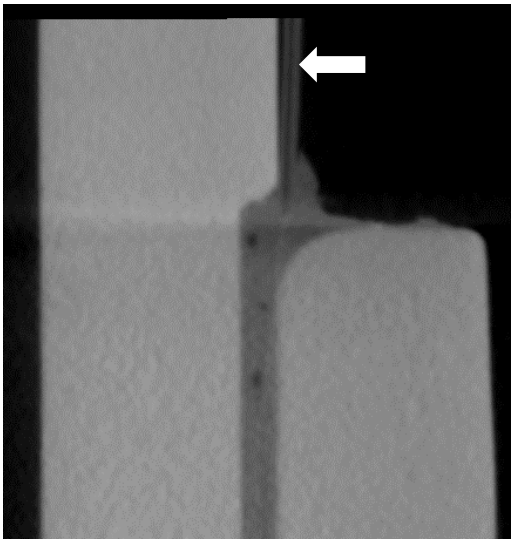

Figure 5-17 - Detail of the cross-section shows an optical fiber (indicated by the arrow) entering the adhesive bond and vanishing soon after.

It is unfortunate that the CT images cannot be used to observe the position of the fibers in detail. Nonetheless the images still contain a lot of information that can be compared to the strain maps.

5.1.2 Specimen B

Two changes were made to the fibers embedding process to try to produce a good quality bonded joint.

The first was a great increase in the amount of adhesive used. Each cartridge contains 50 ml of adhesive. In the first joint about 30 ml were used and for the second one a full cartridge was applied.

The second change is related to the geometry of the spigot. The sudden change in diameter creates a large gap between the fiber and the spigot, as shown in Figure 5-18. In Figure 5-14 the FBGs under traction are the ones nearer to this gap, meaning this may be a contributing factor.

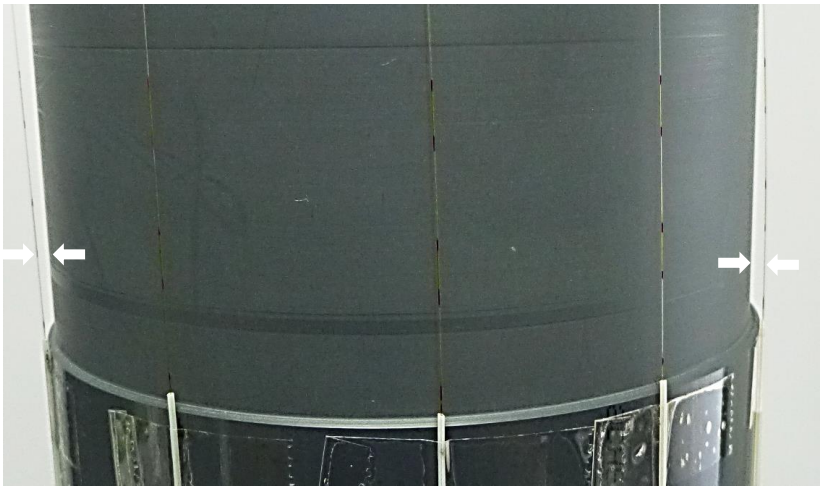

Figure 5-18 - Gap between the fibers and the spigot due to the machining done to the spigot.

This problem was solved by cutting small grooves with a file to smoothly conduct the fibers into the area that will be bonded (Figure 5-19).

Figure 5-19 - Grooves help to conduct the fibers smoothly, eliminating the gap seen in the previous image.

The strain field for this bonded joint, depicted in Figure 5-20 and Figure 5-21 has a more promising look. All sensors are experiencing compressive strain and the field exhibits an approximate rotational symmetry.

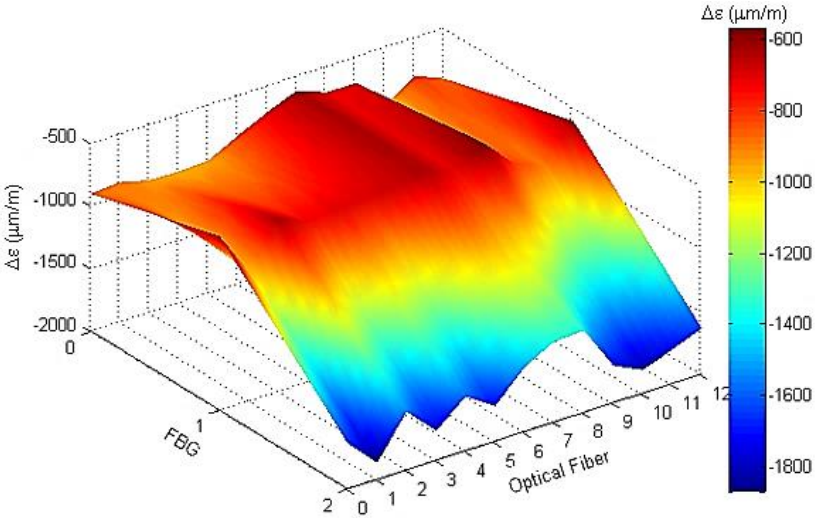

Figure 5-20 - 3D plot with color bar of the cure strain distribution in the adhesive layer. Test specimen B.

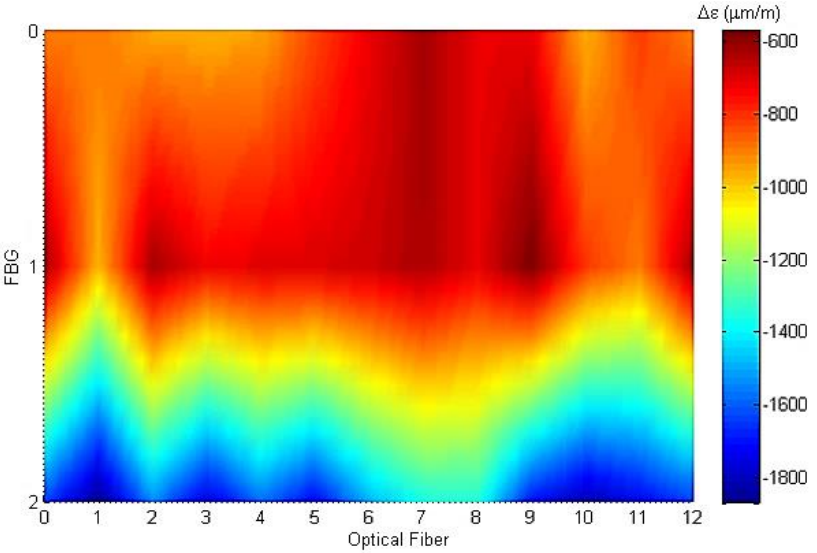

Figure 5-21 - Color plot of the cure strain distribution in the adhesive layer. Test specimen B.

The prospect of a higher quality bonded joint is confirmed by the results from the CT. The 3D rendering in Figure 5-22 is quite different from the previous specimen. There are no big voids like before, instead many small pores can be observed. This is likely the result of entrapped volatile compounds from the adhesive, since it has a sharp exothermal curve and the bonded joint is an enclosed space.

It is unlikely that a porosity free bonded joint can be manufactured with the available materials, but since this does not seem to adversely affect the response of the sensors, this will be considered as a good quality bonded joint for comparison purposes.

Since a good quality joint was achieved in the second try and this specimen also doubles as a good instrumented joint for destructive testing, the total number of required specimens can be reduced from the original seven to six.

Figure 5-22 - 3D rendering of the CT images. Transparency is used to observe the internal structure of the joint. Porosity is observed here instead of numerous large voids.

Inn specimen B, the optical fibers remain invisible inside the bonded region, but it is possible to see how the grooves are producing the expected results (Figure 5-23).

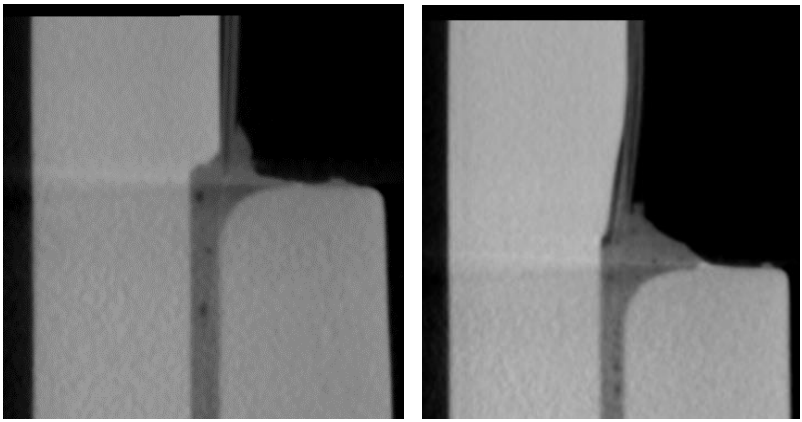

Figure 5-23 – An optical fiber entering the adhesive layer in a test specimen without guiding grooves (left) and with guiding grooves (right).

5.1.3 Specimen C

Having perfected and validated the bonded joint assembly method, the next logical step is to include planned defects for comparison purposes.

Three small inclusions (Figure 5-24), one circle with a diameter of approximately 20 mm, one square with 20 mm sides, and a 20 mm by 70 mm rectangle were prepared. They consist of three layers of aluminum tape, for better visibility in the CT imagens, and one layer of Teflon sheet for its low adherence.

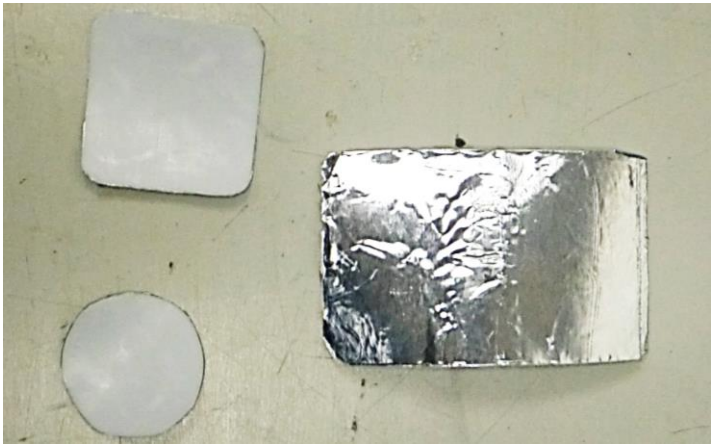

Figure 5-24 - Artificial inclusions made of aluminum tape and Teflon.

The inclusions were then fixed to the sleeve (Figure 5-25) by applying a small amount of instant cyanoacrylate glue around their edges. This will simulate three debonded regions with different sizes and geometries.

Figure 5-25 - Inclusions bonded to the sleeve.

After the joint assembly, the FBG sensors were read. Once more all sensors are under compressive strain, and while the strain field in Figure 5-26 has an overall shape similar to the one in Figure 5-20 some particularities can be observed.

This is more evident in the color plot in Figure 5-27, where the approximate location of the defects is overlaid to the strain field. There is a clear difference around the area where the larger rectangular defect is expected to be, which is promising.

On the other hand, the smaller defects apparently did not produce a significant enough change in the strain field to be evidently noticed. This may be because they are overshadowed by the strain from the adhesive shrinkage. If this is the case they may show up in the hydrostatic tests in the next section.

All three inclusions are visible in the 3D rendered model back from the CT (Figure 5-28).

The exact position of the inclusions can be determined by looking at the cross-sectional cuts, such as the one in Figure 5-29. Their actual position is very close to the ones shown in Figure 5-27. The adhesive layer also seems to be even less porous in relation to test specimen B.

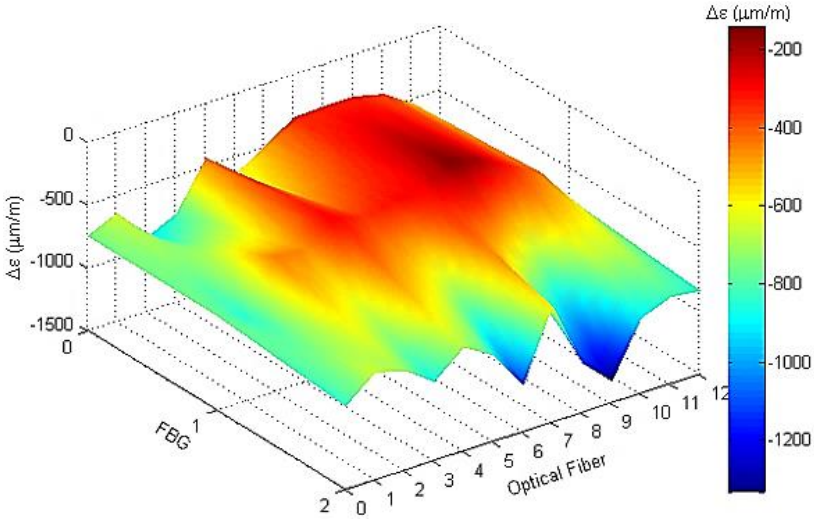

Figure 5-26 - 3D plot with color bar of the cure strain distribution in the adhesive layer. Test specimen C.

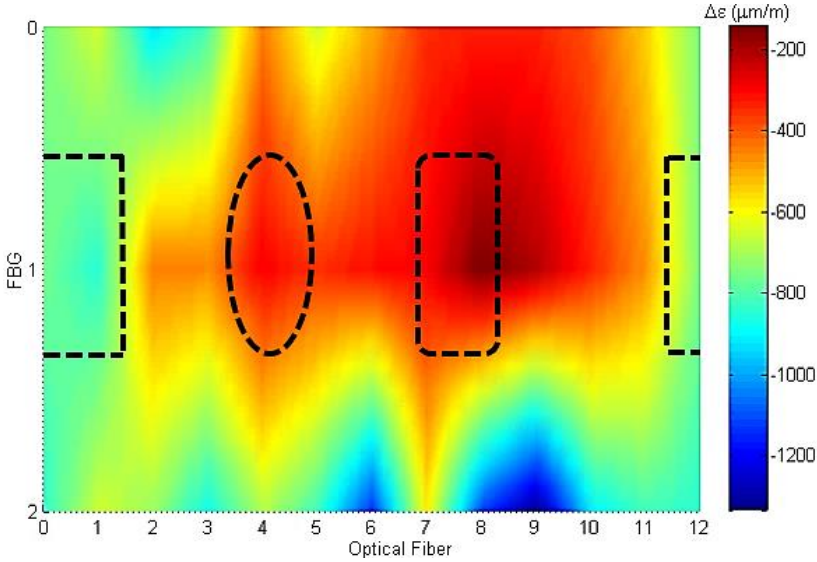

Figure 5-27 - Color plot of the cure strain distribution in the adhesive layer. Test specimen C. The dashed lines define the approximate position of the artificial defects (defect shape distorted due strain map axis scaling).

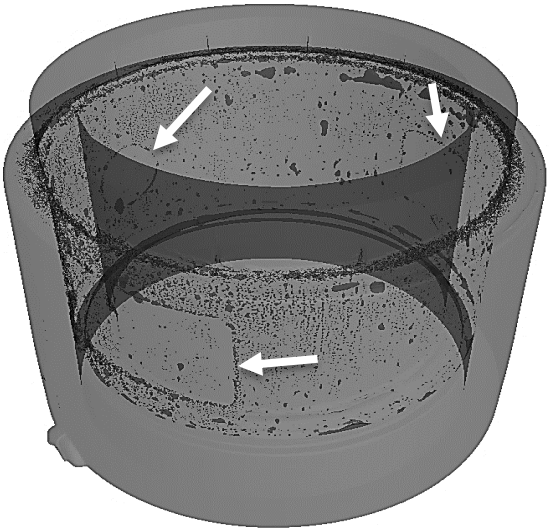

Figure 5-28 - 3D rendering of the CT images. All three inclusions can be seen; they are indicated by arrows.

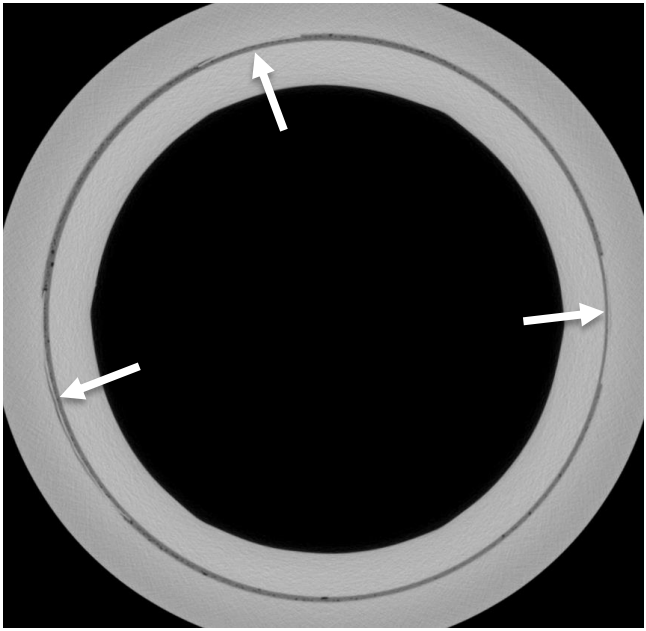

Figure 5-29 - Cross sectional cut from the bonded joint of specimen C showing the exact position of the inclusions (indicated by the arrows).

5.2 Defect Detection with Embedded Sensors

Hydrostatic testing requires the test specimens to be fully assembled. Internal pressure variation will also be used in the tests together with the digital shearography equipment (Figure 5-30).

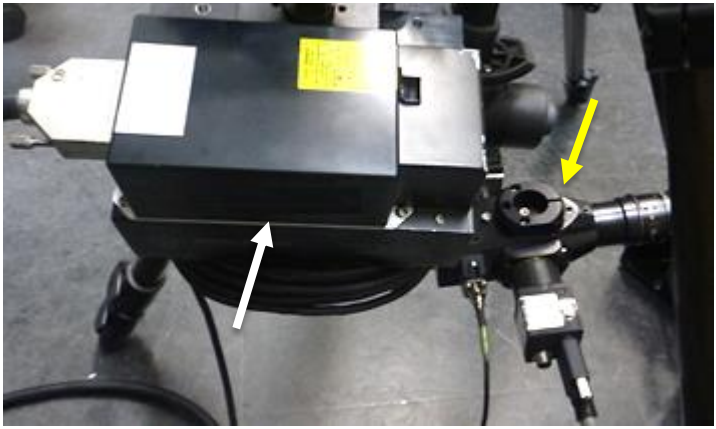

Figure 5-30 - Digital shearography equipment. A 300 mW single longitudinal mode 532 nm laser with expansion lenses (white arrow), and lateral shearing interferometer with attached digital camera and objective lens (yellow arrow).

Specimen B was assembled with a second adhesive bonded joint for the upcoming destructive test. There is no interest in performing destructive tests with test specimen A and C, so both had the flanged pipe piece solvent bonded to the vacant side of their sleeves.

A matching blind flange (Figure 5-31), with a ¼" NPT thread for connecting a manual hydraulic pump, was designed and machined out of a 1040 steel plate to seal the test specimens.

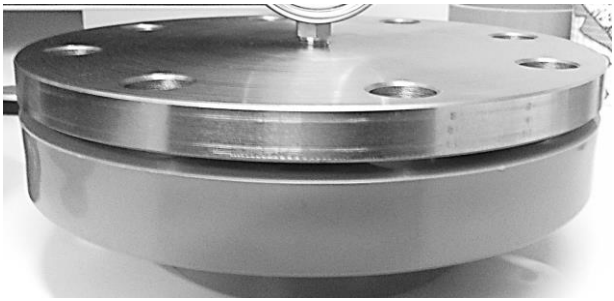

Figure 5-31 - Matching 1040 steel flange with 1/4" NPT thread.

For the digital shearography tests the sleeves were painted mat white and divided in four equal areas. A small structure available in the laboratory was used to keep the specimens in the vertical position. This structure and the painted sleeve can be seen in Figure 5-32.

Figure 5-32 - Test specimen B with the sleeve painted mat white and divided in four equal areas. It is being kept in the vertical position by a metal structure and industrial fabric belts.

It is important to notice that the sleeve has an internal stop at half the way through (Figure 5-33). Since there will not be a pipe inserted in this region, it is expected that this will produce a distinct fringe pattern in the shearography maps.

For the hydrostatic tests, the specimens were laid horizontally, supported by the blind flange and the cap. Strain data will be acquired for various internal pressure values and all $\Delta\varepsilon$ maps will use the zero internal manometric internal pressure strain values as reference.

For a pristine joint, it is expected that when comparing strain distribution from higher pressures in relation to zero, the result is a fully tractive $\Delta\varepsilon$ map.

Figure 5-33 – A stop inside the sleeve.

Even though the maximum internal pressure during this tests will not exceed 8 bar (0.8 MPa) and this pipe is rated for 22 bar (2.2 MPa), a small protective chamber window was placed around the sleeve to avoid water and oil spillage on nearby electronic devices in case of premature failure of the bonded joints (Figure 5-34).

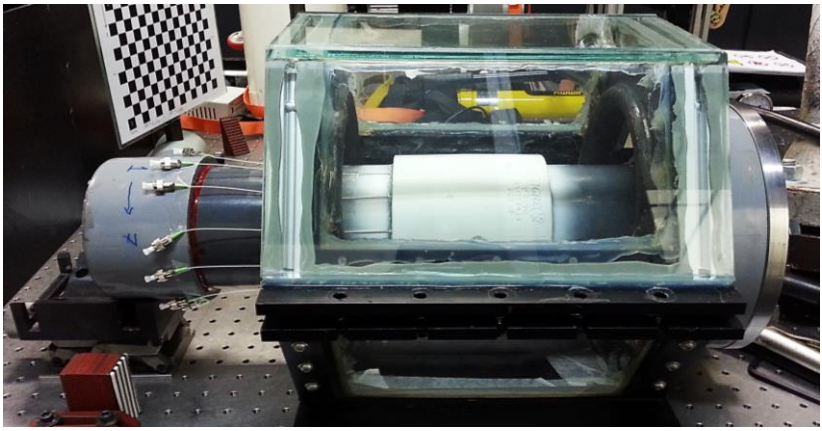

Figure 5-34 - Setup for hydrostatic testing of the instrumented adhesive bonded joints.

5.2.1 Specimen A

Strain distribution was mapped for internal manometric pressure from 0 bar to 7 bar, with 1 bar increments. As pressure increases, the shape of the strain distribution remains almost identical while strain values scale with the applied pressure (Figure 5-35).

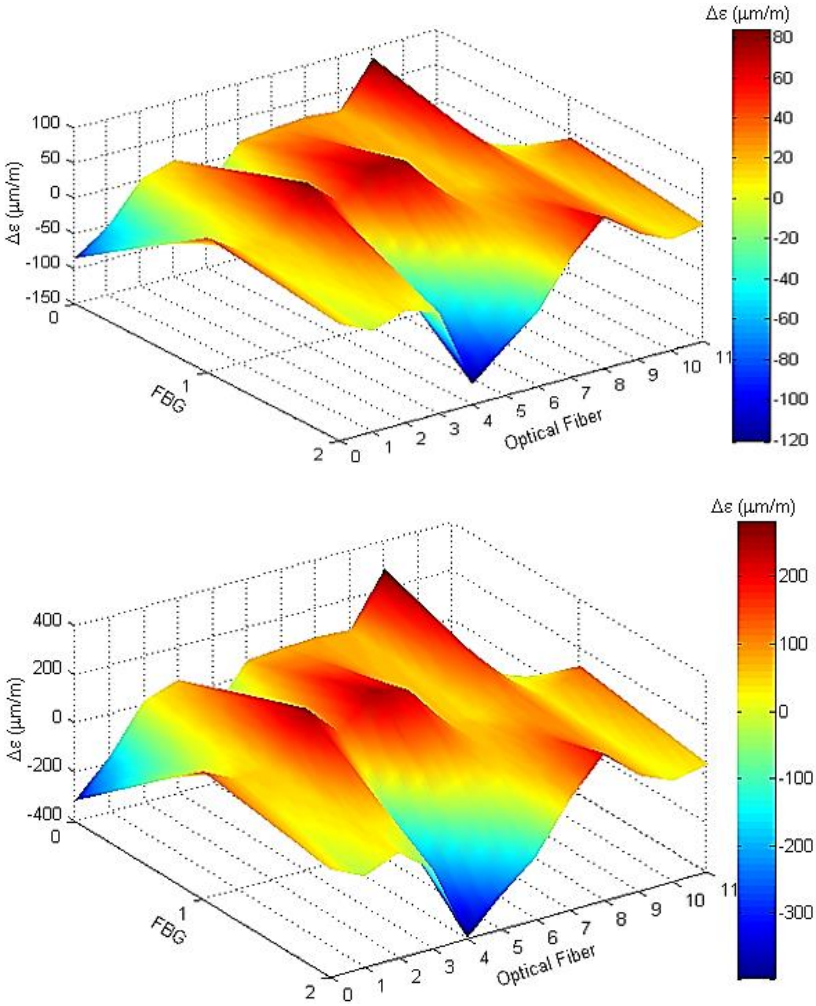

Figure 5-35 - 3D plot with color bar of Δε in the adhesive layer. Specimen A. Internal pressure variation: 2 bar (up) and 6 bar (down).

Strain distribution for specimen A is once again disarranged. No rotational symmetry is observed and various FBGs are experiencing compressive strain, which is the opposite of what was expected for a flawless bonded joint.

Figure 5-36 is the 2D color plot of the Δε map for a Internal pressure variation of 7 bar. It has been divided in four areas that correspond to the ones in the surface of the sleeve for the digital shearography test.

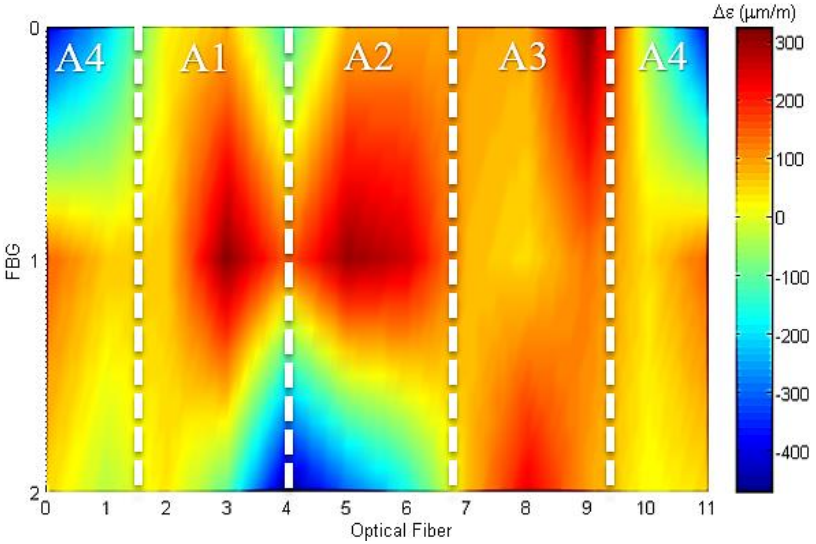

Figure 5-36 - Color plot of Δε in the adhesive layer. Test specimen A. Internal pressure variation: 7 bar.

Area 3 has the most uniform strain distribution, which indicates a lack of defects. The FBGs in the upper portion of area 4 are compressed, hinting at the presence of a defect near the stop by the middle of the sleeve. Areas 1 and 2 have compressed FBGs where the fibers enter the adhesive layer. This result will be compared to the shearograms to verify if the defect indicatives match.

Figure 5-37 shows how the shearography equipment sees the test specimen. The double image is a result of the lateral shearing interferometer. The dashed square to the right is the adhesive bonded region of the sleeve, with the embedded sensors. The dashed square to the left is the solvent bonded region. The space between them contains

the sleeve's stop. The axis labeled as 'x' and 'y' correspond respectively to the horizontal and vertical axis in Figure 5-36.

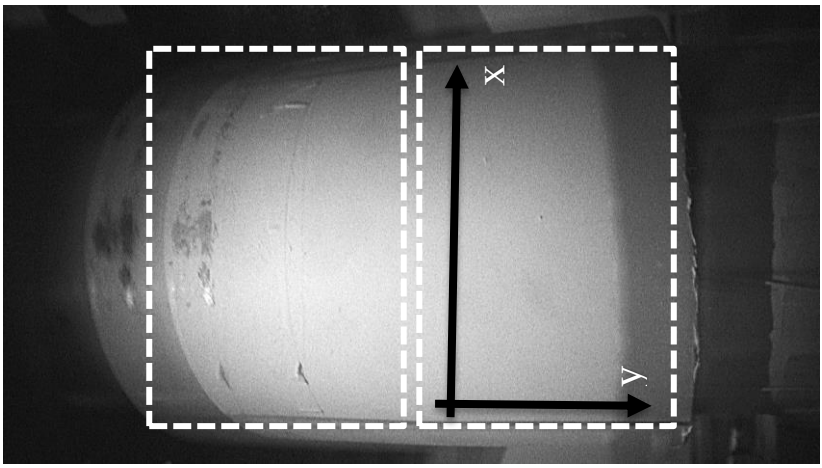

Figure 5-37 - Double image of area 1 as seen by the camera of the shearography equipment.

All shearograms in this chapter will follow the conventions defined in Figure 5-36.

From the fringe maps in Figure 5-38, Figure 5-39, Figure 5-40 and Figure 5-41, it is clear that the sleeve's stop creates a divide in the fringe maps, creating two distinct strain fields that must be analyzed separately. This distinction is necessary since the fringes around this area are very similar to the ones caused by an internal defect, such as the ones in Figure 2-20 and Figure 2-21.

In the shearograms, the areas were disturbances in the fringe patterns indicate the presence of defects are delimited by red dashed rectangles.

The shearograms for area 1 (Figure 5-38) and area 2 (Figure 5-39) exhibit signs of sub-surface defects in the outermost side of the adhesive bonded region, in agreeance to the defect indications from the strain map. The fringes interpretation will be more understandable after reading the next section and comparing the results.

Area 3 shearogram (Figure 5-40) has an almost uniform fringe pattern. A small defect that does not appear in the strain map was detected in the lower right region of the bonded joint.

Area 4 shearogram (Figure 5-41) is also in accordance to the strain map, indicating the presence of defects in the upper half of the bonded region.

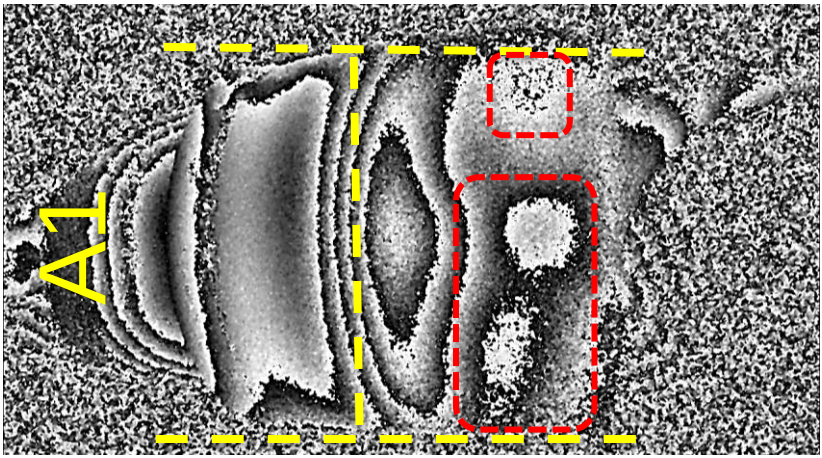

Figure 5-38 - Shearogram of area 1. Test specimen A. Internal pressure variation in relation to the reference phase map: 1 bar.

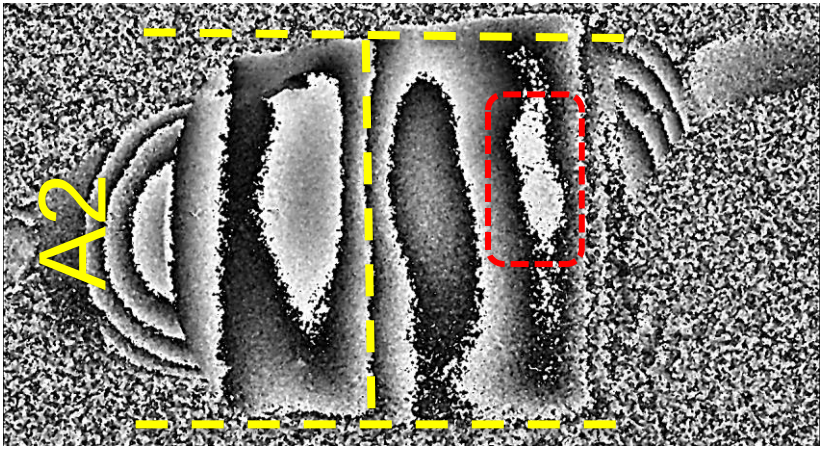

Figure 5-39 - Shearogram of area 2. Test specimen A. Internal pressure variation in relation to the reference phase map: 1 bar.

There is a good correlation between the strain field measured with the FBGs and the fringe maps. Regions with sensors under compressive strain also exhibit disturbances in the corresponding fringe

maps that confirms the presence of defects. The only exception is the small defect in area 3 that was not detected by the FBGs.

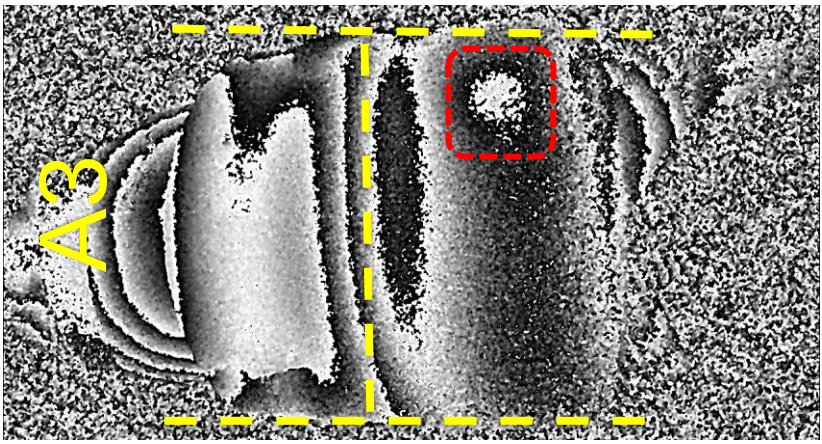

Figure 5-40 - Shearogram of area 3. Test specimen A. Internal pressure variation in relation to the reference phase map: 1 bar.

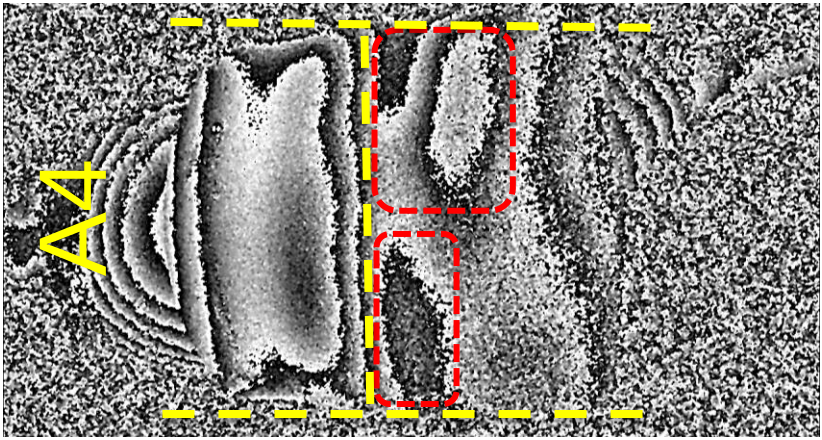

Figure 5-41- Shearogram of area 4. Test specimen A. Internal pressure variation in relation to the reference phase map: 1 bar.

5.2.2 Specimen B

As with specimen A, strain distribution was mapped for internal manometric pressure from 0 bar to 7 bar, with 1 bar increments. Similarly, the shape of the strain distribution remains almost identical while strain values scale with the applied pressure (Figure 5-42).

In comparison to test specimen A, the strain distribution is much more uniform. All FBGs are under tensile strain and a good amount of rotational symmetry can be observed.

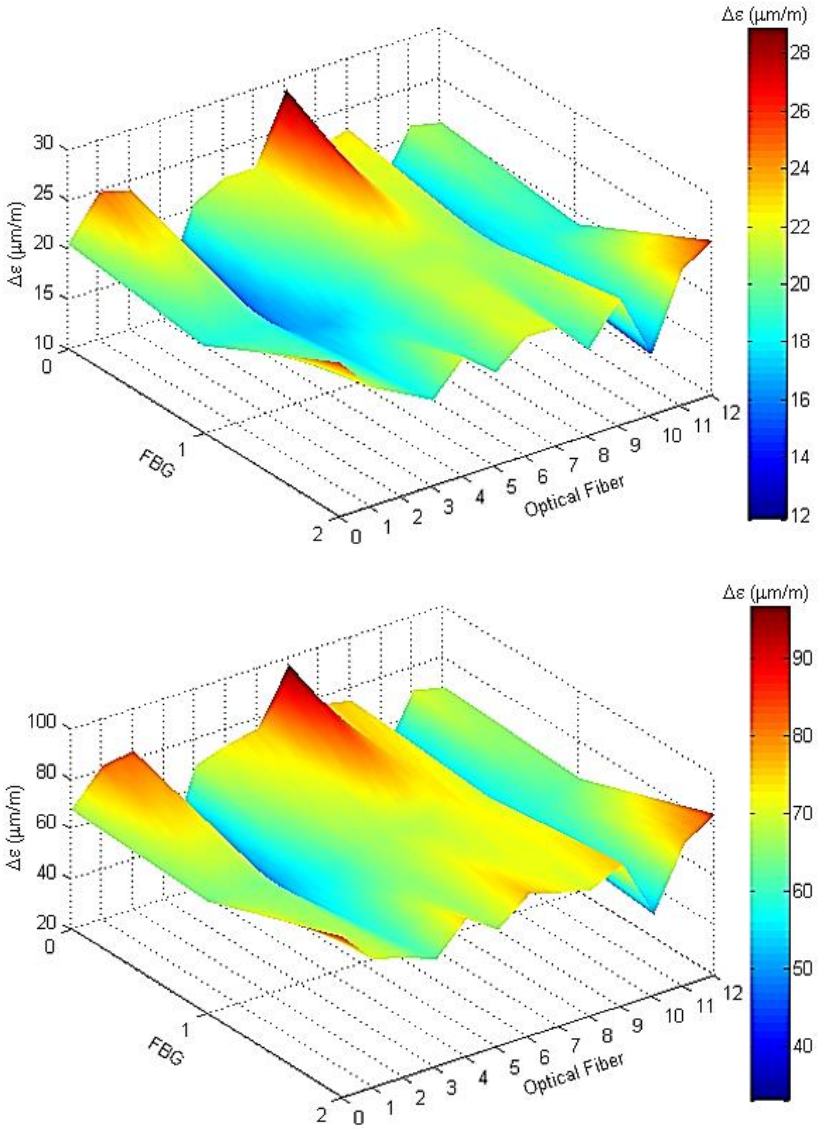

Figure 5-42 - 3D plot with color bar of Δε in the adhesive layer. Specimen B. Internal pressure variation: 2 bar (up) and 6 bar (down).

A few FBGs stand out with significantly lower strain levels, this is more evident Figure 5-43. Looking at Figure 5-42 and Figure 5-43 it seems that the anomalous readings are symmetric in relation to fiber 7.

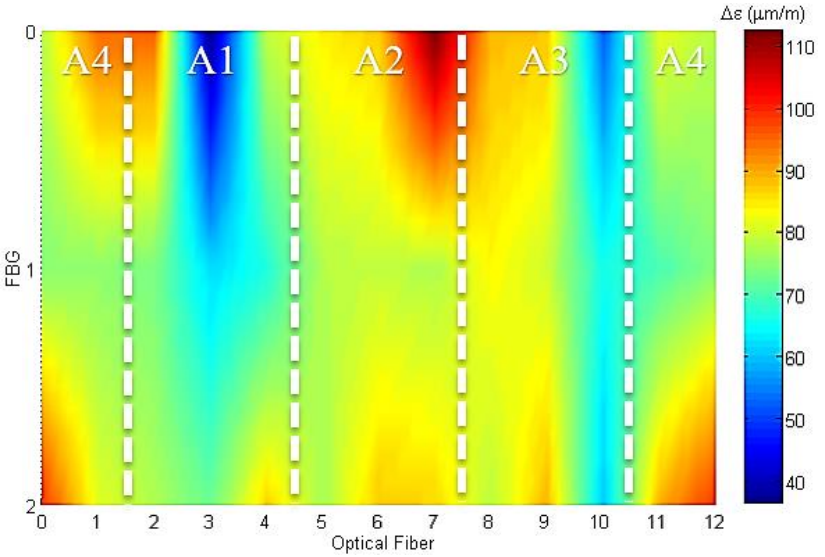

Figure 5-43 – Color plot of Δε in the adhesive layer. Test specimen B. Internal pressure variation: 7 bar.

This lead to the suspicion that supporting the test specimen by the flange and the cap introduced a flexural loading in the sleeve that changed due to pressure stiffening of the pipe. To test this hypothesis the test specimen was rotated by 90º around its axis. If the hypothesis hold, the perceived symmetry will shift laterally in the strain map.

Figure 5-44 is the resulting strain distribution after the rotation, for a Internal pressure variation of 7 bar. The new strain map is almost identical to the previous, the pressure stiffening hypothesis is incorrect. As the results from the CT scan do not exhibit large defects it is possible to propose that this behavior is a result of pores near those sensors.

The information obtained by rotating the test specimen, however, can still be used for an interesting analysis of the flexural strain in the sleeve. The plots in Figure 5-45 and Figure 5-46 were obtained by comparing the strain field for an internal pressure of 7 bar before and after the test specimen was rotated. These flexural strain maps are very smooth and highly symmetrical, showing no evidence of defects.

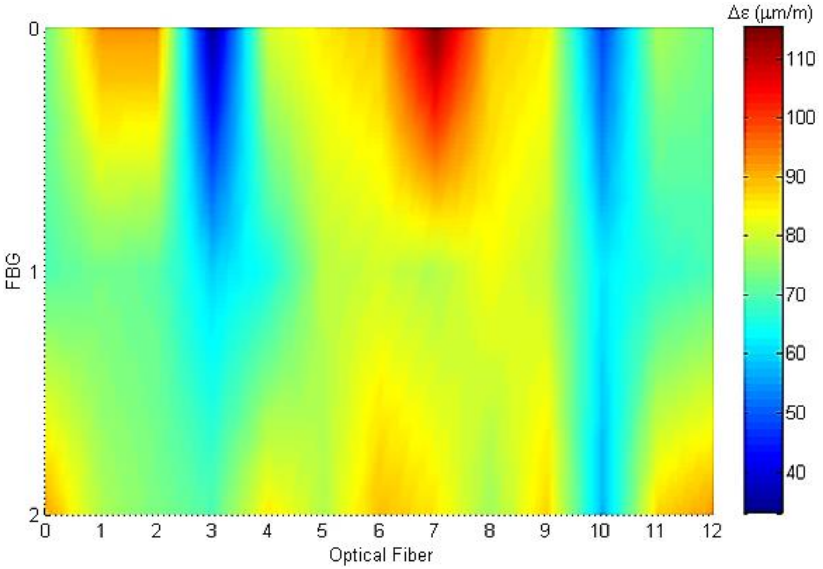

Figure 5-44 - Color plot of Δε in the adhesive layer after rotating test specimen B. Internal pressure variation: 7 bar.

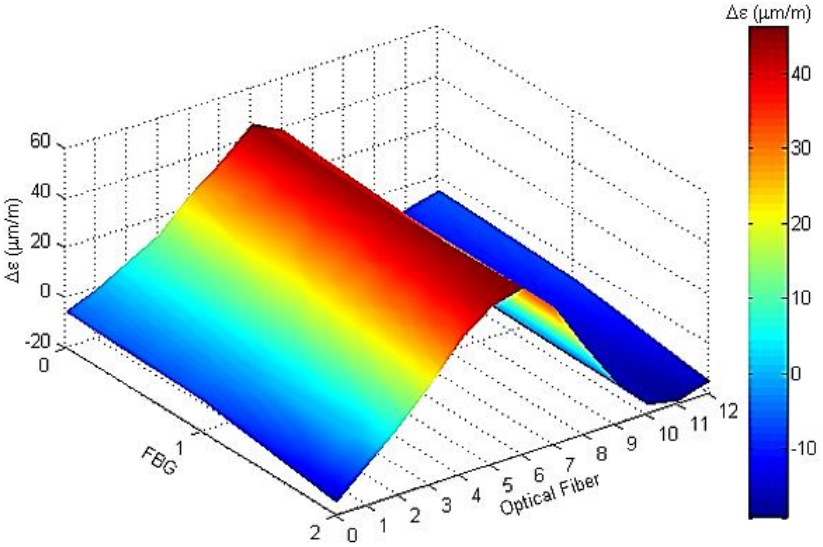

Figure 5-45 - 3D plot with color bar of the flexural strain change in the adhesive layer after rotating test specimen B.

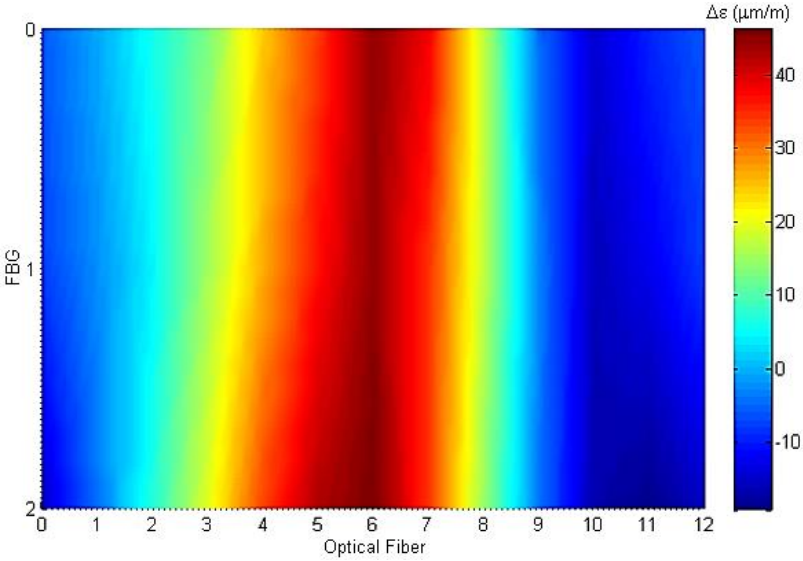

Figure 5-46 - Color plot of the flexural strain change in the adhesive layer after rotating test specimen B.

As for the fringe maps obtained with the digital shearography equipment (Figure 5-47, Figure 5-48, Figure 5-49 and Figure 5-50), there is no indication of internal defects. They all do not exhibit disturbances in the fringe patterns as seen in the Specimen A shearograms.

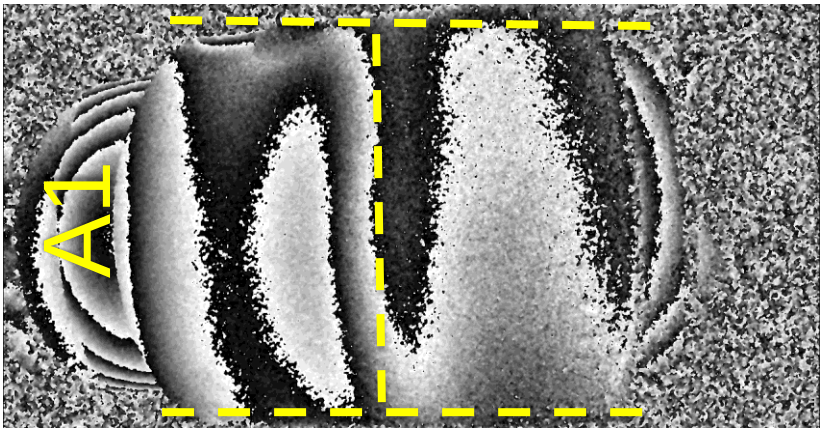

Figure 5-47 - Shearogram of area 1. Test specimen B. Internal pressure variation in relation to the reference phase map: 1 bar.

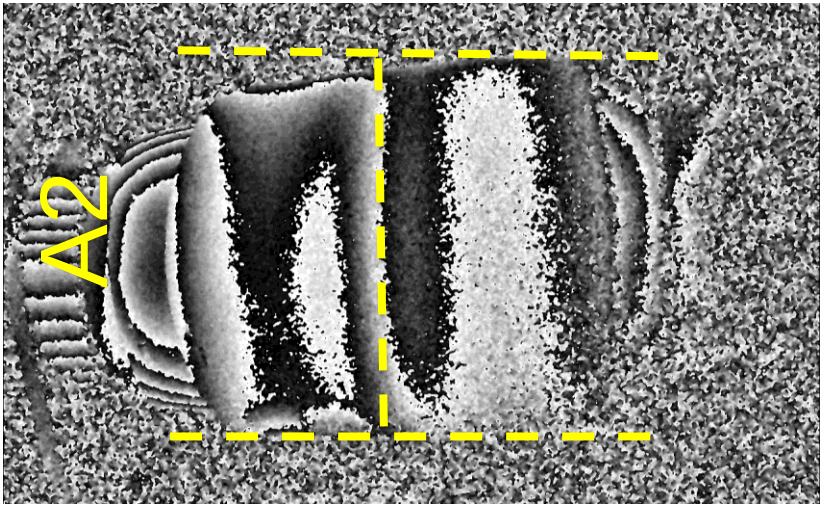

Figure 5-48 - Shearogram of area 2. Test specimen B. Internal pressure variation in relation to the reference phase map: 1 bar.

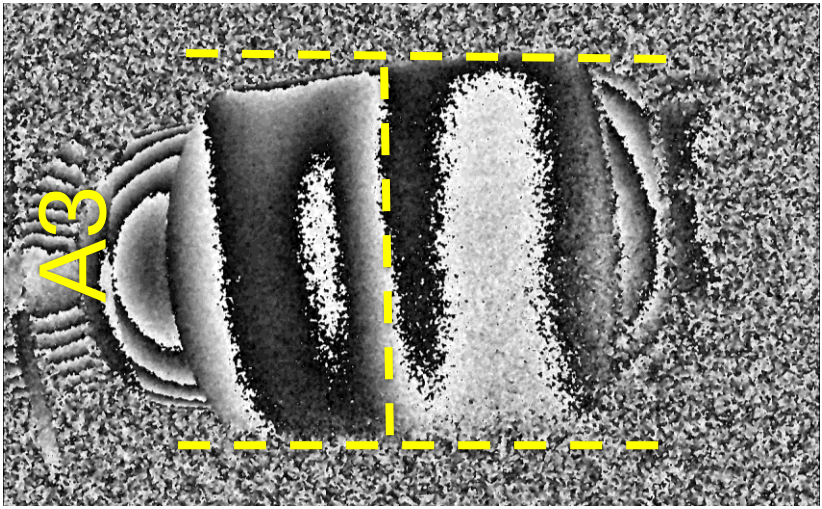

Figure 5-49 - Shearogram of area 3. Test specimen B. Internal pressure variation in relation to the reference phase map: 1 bar.

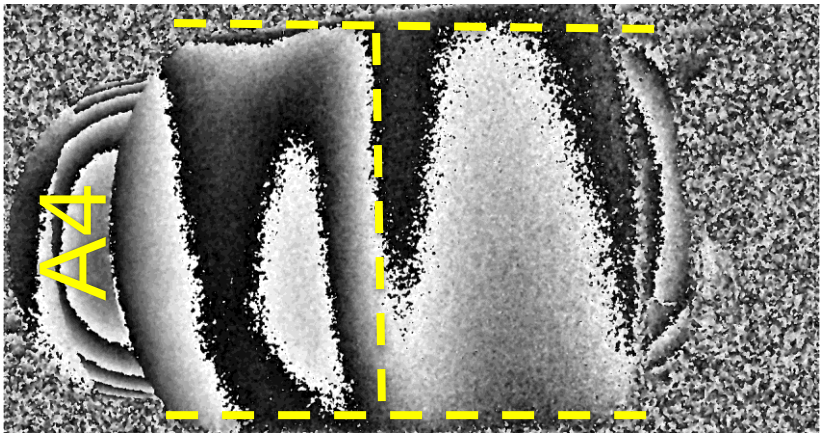

Figure 5-50 - Shearogram of area 4. Test specimen B. Internal pressure variation in relation to the reference phase map: 1 bar.

5.2.3 Specimen C

As previously, strain distribution was mapped for internal manometric pressure from 0 bar to 7 bar with 1 bar increments. The shape of the strain distribution remains almost identical while strain values scale increase in accordance with the applied pressure (Figure 5-51). In comparison to previous specimens the strain distribution is the smoothest one, possibly a reflex of the reduced porosity.

Two of the planned defects were clearly detected by the sensors: The large rectangle in area 4 (Figure 5-52) that spans from fiber 0 to half-way through fiber 1 and 2, and the circle that coincides with fiber 4. The square insert, placed between fibers 6 and 7, was not detected by the FBGs.

Test specimen C was also rotated around its axis to see how the planned defects affect the flexural strain distribution. The large rectangle still produce a visible disturbance in the flexural strain map (Figure 5-53), but the smaller defects are not seen.

Digital shearography (Figure 5-54, Figure 5-55, Figure 5-56 and Figure 5-57) also did not detect the smaller inserts. The large rectangle appears clearly in the shearogram of area 4 (Figure 5-57) and a small part of it is still visible in area 1 (Figure 5-54).

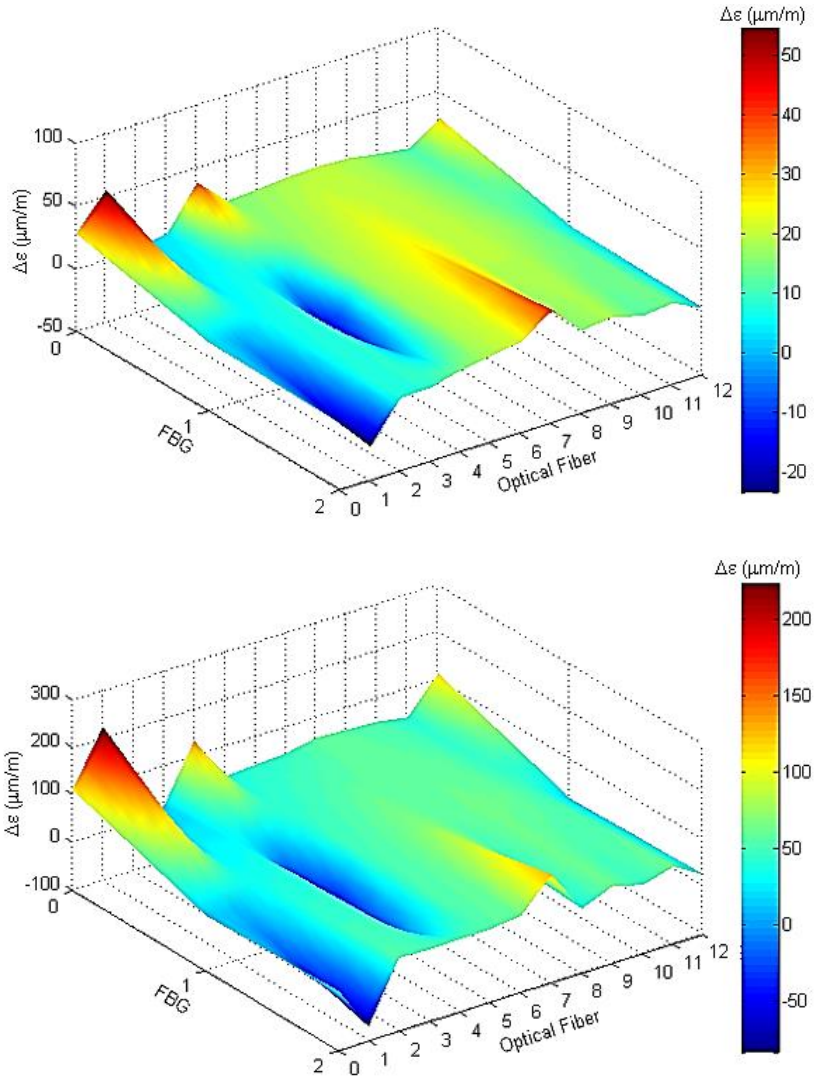

Figure 5-51 - 3D plot with color bar of Δε in the adhesive layer. Specimen C. Internal pressure variation: 2 bar (up) and 6 bar (down).

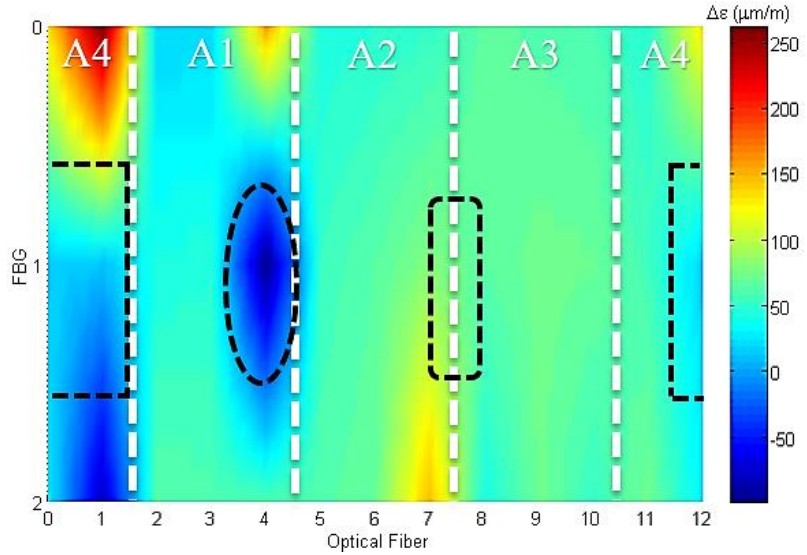

Figure 5-52 – Color plot of Δε in the adhesive layer. Test specimen C. Internal pressure variation: 7 bar. The dashed lines define the approximate position of the artificial defects (defect shape distorted due strain map axis scaling).

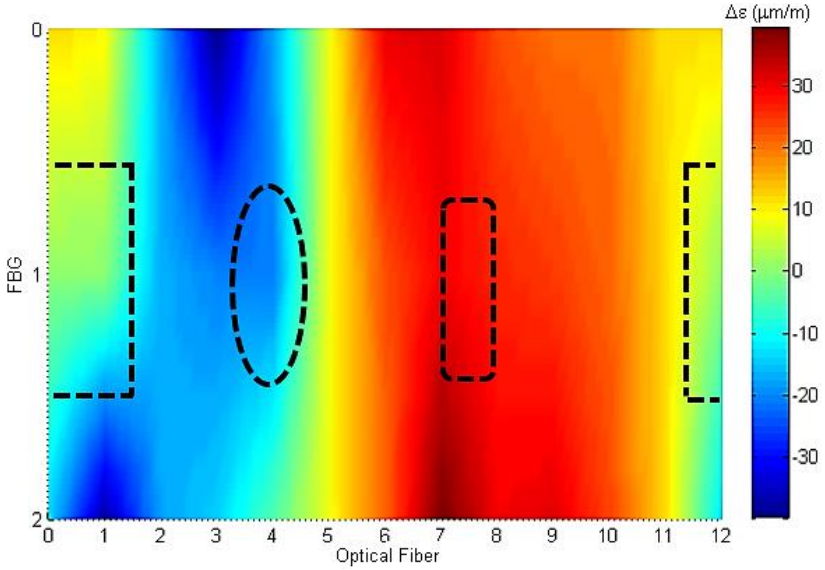

Figure 5-53 - Color plot of the flexural strain change in the adhesive layer after rotating test specimen C. The dashed lines define the approximate position of the artificial defects (defect shape distorted due strain map axis scaling).

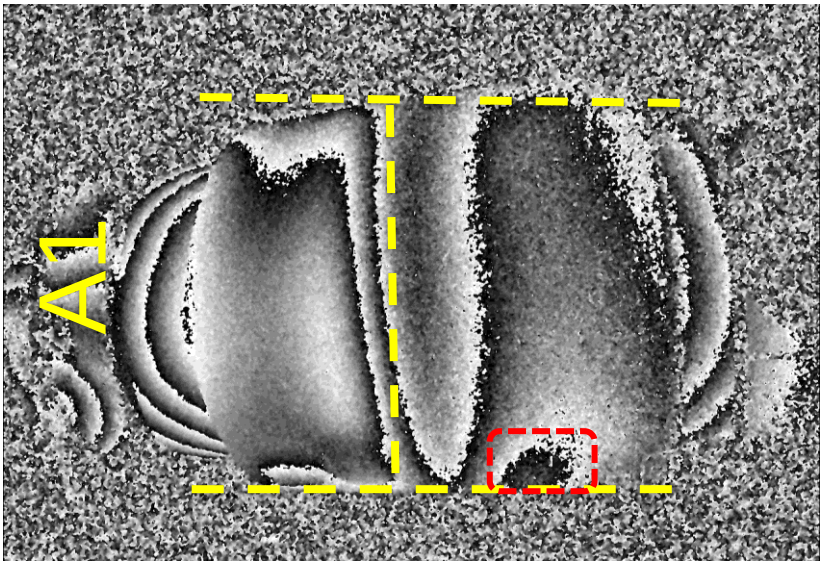

Figure 5-54 - Shearogram of area 1. Test specimen C. Internal pressure variation in relation to the reference phase map: 1 bar.

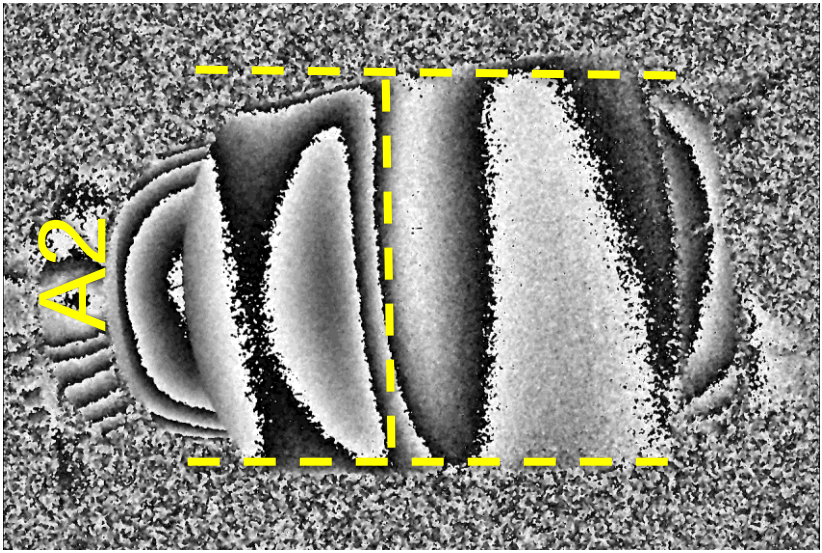

Figure 5-55 - Shearogram of area 2. Test specimen C. Internal pressure variation in relation to the reference phase map: 1 bar.

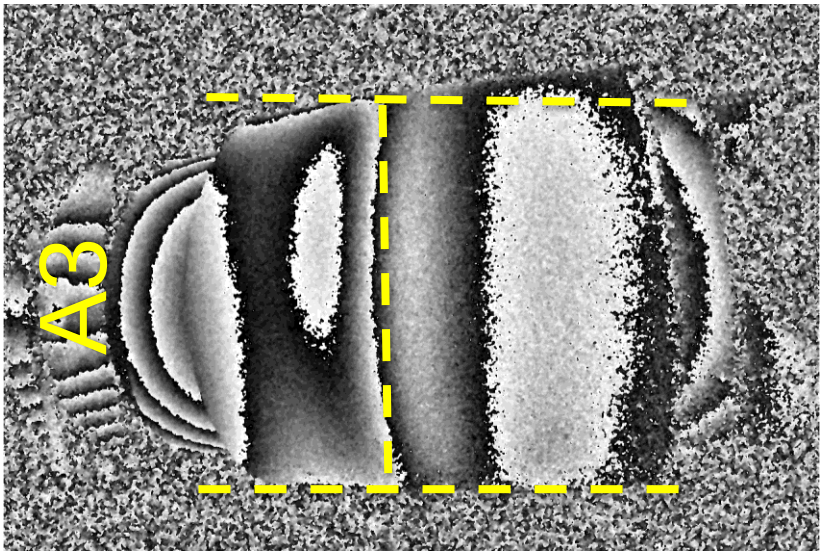

Figure 5-56 - Shearogram of area 3. Test specimen C. Internal pressure variation in relation to the reference phase map: 1 bar.

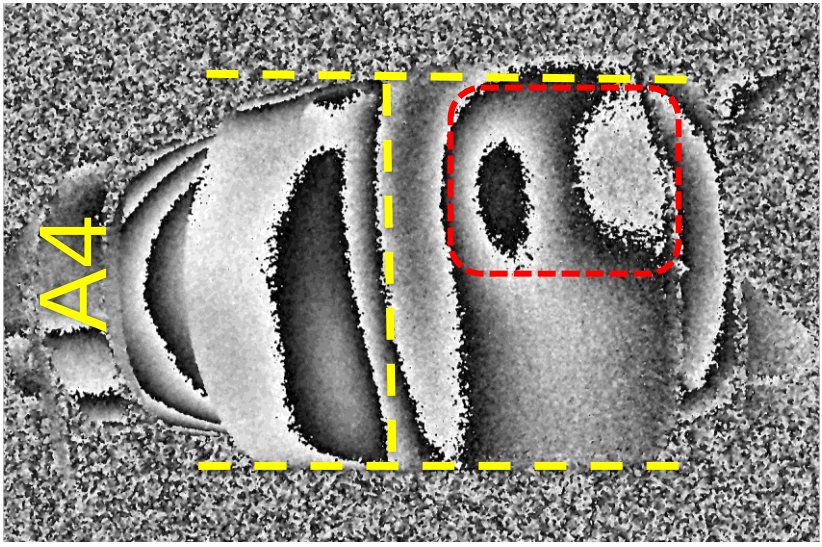

Figure 5-57 - Shearogram of area 4. Test specimen C. Internal pressure variation in relation to the reference phase map: 1 bar.

Test specimen C was used in one last test with one of the longer FBG chains. The 12 FBG chain specified for the 6" fiberglass-epoxy pipe was too long and the last two FBGs were cut out to avoid sensor overlap. The 10 FBG chain was bonded to the surface of the sleeve using the methyl methacrylate adhesive.

Counting from the FC/APC connector, FBGs 1 and 2 are located by the borders of the large rectangle, while FBG 10 is directly on top of it after the fiber wraps around (Figure 5-58).

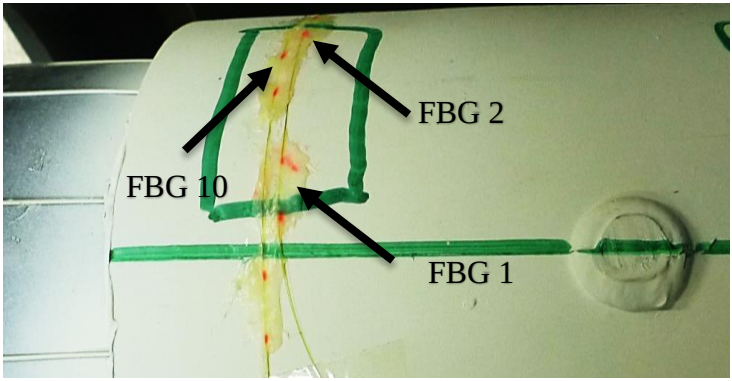

Figure 5-58 – FBGs 1, 2 and 10 bonded around the large rectangular insert.

FBG 5 was bonded on top of the small square insert (Figure 5-59).

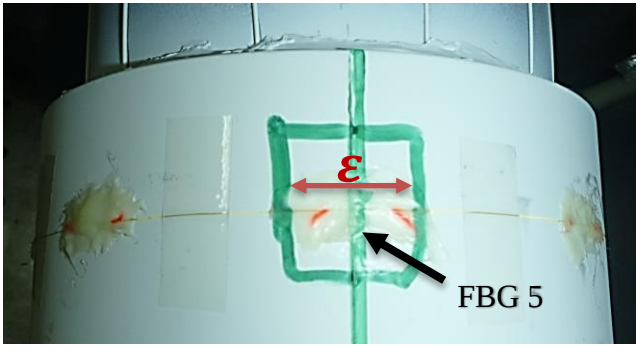

Figure 5-59 – FBG 5 bonded directly on top of the small square insert. The direction of the strain sensitivity of the FBG is indicated by the red arrow.

And FBGs 7 and 8 were bonded close by the small circle insert (Figure 5-60).

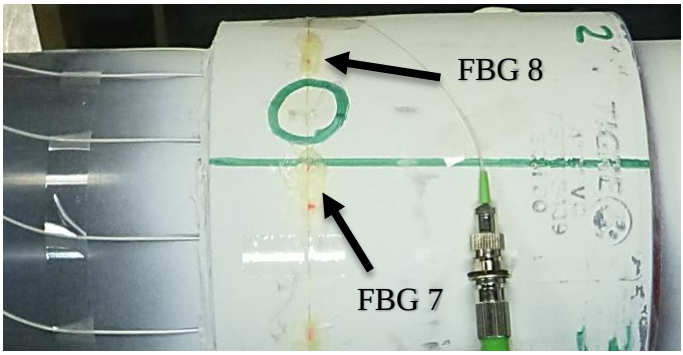

Figure 5-60 - FBGs 7 and 8 on both sides of the small circle insert.

The test specimen was then pressurized up to 8 bar and the 10 FBGs were interrogated every 1 bar. To evaluate if the FBGs placed around the inserts could detect the internal defects based on the circumferential strain distribution on the outer surface of the sleeve, look at the strain profile at 8 bar (Figure 5-61).

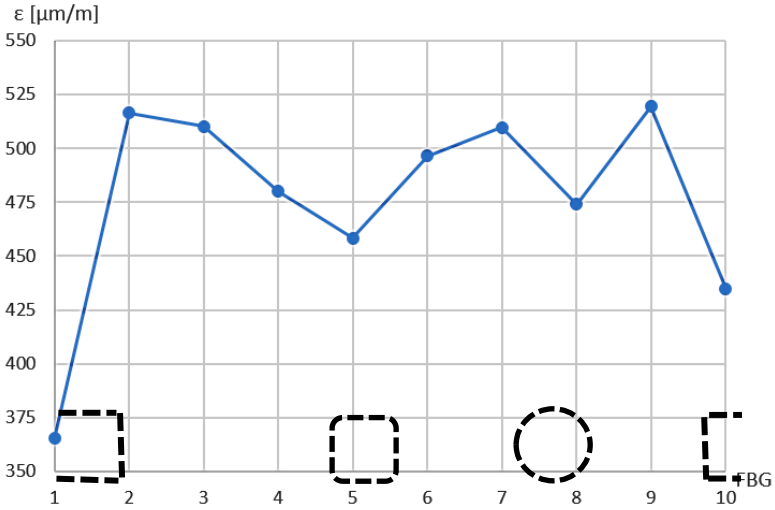

Figure 5-61 – A closer look at the circumferential strain profile for an internal Internal pressure variation of 8 bar. The dashed lines near the horizontal axis shows the approximate position of the inserts in relation to the FBGs.

The evolution of the strain profile along the 10 FBG chain can be seen in Figure 5-62. Non-uniformities become more evident at higher pressures.

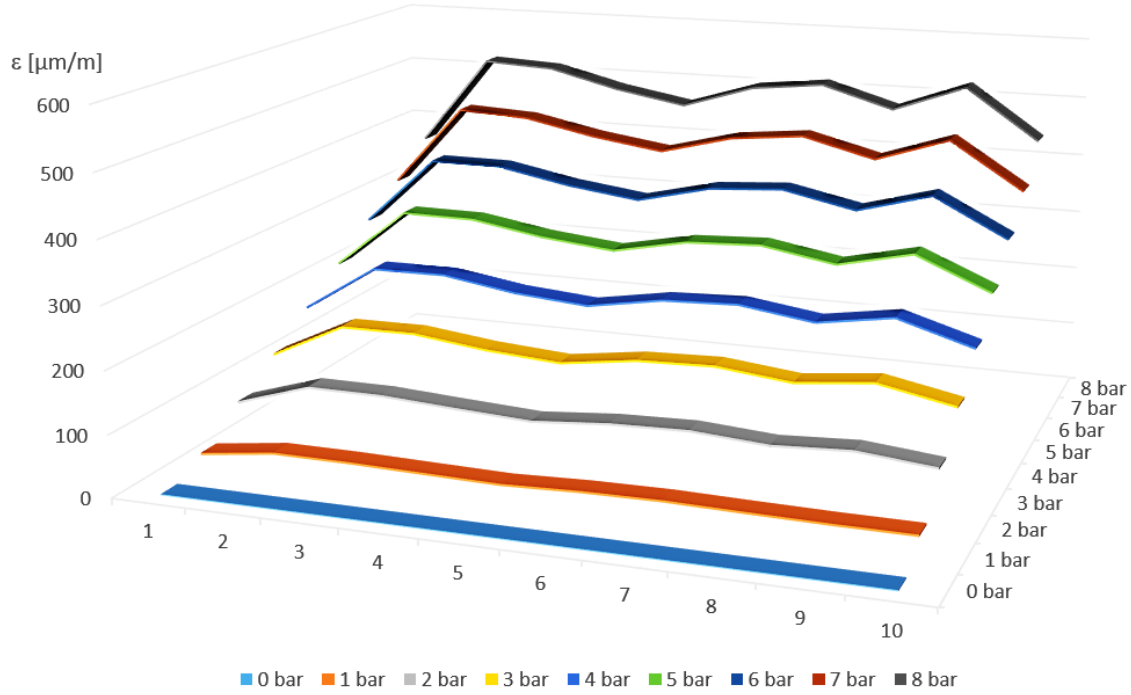

Figure 5-62 – Evolution of the circumferential strain profile along a single line in the outer surface of the sleeve at the adhesive bonded joint.

FBGs 1, 5, and 10 are all close to defects and appear to be subjected to lower strain values. It is possible to use a hypothesis test to determine if they can be considered different from the other points. [85]

The mean strain μ_ε of the other 7 FBGs is 500.83 μm/m. The null hypothesis H_0 and alternative hypothesis H_1 can be defined as:

$$H_0: \varepsilon_{FBG1}, \varepsilon_{FBG5}, \varepsilon_{FBG10} = \mu_\varepsilon$$
$$H_1: \varepsilon_{FBG1}, \varepsilon_{FBG5}, \varepsilon_{FBG10} < \mu_\varepsilon$$

The standard deviation S_ε of μ_ε is 17.95 μm/m. For a significance level α of 0.05, and 6 degrees of freedom, the test statistic T as given by Equation 5.3 must be smaller than the critical value $-T_{\alpha,6} = -1.943$.

$$T = \frac{\varepsilon_x - \mu_\varepsilon}{S_\varepsilon} \tag{5.3}$$

The higher value of T will occur for ε_{FBG5} since it has the highest strain value of the 3 tested FBGs. Substituting the values of μ_ε, S_ε and $\varepsilon_{FBG5} = 458.27\ \mu m/m$ in equation 5.3 returns $T = -2.37$.

H_0 is then rejected and all three strain measurements can be considered different from the mean strain value for a 95% confidence level.

5.3 Instrumentation Impact on Joint Pressure Rating

In the manufacturer's product guide, all 4" CPVC pipes and fittings, except 45º elbows, have an operating pressure rating of 22 bar (2.2 MPa) @ 20 ºC. However, it was not disclosed that the flanges operating pressure rating is 150 psi (1.03 MPa).

With such lower pressure rating, the test specimen is much more likely to fail at the flange. As this will probably lead to inconclusive experiments, no more test specimens were assembled for destructive testing. Only Specimen B was pressurized until failure. This concludes the explanation on why only three out of the originally planned seven test specimens were fully assembled.

For the destructive test, specimen B was placed inside a steel pipe fastened to the ladder of a small bunker under Labmetro (Figure 5-63).

Figure 5-63 - Test specimen B inside a steel pipe fastened to a ladder.

During the test, the entrance to the bunker was sealed using its own concrete trapdoor (Figure 5-64).

Figure 5-64 – Concrete trapdoor sealing the entrance to the bunker.

The test specimen was then pressurized until it failed at the internal pressure of 60 bar. The FBGs were interrogated every 5 bar. Upon reaching 25 bar, 40 bar and 50 bar the manometric pressure was brought down to 0 bar. Comparing the strain field at the zeroes can show the buildup of residual strain.

Figure 5-65 and Figure 5-66 show strain maps in the adhesive layer for various pressure levels. The ongoing trend of very similar strain distributions is still present, with a slight strain homogenization in the bonded joint at higher pressures.

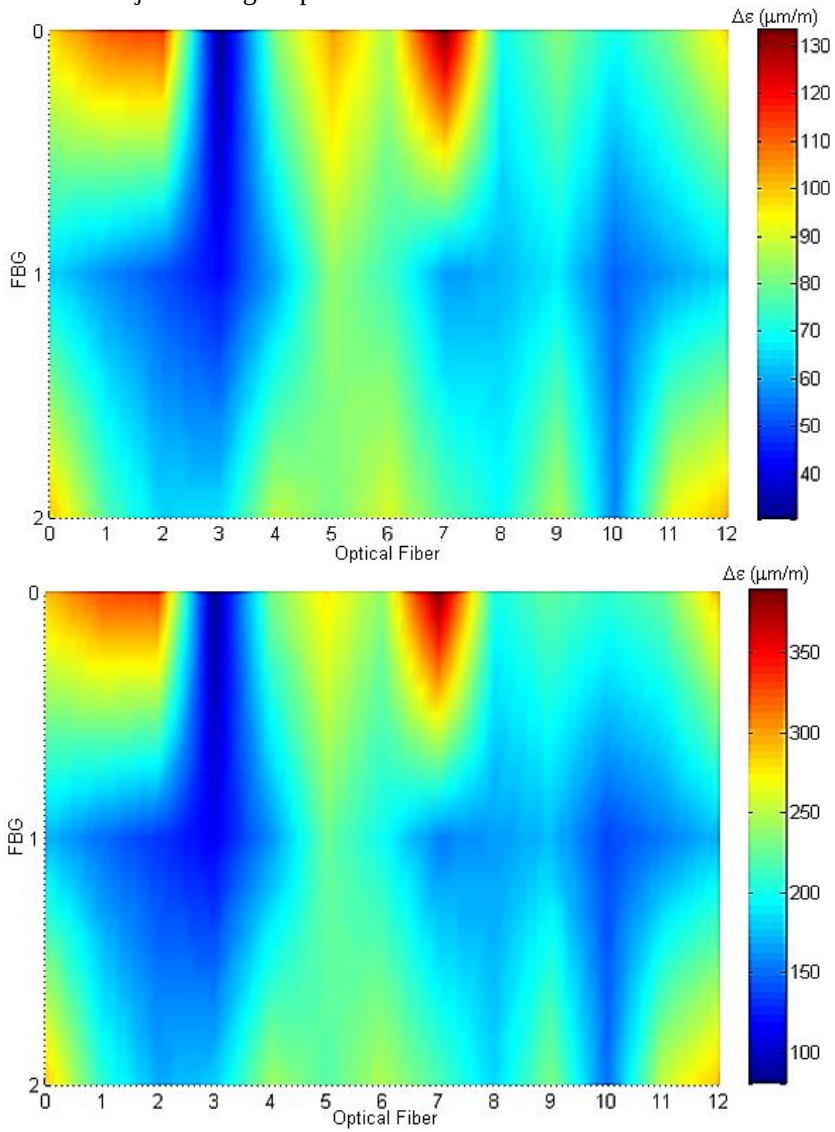

Figure 5-65 - Color plot of Δε in the adhesive layer. Specimen B. Internal pressure variation: 5 bar (up) and 25 bar (down).

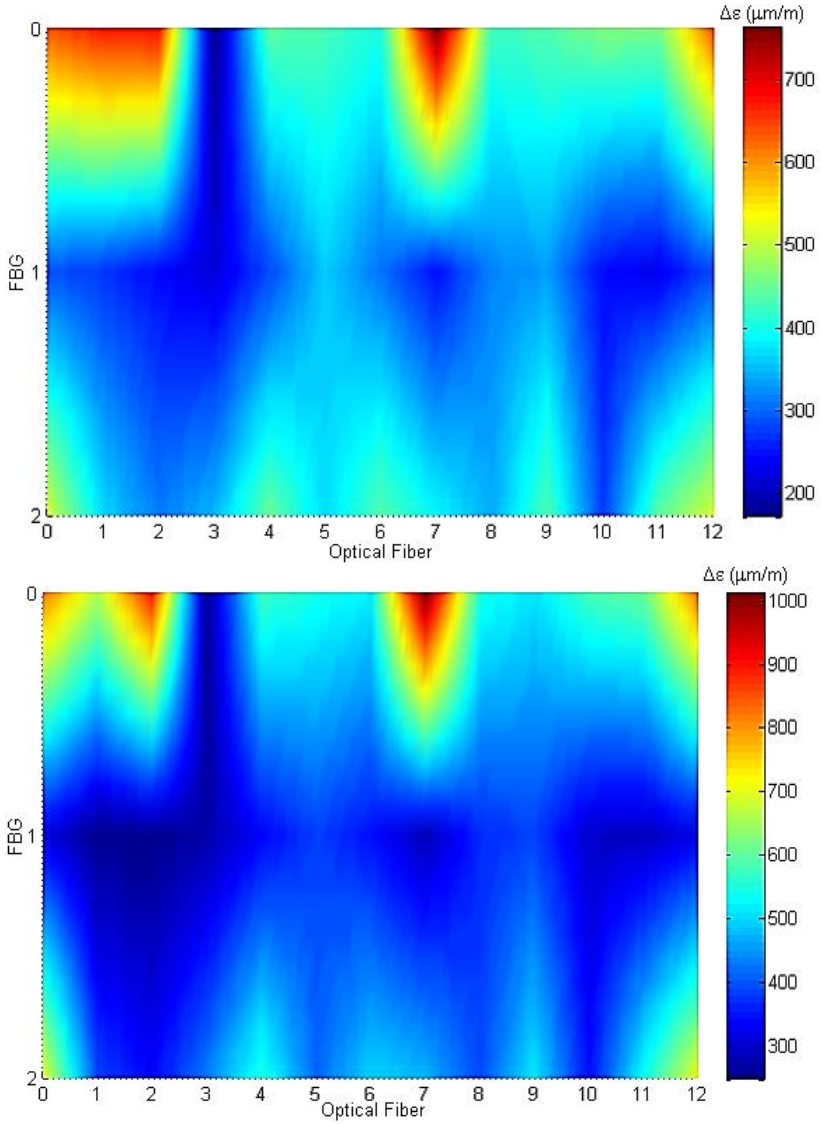

Figure 5-66 - Color plot of Δε in the adhesive layer. Specimen B. Internal pressure variation: 45 bar (up) and 55 bar (down).

The strain maps in Figure 5-67 clearly show an increasing amount of residual strain when lowering the internal manometric pressure back to 0 bar after reaching 25 bar and 50 bar.

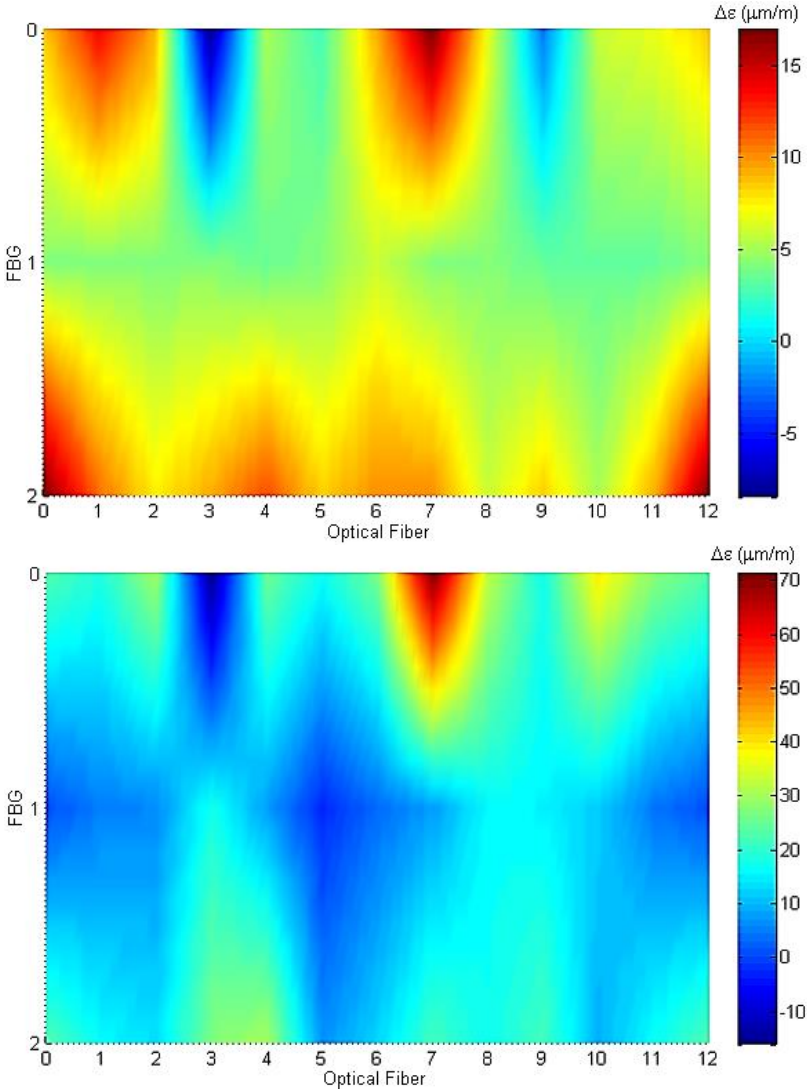

Figure 5-67 - Color plot of Δε in the adhesive layer. Specimen B. Difference between the starting 0 bar and alleviating pressure from 25 bar to 0 bar (up), and from 50 bar (down).

The test specimen failed at the adhesive bonded joint without the optical fiber sensors (Figure 5-68).

Figure 5-68 – Destructive test aftermath. Test specimen B failed in the adhesive bonded joint without embedded fiber optic sensors.

Unfortunately, since the failure did not start in the region with the FBGs, it was not possible to monitor its progression.

6 CONCLUSIONS

This work proposed an integrated sensing solution to monitor the structural integrity of adhesive bonded joints in pipes. Differently from existing solutions that focus on regularly scheduled maintenance, the approach proposed here aims to be compatible with long-term monitoring.

A simple and well known optical fiber sensor was selected and a sensing strategy based on $\Delta\varepsilon$ maps, similarly to optical interferometry techniques such as shearography and holography, was applied.

The objectives set on the first chapter: studying and selecting sensors, elaborating an integrated sensing strategy and evaluating both the sensors and sensing strategy have all been fulfilled.

The following sections summarize the capabilities and limitations of the method that has been proposed and tested, along with presenting suggestions to further develop this study.

6.1 Performance of the Proposed Method

From the results exposed in Chapter 5 it is evident that the proposed method is capable of detecting internal defects in adhesive bonded joints.

While the sensors embedded into the adhesive layer could not detect all three defects purposely introduced into test specimen C, the combined approach of embedding and wrapping sensors could.

The results obtained from the optical fiber sensors were in agreeance with the much more detailed computed tomography scans, which is a technique with severe limitations for in field applications. They were also on par with shearography for detecting larger defects and was able to detect the smaller defects that did not appear in the shearograms.

Even while focusing only on joint assemble and long-term monitoring, the method proved itself to be effective for monitoring the pipeline assembly process by providing a detailed flexural strain profile. The sensors can be used during this stage to monitor if excessive loads were introduced in the joints when misalignments are corrected by force.

By mapping $\Delta\varepsilon$ instead of absolute strain values, the method allows all stages of the pipeline lifecycle to be monitored independently by keeping strain comparisons intra-stage only.

6.2 Sensing Strategy Limitations

It is important to know that this approach is not able to reject, or approve, an inspected bonded joint per the criteria defined by the standards cited in section 4.1.2, as the FBGs are quasi single-point strain sensors and the standards reject a joint based on total defect area.

The tests with planned defects showed that the FBGs are very good at detecting voids and debonded areas when directly adjacent to them, but a defect resting between fibers can go undetected.

A solid sensing coverage is possibly the most important aspect to consider when utilizing this method, otherwise defects can remain unnoticed.

6.3 Suggestions for Future Advancements

6.3.1 Tensile Testing

The pressure rating of the plastic flanges undermined the execution of destructive tests. Although the failure occurring away from the embedded fibers is positive, only one destructive test does not bear enough statistical significance to conclude that the embedded sensors have no deleterious effects in the mechanical strength of the joint.

One way to utilize the material already acquired for this dissertation is to substitute the hydrostatic test for a tensile test. The mechanical engineering department of Federal University of Santa Catarina is equipped with a 300 kN tensile testing machine, more than enough to lead the CPVC pipes to failure. An ASTM D2105 tensile grip or similar can be procured and used to fix the test specimens to the machine.

6.3.2 Fibers per Joint versus Joint Strength

With the proper means to extensively execute destructive tests, it would be interesting to evaluate how the number of embedded sensors affects the strength of the bonded joints. This information can be used to obtain the best sensing coverage with minimal intrusiveness.

6.3.3 More Sensors in a Single Fiber

For an even better coverage the number of sensors per fiber can be increased. Three FBGs already have produced very good results for an insertion depth of 57 mm.

From this perspective, the best may be making use of distributed strain sensing with OFDR. The entire fiber can be used as a cheap distributed sensor, with the downside of requiring a more complex interrogation scheme.

6.3.4 Temperature Compensation for Field Testing

Having an instrumented pipeline in the field can provide a lot of invaluable data, but a few problems must be solved before this can be attempted successfully.

The most important point is temperature compensation. In the laboratory it is easy to make temperature a non-issue by keeping it constant during all tests. Without temperature compensation pure strain data cannot be extracted from the sensors.

Chapter 3 already covers a few fiber optic sensors with multi-parameter capabilities and many more can be found in specialized literature. From the ones cited in chapter 3, the thermochromic coating seems to be the easiest to adapt to the current sensing strategy.

6.3.5 Ruggedness for Long-Term Monitoring

Field employed sensors need to be very robust if long-term monitoring capability is desired.

There is ample variety of buffer coating material available, including organically modified ceramics and metallic coatings that can provide a better protection against constant exposure to UV light and humidity. Rugged fiber connectors are also available, some even with IP 68 ratings and salt mist tolerance. Armored fiber optic patch cords and cables are already widespread.

Submarine optical fiber communications technology can provide lots of useful information and design choices for increased ruggedness.

6.3.6 Annealing of the FBGs

The periodic modulation of the refractive index of the FBG decays with time. This decay results in a change of grating reflectivity and nominal Bragg wavelength, which in turn will lead to measurement errors in long-term monitoring applications.

Annealing is a powerful and simple technique to greatly increase the stability of the periodic modulation. References [86] and [87] provide more details on how to anneal FBGs written in regular fibers and in hydrogen loaded fibers.

REFERENCES

[1] DE TARSO R. MENDONÇA, PAULO. **Materiais Compostos e Estruturas Sanduíche**. Manole, Barueri, 2005.

[2] UMECO. **SM1010/03.12/6 – Introduction to Advanced Composites and Prepreg Technology**. 2006.

[3] GAY, D., HOA, V. S., TSAI, W. S. **Composite Materials: Design and Applications**. CRC Press, London, 2003.

[4] BAKER, A. **Composite Materials for Aircraft Structures**. American Institute of Aeronautics and Astronautics, Reston, 2004.

[5] MALLICK, P. K. **Composites Engineering Handbook**. Marcel Dekker Inc, New York, 1997.

[6] UNIVERSITY OF NEW SOUTH WALES (UNSW). **Particle Reinforced Composites**. Retrieved 01/sept/2015 from <http:// www.materials.unsw.edu.au/tutorials/online-tutorials/5-particle-reinforced-composites>.

[7] BREMBO SGL CARBON CERAMIC BRAKES. **Carbon Ceramic Technology**. Retrieved 08/dec/2015 from <http://www.carbonceramicbrakes.com/en/technology/Pages/Technology.aspx>.

[8] BREMBO S.P.A. **Carbon-ceramic discs**. Retrieved 08/dec/2015 from < http://www.brembo.com/en/car/original-equipment/products/carbon-ceramic-discs>.

[9] TORRES, C.S.; SCHAEFFER, L. **Sinterização do compósito metal duro WC-Co**. Revista Eletrônica de Materiais e Processos, v 4.3, pp. 58-63. 2009.

[10] ALL ABOUT CEMENTED CARBIDE. **What are the different types of Cemented Carbide?** Retrieved 08/dec/2015 from <http://www.allaboutcementedcarbide. com/02.html>.

[11] KÖNIG, W.; KLOCKE, F. **Fertigungsverfahren 1: Drehen, Bohren, Fräsen**. Springer, Berlin, 1997.

[12] SANDVIK HARD MATERIALS. **Cemented Carbide, Sandvik new developments and applications**. 2005.

[13] INTERNATIONAL TUNGSTEN INDUSTRY ASSOCIATION (ITIA). **Tungsten Carbide and Cobalt**. Retrieved 08/dec/2015 from < http://www.itia.info/wc-and-co.html>.

[14] THE WELDING INSTITUTE (TWI). **What is a Sandwich Structure?** Retrieved 08/dec/2015 from <http://www.twi-global.com/technical-knowledge/faqs/material-faqs/faq-what-is-a-sandwich-structure/>.

[15] PETRAS, A. **Design of Sandwich Structures**. PhD dissertation – Cambridge University. 1998.

[16] REZENDE, M. C. **Fractografia de Compósitos Estruturais**. Polímeros: Ciência e Tecnologia, v 17, nº 3. 2007.

[17] SOUZA, JOÃO PAULO F. M. **Inspeção de Defeitos em Revestimentos de Materiais Compósitos Aplicados em Tanques Metálicos Utilizando Shearografia**. MSc dissertation – Federal University of Santa Catarina. 2012.

[18] SCHONTAG, J. M. **Caracterização da Profundidade de defeitos em Materiais Compósitos Utilizando Shearografia com Carregamento Vibracional**. – MSc dissertation – Federal University of Santa Catarina. 2009.

[19] GARCIA, J. P.; MORILLA, J. C. **Aplicação de materiais compósitos em reparos de tubulações de óleo e gás**. UNISANTA – Science and Technology, v 1, nº 1, pp. 14-19. 2012.

[20] NATIONAL OILWELL VARCO (NOV). **Bondstrand Marine and Offshore Piping Systems**. Retrieved 09/dec/2015 from <https://www.nov.com/Segments/Completion_and_Production_Solutions/Fiber_Glass_Systems/Marine_Offshore/Bondstrand_MOS/Bondstrand_MOS.aspx>.

[21] PRICE, J. C. **The "State of the Art" in Composite Material Development and Applications for the Oil and Gas Industry**. Proceeding of the Twelfth International Offshore and Polar Engineering Conference, pp. 125-131. 2002.

[22] STORHAUG, T.; STJERN, G.; PAULSHUS, B.; SLAMA, M. M. **Significant Achievements in Composites Technology in 2001. Qualification and Testing of Composite Tethers and Risers for Ultra Deep Water. Including Commenced Field Demonstration**

at Heidrun TLP. 13th Deep Offshore Technology Conference – New Orleans, USA. – 2001.

[23] MIRAVETE, A. **Alternative/Innovative Structural Concepts for Offshore Topside Composite Structures**. Composite Materials for Offshore Operations 3. Houston, Texas. 1993.

[24] DOS SANTOS FARO, A. A. **Desenvolvimento de Tubos Compósitos Produzidos por Enrolamento Filamentar para Possíveis Aplicações como Risers Rígidos**. MSc dissertation – Federal University of Rio de Janeiro. 2008.

[25] SHEN, F. C. **A Filament Wound Structure Technology Overview**. Materials Chemistry and Physics, v 42, pp. 96-100. 1995.

[26] CPIC FIBERGLASS. **Enrolamento Filamentar**. Retrieved 08/dec/2015 from <http://br.cpicfiber.com/processos.asp?codigo=7&cat=Processos>.

[27] BANEA, M. D.; da Silva, L. F. M. **Adhesively bonded joints in composite materials: an overview**. Proc. IMechE, v 223, Part L: J. Materials: Design and Applications. 2009.

[28] HEXCEL CORPORATION. **Redux Bonding Technology**. Publication No. RGU 034c – Rev. July 2003.

[29] POTTER, K. **Adhesively Bonded Joints Between Composites**. Composites Bonding/Fixing Event, City of Bristol College, 2012.

[30] FERRAZ, F.; GOMES, M.; ANDRADE, M. **Meio de Ligação de Tubos, Conexões de Tubulação, Válvulas Industriais**. Professor edited booklet – Electromechanics course – Federal Institute of Science, Technology and Education of Bahia. 2009.

[31] SANDERS, D. **Pipe Joints and Critical Performance Requirements by System Application**. Professional Development Advertising Section – CONTECH Engineered Solutions. 2009.

[32] EXTRACO COMPOSITES INDIA. **GRP/GRE/GRV Pipes and Fitting**. Retrieved 14/dec/2015 from <http://www.extraco composites.com/Products/GRP-GRE-GRV-Pipes-and-Fitting.html>.

[33] DAS, R. R.; PRADHAN, B. **Adhesion failure analysis of bonded tubular single lap joints in laminated fibre reinforced plastic**

composites. International Journal of Adhesion & Adhesives, v 30, pp. 425-438. 2010.

[34] LEES, J. M. **Behaviour of GFRP adhesive pipe joints subjected to pressure and axial loadings**. Composites: Part A, v 37, pp. 1171-1179. 2006.

[35] PARASHAR, A.; MERTINY, P. **Adhesively bonded composite tubular joints: Review**. International Journal of Adhesion & Adhesives, v 38, pp. 58-68. 2012.

[36] OH, J. H. **Strength prediction of tubular composite adhesive joints under torsion**. Composites Science and Technology, v 67, pp. 1240-1347. 2007.

[37] OH, J. H. **Torque capacity of tubular adhesive joints with different composite adherends**. Materials Letters, v 62, pp. 1234-1237. 2008.

[38] MISEN, N.; SINKE, J.; GROVES, R. M.; BENEDICTUS, R. **Market survey of flaws during composite laminate production and demand for a complementary monitoring system**. Under revision.

[39] RAO, M. R. P. D. **Review of Nondestructive Evaluation Techniques for FRP Composite Structural Components**. MSc dissertation – West Virginia University. 2007.

[40] OLIVEIRA, D. F.; SOARES, S. D.; LOPES, R. T. **Inspection of Composite Pipelines using Computed Radiography**. 5th Pan American Conference for NDT. Cancun, Mexico. 2011.

[41] DE ALMEIDA, P. D. **Inspeção por Ultrassom de Juntas Adesivadas de Tubulações em Material Compósito**. BSc dissertation. Federal University of Rio de Janeiro. 2011.

[42] KROEGER, T. **Thermographic inspection of composites**. Reinforced Plastics, v 58, issue 4, pp. 42-43. 2014.

[43] ALBERTAZZI, A. [ET AL.]. **Detecção de Falhas de Adesão Entre Mantas Poliméricas e Dutos Usando Interferometria de Deslocamento Lateral**. CONAEND 036. 2006.

[44] CRUPI, V.; EPASTO, G.; GUGLIELMINO, E. **Computed Tomography analysis of damage in composites subjected to**

impact loading. Frattura ed Integrità Strutturale, v 17, pp. 32-41. 2011.

[45] GREEN, W. H; SINCEBAUGH, P. **Nondestructive Evaluation of Complex Composites Using Advanced Computed Tomography (CT) Imaging**. Army Research Laboratory. ARL-TR-2400. 2001.

[46] KRUMM, M. [ET AL.]. **Capabilities and Applications of Specialized Computed Tomography for the Determination of Characteristic Material Properties of Fiber Composite Components**. iCT 2012 – Conference on Industrial Computed Tomography, Austria.

[47] STEINCHEN, W.; YANG, L. **Digital Shearography: Theory and Application of Digital Speckle Pattern Shearing Interferometry**. SPIE Press, Washington, 2003.

[48] SANTOS, F.; VAZ, M.; MONTEIRO, J. **A new set-up for pulsed digital Shearography applied to defect detection in composite structures**. Optics and Lasers in Engineering, v 42, pp. 131-140. 2004.

[49] UC DAVIS CHEMWIKI. **Dynamic Light Scattering**. Retrieved 16/dec/2015 from <http://chemwiki.ucdavis.edu/Analytical_Chemistry/Instrumental_Analysis/Microscopy/Dynamic_Light_Scattering>.

[50] CABRAL, T. D. **Caracterização Experimental de Um Sistema de Shearografia Para Inspeção Não Destrutiva de Tubulações Compósitas**. BSc dissertation – Federal University of Santa Catarina. 2014

[51] WILLEMANN, P. W. [ET AL.]. **Inspeção de Defeitos em Dutos Revestidos de Material Compósito Utilizando Shearografia**. Santos Offshore Conference. 2009.

[52] MURAD, M. A. **An Integrated Structural Health Monitoring Approach to Composite-Based Pipeline Repair**. PhD dissertation – Cranfield University. 2011.

[53] MAJUMDER, M. [ET AL.]. **Fibre Bragg gratings in structural health monitoring – Present status and applications**. Sensors and Actuators A, v 147, pp.150-164. 2008.

[54] SIANAKI, A. A. [ET AL.]**. Effect of Embedded Electric Sensor on the Structural Strength of Filament Wound Hybrid**

Composite. ASME 33rd International Conference on Ocean, Offshore and Arctic Engineering – Vol. 5: Materials Technology; Petroleum Technology. 2014.

[55] HOQUE, M. U.; TAYEBI, A. **Embedded MEMS Sensor for Structural Health Monitoring of Composite Materials**. Proceedings of the Seventeenth Annual Technical Conference of the American Society for Composites. 2012.

[56] JENSEN, D. W.; PASCUAL, J. **Degradation of graphite/ bismaleimide laminates with multiple embedded fiber-optic sensors**. SPIE Fiber Optic Smart Structures and Skins, v 1370, pp. 228-237. 1990.

[57] MOGHADDAM, M. K.; BOLL, D.; LANG, W. **Embedding rigid and flexible inlays in carbon fiber reinforced plastics**. IEEE/ ASME International Conference on Advanced Intelligent Mechatronics (AIM), pp. 1387-1392. 2014.

[58] SCHULZ, W. L. [ET AL.]. **Health monitoring of an adhesive joint using a multi-axis fiber grating strain sensor system**. Proc. SPIE 3586, Nondestructive Evaluation of Aging Aircraft, Airports and Aerospace Hardware III. 1999.

[59] SULEJMANI, S. [ET AL.]. **Adhesive Disbond Monitoring With Microstructured Optical Fiber Bragg Grating Sensors**. 7th European Workshop on Structural Health Monitoring, pp. 1194-1199. 2014.

[60] CANAL, L. P. [ET AL.]. **Monitoring strain gradients in adhesive composite joints by embedded fiber Bragg grating sensors**. Composite Structures, v 112, pp. 241-247. 2014.

[61] TAKEDA, N.; MINAKUCHI, S.; UMEHARA, T.; ITO, Y. **Life Cycle Monitoring of Curved Composite Parts Using Embedded Fiber Bragg Grating Sensors**. Advanced Materials Research, v 410, pp. 18-21. 2012.

[62] UDD, E. **Fiber Optic Smart Structures**. Proc. IEEE, Vol. 84, No. 1, pp. 60-66. 1996.

[63] UDD, E.; SPILLMAN JR., W. B. **Fiber Optic Sensors: An Introduction for Engineers and Scientists**. Wiley, New Jersey, 2011.

[64] KASHYAP, R. **Fiber Bragg Gratings**. Academic Press, 1999.

[65] KEISER, G. **Comunicações Por Fibras Ópticas**. AMGH, Porto Alegre, 2014.

[66] HILL, K. O.; FUJII, Y.; JOHNSON, D. C.; KAWASAKI, B.S. **Photosensitivity in optical fiber waveguides: Application to reflection filter fabrication**. Appl. Phys. Lett. 32, 647, 2014.

[67] MELTZ, G.; MOREY, W. W.; GLENN, W. H. **Formation of Bragg gratings in optical fibers by a transverse holographic method**. Optics Letters, Vol. 14, Issue 15, pp. 824-825. 1989.

[68] LINDER, E. [ET AL.]. **Post-hydrogen-loaded draw tower fiber Bragg gratings and their thermal regeneration**. Applied Optics, Vol. 50, No. 17, pp. 2519-2522. 2011.

[69] THYAGARAJAN, K.; GHATAK, A. **Fiber Optic Essentials**. Wiley, New Jersey, 2007.

[70] CHEN, Y. C.; HSIEH, C. C.; LIN, C.C. **Strain measurement for composite tubes using embedded, fiber Bragg gratin sensor**. Sensors and Actuators A, v. 167, pp. 63-69. 2011.

[71] KANG, H. K. [ET AL.]. **Cure monitoring of composite laminates using fiber optic sensors**. Smart Materials and Structures, v. 11, pp. 279-287. 2002.

[72] FRAZÃO, O. [ET AL.]. **Applications of Fiber Optic Grating Technology to Multi-Parameter Measurement**. Fiber and Integrated Optics, v. 24, pp. 227-244. 2005.

[73] KINET, D. [ET AL.]. **Fiber Bragg Grating Sensors toward Structural Health Monitoring in Composite Materials: Challenges and Solutions**. Sensors, v. 14, pp. 7394-7419. 2014.

[74] MAWATARI, T.; NELSON, D. **A multi-parameter Bragg grating fiber optic sensor and triaxial strain measurement**. Smart Materials and Structures, v. 17, 19pp. 2008.

[75] VALDIVIELSO, C. F.; MATÍAS, I. R.; ARREGUI, F. J. **Simultaneous measurement of strain and temperature using a fiber Bragg grating and a thermochromic material**. Sensors and Actuators A, v. 101, pp. 107-116. 2002.

[76] JUNG, J.; NAM, H.; LEE, J. H.; PARK, N.; LEE, B. **Simultaneous measurement of strain and temperature by use of a single-fiber**

Bragg grating and an erbium-doped fiber amplifier. Applied Optics, Vol. 38, No. 13, pp. 2749-2751. 1999.

[77] JUNG, J.; PARK, N.; LEE, B. **Simultaneous measurement of strain and temperature by use of a single fiber Bragg grating written in an erbium:ytterbium-doped fiber**. Applied Optics, Vol. 39, No. 7, pp. 1118-1120. 2000.

[78] HITZ, C. B.; EWING, J.; HECHT, J. **Introduction to Laser Technology**. IEEE Press / Willey, New Jersey, 2012.

[79] MOUSTAFA, A. (EDITOR) **Earthquake-Resistant Structures – Design, Assessment and Rehabilitation**. Chapter 19. InTech, 2012.

[80] SAMIEC, D. **Distributed fibre-optic temperature and strain measurement with extremely high spatial resolution**. Photonik international 2012.

[81] SANBORN, E. E. [ET AL.] **Distributed Fiber Optic Strain Measurement Using Rayleigh Scatter in Composite Structures**. Experimental and Applied Mechanics, Vol. 6, Conference proceedings of the Society for Experimental Mechanics Series 9999. 2011.

[82] KIRBY, A. J. **Polyimides – Materials, Processing and Applications**, Pergamon Press Ltd., Oxford, 1992.

[83] GEORG FISCHER HARVEL LLC. **Engineering & Installation Guide: PVC and CPVC extruded pipe, duct, and machining stock**. 2012.

[84] KOSAKA, T.; OSAKA, K.; SAWADA, Y. **Evaluation of Residual Strain of Fibres in Matrix Resin During Cure Process By Optical Fibre Sensors**. Proceedings of the 17th International Conference on Composite Materials. Edinburgh, 2009.

[85] MONTGOMERY, D. C.; RUNGER, G. C. **Estatística Aplicada e Probabilidade para Engenheiros**. LTC, Rio de Janeiro, 2003.

[86] ERDOGAN, T. [ET AL.] **Decay of ultravioleta-induced fiber Bragg gratings**. J. Appl. Phys., Vol. 76, No. 1, pp. 73-80. 1994.

[87] PATRICK, H. [ET AL.] **Annealing of Bragg gratings in hydrogen-loaded optical fiber**. J. Appl. Phys., Vol. 78, No. 5, pp. 2940-2945. 1995.

APPENDIX A – Block Diagram of Labview VI for Extracting Data from Measurement Logs

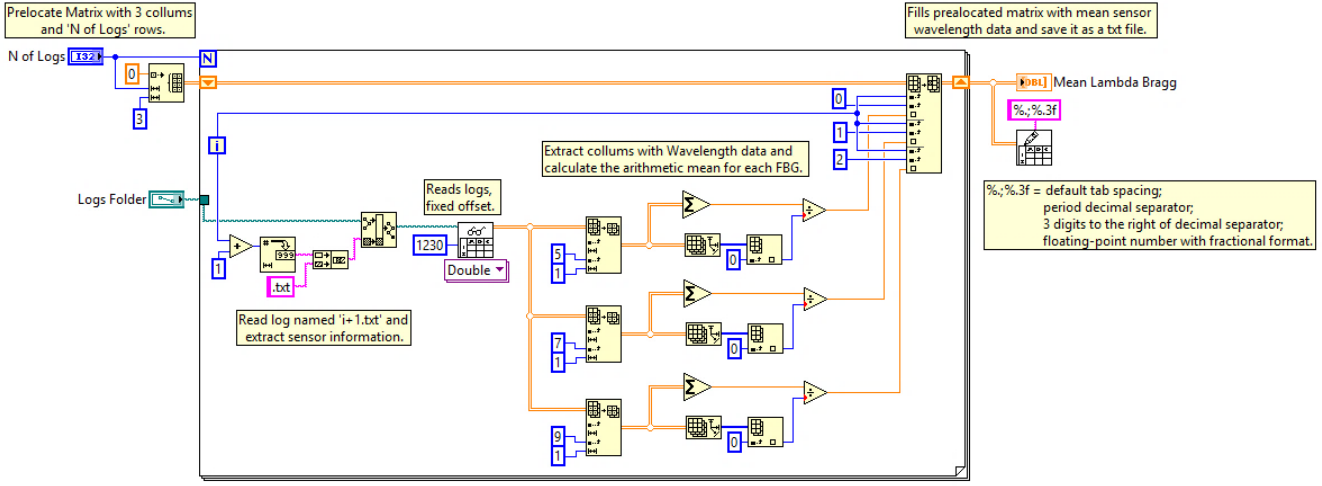

APPENDIX B – Matlab Code for Sensor Data Handling and Plotting

```
%% Clears screen and variables %%

clc
clear

%% Import Fiber Bragg Gratings Measurements %%

dataSet1 = fopen(logA.txt');
    sensorData1 = textscan(dataSet1,'%f %f %f','CollectOutput',1);
fclose(dataSet1);

dataSet2 = fopen(logB.txt');
    sensorData2 = textscan(dataSet2,'%f %f %f','CollectOutput',1);
fclose(dataSet2);

Z = sensorData2{1}' - sensorData1{1}';

%% Converts Wavelength Differences to micro-Strain Differences %%

Z = 10^6*Z./(0.769*sensorData1{1}');

%% Creates a 2D-Grid and Grid Interpolants F %%

[X,Y] = ndgrid(0:2,0:12);

Fl = griddedInterpolant(X,Y,Z,'linear');
Fc = griddedInterpolant(X,Y,Z,'cubic');

%% Interpolates Grid Values and Sensor Data %%

[Xq,Yq] = ndgrid(0:.1:2,0:.1:12);

tri = delaunay(Xq, Yq);

Zl = Fl(Xq,Yq);
Zc = Fc(Xq,Yq);
```

```
%% Multiple Plots for the Interpolated Grids and Data %%

figure()
    trisurf(tri,Xq,Yq,Zl,'FaceColor','interp', 'EdgeColor ', ‘none')
    axis([0 2 0 12])
    set(gca, 'XTick', 0:1:2)
    set(gca, 'YTick', 0:1:12)
    colorbar
    title('Linear Delaunay Grid')

figure()
    trisurf(tri,Xq,Yq,Zc,'FaceColor','interp', 'EdgeColor ', ‘none')
    axis([0 2 0 12])
    set(gca, 'XTick', 0:1:2)
    set(gca, 'YTick', 0:1:12)
    colorbar
    title('Cubic Delaunay Grid')

figure()
    pcolor (Xq, Yq, Zl) , shading interp
    axis([0 2 0 12])
    set(gca, 'XTick', 0:1:2)
    set(gca, 'YTick', 0:1:12)
    colorbar;
    title('Linear Grid Color Plot’)

figure()
    pcolor (Xq, Yq, Zl) , shading interp
    axis([0 2 0 12])
    set(gca, 'XTick', 0:1:2)
    set(gca, 'YTick', 0:1:12)
    colorbar;
    title('Cubic Grid Color Plot’)

figure()
    contour(Xq, Yq, Zc);
    axis([0 2 0 12])
    set(gca, 'XTick', 0:1:2)
    set(gca, 'YTick', 0:1:12)
    title('Linear Grid Contours')
```

```
figure()
    contour(Xq, Yq, Zc);
    axis([0 2 0 12])
    set(gca, 'XTick', 0:1:2)
    set(gca, 'YTick', 0:1:12)
    title('Cubic Grid Contours')
```